Advancing Chiral Plasmonics Using Single-Molecule Localization Microscopy

by

Zechariah J. Pfaffenberger

A dissertation submitted in partial fulfillment
of the requirements for the degree of
Doctor of Philosophy
(Chemistry)
in the University of Michigan
2023

Doctoral Committee:

Professor Julie S. Biteen, Chair
Professor Andrew Ault
Professor L Jay Guo
Professor Roseanne Sension

Zechariah J. Pfaffenberger

zpfaffen@umich.edu

ORCID iD: 0000-0002-9878-5445

Dedication

For Vivian, Phillip, and Peter

No one is a failure who has good friends

Acknowledgements

Doing a Ph.D. was an oddly spur of the moment decision for me. In spite of that, I doubt anyone who knows me well will be surprised that I have gotten to this point. The only person who might be truly shocked is me. Completing this degree has been one of the hardest things I have done in my life. What I mostly feel and understand at the end is a profound sense of gratitude. It does truly take a village to finish this kind of degree and I'm so thankful for all the folks I met along the way.

I want to thank the many collaborators who have contributed to the work in this thesis and during my time in the Biteen lab more broadly. Thank you to Dr. Nadra Al-Husini and Professor Jared Schrader who helped on my very first project in the Biteen lab on phase separation. You taught me the power of collaboration in science early on. Thank you to Dr. Anthony Balistreri for teaching so much about amyloid fibrils and humoring my crazy microscopy ideas. Thank you to Dr. Nicholas Kotov and his lab members: Dr. Ji-Young Kim and Connor McGlothlin. Ji-Young and Connor, thank you for the exciting science conversations and meetings in the NCRC lobby. Thank you to Maciej Lipok and Professor Olesiak-Bańska from Wroclaw University of Science and Technology. I am so excited to see where our collaboration goes and for more great science chats in the future. Maciej, hosting you and introducing you to all that the U.S.A. has to offer was a genuine joy. I will come to Poland someday so we can hit up some of your favorite places. I'd also like to thank the folks in the plasmonics and microscopy community who provided feedback

and answered questions: Dr. Michelle Solomon, Dr. Lisa-Maria Needham, and Professor Matt Lew.

It has been a true privilege to work with Professor Julie Biteen for my Ph.D. Thank you, Julie, for taking a chance on a random liberal arts kid from Indiana. Thank you also for always being available to chat with your students and colleagues. It is a truly good thing.

I'd like to thank all the Biteen lab alumni who I've worked with over the years. I'd like to particularly thank Dr. Stephen Lee, Dr. Josh Karslake, Dr. Curly Zuo, and Dr. Ben Isachoff for their mentorship early on in summer 2018. You were kind and patient when I knew how to do absolutely nothing. I'd also like to thank Dr. Aathmaja Anandhi Rangarajan and Dr. Laurent Geffroy. I'd also specially like to thank Dr. Hannah Chia. Thank you for being a mentor (and friend) during 2020 and 2021. I still think (fondly?) of those times you and I (socially distanced) worked in the office together as you were completing your thesis. I think we really needed each other in those moments.

Thank you Dr. Ziyuan Chen, Dr. Lauren McCarthy, Dr. Luis Ortíz-Rodríguez, and Dr. Daniel Foust, David Fuller, Kate Fyodorova, and Xiaofeng Dai for your input on presentations and helping me grow as a scientist. Thank you also for the fun happy hours out in Ann Arbor or game nights as a lab. Thanks specifically to Chris Azaldegui for the same and for being an amazing travel companion in Spain. I will truly never forget our first GRC together. I'd also like to specifically thank Dr. Anna Calkins. Your skill as a scientist and communicator inspires me as does your care for others. Finally, I'd like to specially thank Saaj Chattopadhyay. The work herein was accelerated and made possible with your input and hard work. You and I both know there's been a lot of challenging moments, but I'm incredibly proud of what we have accomplished. You

are an amazing scientist, communicator, and person. I'm so excited to see the directions you take this research in the future.

Thank you to the members of my committee: Professor Andrew Ault, Professor Roseanne Sension, and Professor Jay Guo. Each of you has helped strengthen my skills as scientist. I'd also like to thank Biteen lab rotation students: Shelby Nicolau, Adam Decker, and Sara Jovanovski. It was such a pleasure to work with each of you and amazing to see you all going to have your own incredible careers as graduate students here at University of Michigan.

Thank you to my many friends at University of Michigan and in the Ann Arbor area. In particular, Dr. Khoi Dang, Carson Szot, Raz Jugovic, Dr. Taylor Soucy, Dr. Bernadette Sneider, Amy Getz, Daniel Whitford, Micah Bush, Ritz Raju, Dr. Emily Tucker, Dr. Emily Mueller, Dr. Petra Vande Zande, Dr. Anna Michmerhuizen, Hayley Herderschee, and Jon Jaber. Special thanks to Virginia Larson for introducing me to rock climbing and for all our backpacking/camping adventures across the great state of Michigan. I hope we get to camp and climb again in the future.

Thank you to the many friends and family who have stuck with me despite distance. Thank you to my parents, Dave and Tracy, and to my sisters, Melody and Karie, for believing I could do this when I really believed I couldn't, and for loving me no matter the circumstances. Thank you to Michael Heckman. We've got to go to more Michigan Football games even though I won't have as convenient a place to stay. Thank you the John Wesley Honors College Class of 2018 at Indiana Wesleyan University. I miss each and every one of you often. Our little group chat is something that keeps me going. I must specifically thank my former roommates John Kristof, Albert Gustafson, and Justin Stuckey as well as Sydney Gustafson and Andra Wolgemuth. PZ and the SQuad never fails to put a smile on my face.

Finally, I want to thank Peter Troutner, Phillip Quinn, and Vivian Crum to whom this thesis is dedicated. You are my closest friends and I truly believe your friendship more than anything else helps make me the person I am and helped me get through writing this thesis. I love you each so much. There is no greater gift in life than friendship.

Table of Contents

List of Tables

List of Figures

Abstract

Fluorescence microscopy is an important tool for studying structures in living cells, but its use is limited to sizes greater than 300 nm due to the diffraction limit of visible light. Single-molecule localization microscopy overcomes this limitation by fitting the diffraction-limited image of a single molecule to a two-dimensional Gaussian function, enabling the study of subcellular biophysics and nanoscale devices. The precision on the peak position estimation improves with the number of photons collected and can reach tens of nanometers with fluorescent proteins and organic dyes.

On the other hand, plasmonics is the study of the collective oscillation of free electrons in a metal. Plasmonics has enabled incredible control of light on the nanoscale. Plasmonic nanoparticles act as antennas that convert propagating visible light from the far field to localized electromagnetic fields. These nanoparticles can also act as antennas that couple near-field energy to the far field by increasing the radiative rate of nearby fluorescent molecules. The net effect is that plasmonic nanoparticles can increase the number of photons detected per unit of time from a fluorescent molecule. This plasmon-enhanced fluorescence has successfully been applied to increase the precision in single-molecule localization microscopy.

The subfield of chiral plasmonics deals with the ability of these plasmonic nanoparticles to increase optical signals related to the molecular property of chirality—the geometric property of molecules that cannot be superimposed on their mirror image through rotations and translations. In addition to increasing the electric field intensity, nanoparticles can twist a circularly polarized

propagating wave through a circle in an area much smaller than its wavelength, thus more efficiently coupling ultraviolet and visible light (hundreds of nanometers) to the length scale of chiral molecules (one angstrom − one nanometer). This subfield of chiral plasmonics has grown very fast in the last ten years because of its broad applicability to many research areas including biosensing, chemical catalysis, pharmacology, agricultural science, and information technology.

The work in this thesis combines the resolution of single-molecule localization microscopy with the enhancement of chiral plasmonics. I collaborated with Saaj Chattopadhyay to design and build a polarization microscope capable of studying single-molecule chiral plasmonics. I then used this instrument for three major projects. I measured a strong emission dissymmetry from single nanohelicoids fabricated by collaborators in Dr. Nicholas Kotov's lab and determined that their fabrication method was highly selective based on single-particle data. In a study of near-field interactions of chiral nanoparticle dimers with achiral fluorescent molecules, I measured an induced fluorescence dissymmetry in the achiral dye Cy5.5 of ~|0.5| from only 100 zmol sample (10^4 molecules). I collaborated with Saaj Chattopadhyay to show that the electromagnetic property of optical chirality represents regions of maximal redirection of left-circularly polarized and right-circularly polarized emission by correlating electromagnetic simulations with experimental data. I collaborated with Maciej Lipok and Saaj Chattopadhyay to apply the polarization microscope to the interactions of achiral nanoparticles bound to a chiral biopolymer, the amyloid fibril. We found that binding to amyloid can induce a circular dichroism signal from gold nanorods without micron-scale order and that small aggregates of a few (2-5) nanoparticles dominate this induced signal.

This thesis demonstrates how single-molecule and single-particle techniques can uncover heterogeneities missed in bulk experiments to enable improved sensing of enantiomers, better selectivity for single-molecule imaging of chiral biomolecules, and more efficient light-emitting

devices. More broadly, this thesis expands the list of properties we can observe at the nanoscale by applying single-molecule localization microscopy to chirality.

Chapter 1
Introduction

1.1 Microscopy and Chirality: Hand-in-Hand

Chirality is a fundamental property of nature from the twist of spiral galaxies to individual amino acids.[1–5] It is the geometric property of an object that cannot be mapped onto its mirror image through rotations and translations alone, also called a non-superimposable mirror image. Perhaps the most common natural example of chirality is our own human hands (Figure 1.1a).

In the field of chemistry, chirality refers to molecules that have the same molecular formula and bond distances between atoms, but their 3D structure is not superimposable on their mirror image. A molecule possessing chirality and its mirror image are termed enantiomers. It might seem like enantiomers would be uncommon; however, they occur so often in nature that entire subfields and journals are devoted to their study.[6] Chirality is important because most biomolecules (i.e., nucleic acids and proteins) are chiral. Furthermore, naturally occurring proteins and nucleic acids show a heavy preference for one enantiomer over the other. This preference is called homochirality. Why nature shows such a strong enantiomeric preference is still a debated question in the scientific literature.[7–9]

Chiral molecules and microscopy have been intertwined since Louis Pasteur observed tartaric acid crystals in 1844.[10] In this groundbreaking study, Pasteur observed two enantiomers for the first time. This observation was made by examining the crystals under a magnifying lens and carefully sketching their structures (Figure 1.1b). This discovery created a new field of

stereochemistry. Pasteur was quite fortunate that he studied a molecule that formed crystals microns in size.[11,12] Because they were sufficiently large, he could see the enantiomer shapes under his lens. However, most enantiomeric molecules are nanometers in size; thus, they are too small to be observed with typical microscope optics (see 1.2.2).

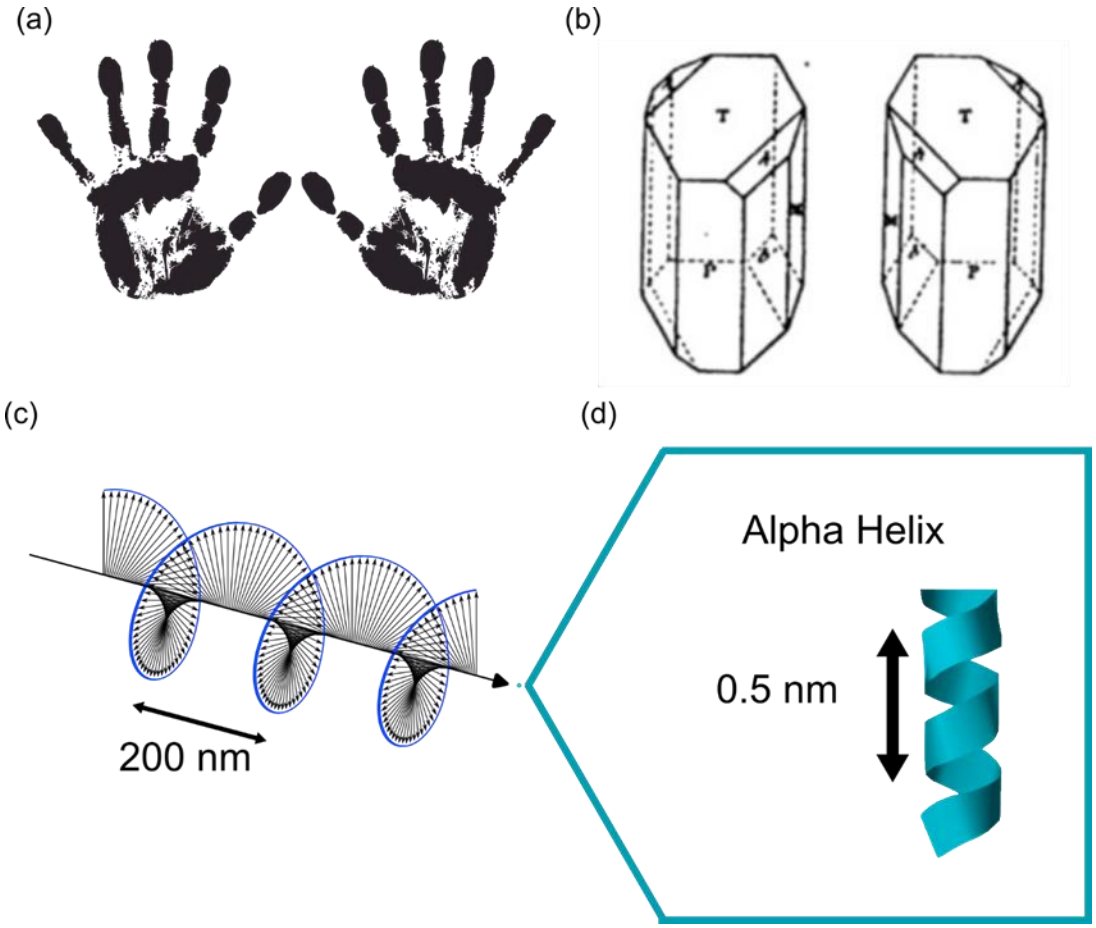

Figure 1.1: Examples of Chirality and Length Scales of Chiral Molecules.
(a) The human hand is a common example of a chiral object. (b) Louis Pasteur's original drawings of the tartartic acid crystal enantiomers.[10] (c) The length scale of circularly polarized visible light compared to an alpha helix displayed as an infinitesimal point (blue dot). (d) Blown up image of an alpha helix showing the pitch of the helix.

Because molecules are so small, we cannot just take pictures under a lens to determine which enantiomer of a molecule we are working with most of the time. Chemists rely on spectroscopy to distinguish enantiomeric molecules. The types of spectroscopy that can distinguish

enantiomers rely on the different interactions of enantiomers with circularly polarized light. Light waves are transverse waves, meaning that the oscillation of the wave is in a plane perpendicular to the wave propagation direction.[13,14] If the vector in the direction of oscillation traces a line, the light is said to be linearly polarized. If the vector's components are out of phase, the vector will trace a circle (Figure 1.1c). The circle can either rotate clockwise or counterclockwise and it is referred to as right-handed or left-handed. Two important types of spectroscopy for this thesis are circular dichroism (CD) and circularly polarized luminescence (CPL) spectroscopy. Techniques that measure differences in molecules' response to circularly polarized light are collectively called chiroptical spectroscopy and are powerful ways to determine chiral molecular structure.

However, chiroptical spectroscopic techniques have limitations. High concentrations of enantiomeric molecules, often micromolar and above, are required to obtain a sufficient signal. These low signals in chiroptical spectroscopy are particularly low because the wavelength of ultraviolet or visible light that excites electronic transitions in the molecule is much longer than the molecular length scale.[15,16] Thus, the circularly polarized wave is twisted only by a very small amount upon interacting with the molecule (Figure 1.1c). A lot of recent chiroptical spectroscopy work has sought to bridge these length scales. Tang and Cohen first showed that Maxwell's equations permitted a standing wave to twist through a full circle in an area much smaller than the wavelength under the right conditions and formulated a new conservation law related to molecular chirality they termed optical chirality.[17] They then showed that this quantity has physical relevance by creating such a standing wave with a beam reflected off a mirror interfering with itself.[18] Follow-up work has shown that evanescent fields near nanostructures can also have unusually high optical chirality and enhanced spectroscopy signals.[15,19]

These enhanced spectroscopic techniques hold great promise for increasing the sensitivity of enantiomer detection even to the single-molecule level.[20] However, most studies have been conducted using bulk instruments and diffraction-limited optics, which lack sufficient spatial resolution to uncover spatial heterogeneities in the field enhancements which decay in the near-field of antennas on the order of tens of nanometers. Additionally, there is a great interest in combining measurements of the chirality of biomolecules with spatial information on subcellular structures. For example, Robert Pal's lab at Durham University has combined CPL spectrometers with scanning confocal microscopes. These studies correlating CPL with microscopy leverage lanthanide complex probes to report on the chiroptical properties of biomolecules.[21] Though these probes are expensive, combining chiroptical measurements with the spatial resolution of modern super-resolution microscopes may open doors to understanding how chiral recognition happens in living cells.[22]

The work reported in this dissertation extends the ability of the microscope to distinguish enantiomers beyond the diffraction limit. I achieved this by constructing a polarimetric microscope and using plasmonic nanoparticles. By imaging single organic fluorescent dyes interacting with chiral plasmonic nanostructures, I uncovered how fluorescence emission patterns are affected by the circular polarization of electromagnetic fields near such nanostructures, laying the groundwork for future studies combining super-resolution imaging with the signal-enhancing power of chiral plasmonic nanoparticles. I also determined how achiral nanoparticles can be powerful sensors of biomolecular chirality at the single-molecule level by measuring difference signals of nanoparticle aggregates templated onto a biopolymer, the insulin amyloid fibril.

1.2 Visible Light Microscopy

1.2.1 Fluorescence Microscopes

The discovery of bacteria cells by Anton van Leeuwenhoek was made using a visible light microscope.[23] Leeuwenhoek used a bright field microscope which creates contrast based on the different absorbance of light between a material and the background. Today, many different strategies exist for creating the contrast necessary for imaging. Some of these include dark-field microscopy which relies on scattering, differential-interference contrast microscopy, and phase contrast microscopy.

Most important for this thesis is fluorescence microscopy. The modern fluorescence microscope is a powerful tool that allows scientists to study living cells in their natural environment with great specificity. The photophysical process of fluorescence creates contrast in this technique (Figure 1.2). This process begins when a molecule is first promoted from a singlet ground state, S_0, to an excited state, S_1, through absorption (purple arrow) which takes place nearly instantaneously at less than 1 fs.[24] Photon absorption can excite an electron to any vibrational excited state but it will quickly relax to the lowest vibrational level (on the order of 10 fs to 1 ps).

The major pathway for the de-excitation of most dyes and proteins used in fluorescence microscopy at this point is radiative decay to the ground state from the singlet excited state, emitting a photon in a process termed fluorescence (1 to 10 ns lifetimes). Fluorescence microscopists take advantage of the fact that the energy of this fluorescence transition is smaller than that of absorption; this Stokes shift allows us to filter out the excitation light. This is unlike normal bright-field microscopy which includes all the transmitted light from the source. In this way, the modern fluorescence microscope can observe living cells in their natural environment with a high signal-to-noise ratio and without damaging the cells with high excitation powers.

While fluorescence is the most probable transition for the fluorescent molecules used in this thesis (fluorescence quantum yield > 50%), it is also possible for the molecule to decay non-radiatively to the ground state, for example through converting energy to heat. One other photophysical pathway is intersystem crossing into a triplet state. From this triplet state, the molecule can radiatively decay on a long timescale (ms), in a process known as phosphorescence (Figure 1.2, orange arrow). However, because the relaxation of the triplet state to the singlet ground state is spin-forbidden, this triplet state is long-lived, and molecules in the triplet state can be quenched by interaction with oxygen, which has a triplet ground state, in a process termed photobleaching (Figure 1.2, black arrow).

The quantum yield of a fluorescent molecule is defined as:

$$\phi = \frac{\gamma_{rad}}{\gamma_{rad} + \gamma_{nrad}} \tag{1.1}$$

where γ_{rad} is the rate constant for the fluorescence radiative transition and γ_{nrad} is the rate constant of all the non-radiative pathways. The fluorescence lifetime is inversely related to the rate constants by equation (1.2).

$$\tau = \frac{1}{\gamma_{rad} + \gamma_{nrad}} \tag{1.2}$$

Typical quantum yields for fluorescent proteins and organic dyes are greater than 0.5, such that the fluorescence is the most prevalent relaxation pathway.[25,26] Based on the fluorescence quantum yield and the radiative rate, as well as the high quantum efficiency of EMCCD cameras, we can detect thousands of photons from each molecule in a single camera frame at frame rates on the order of 100 hertz (Hz). Getting these numbers of photons and filtering out the excitation source results in a sufficient signal-to-noise ratio for single-molecule detection.

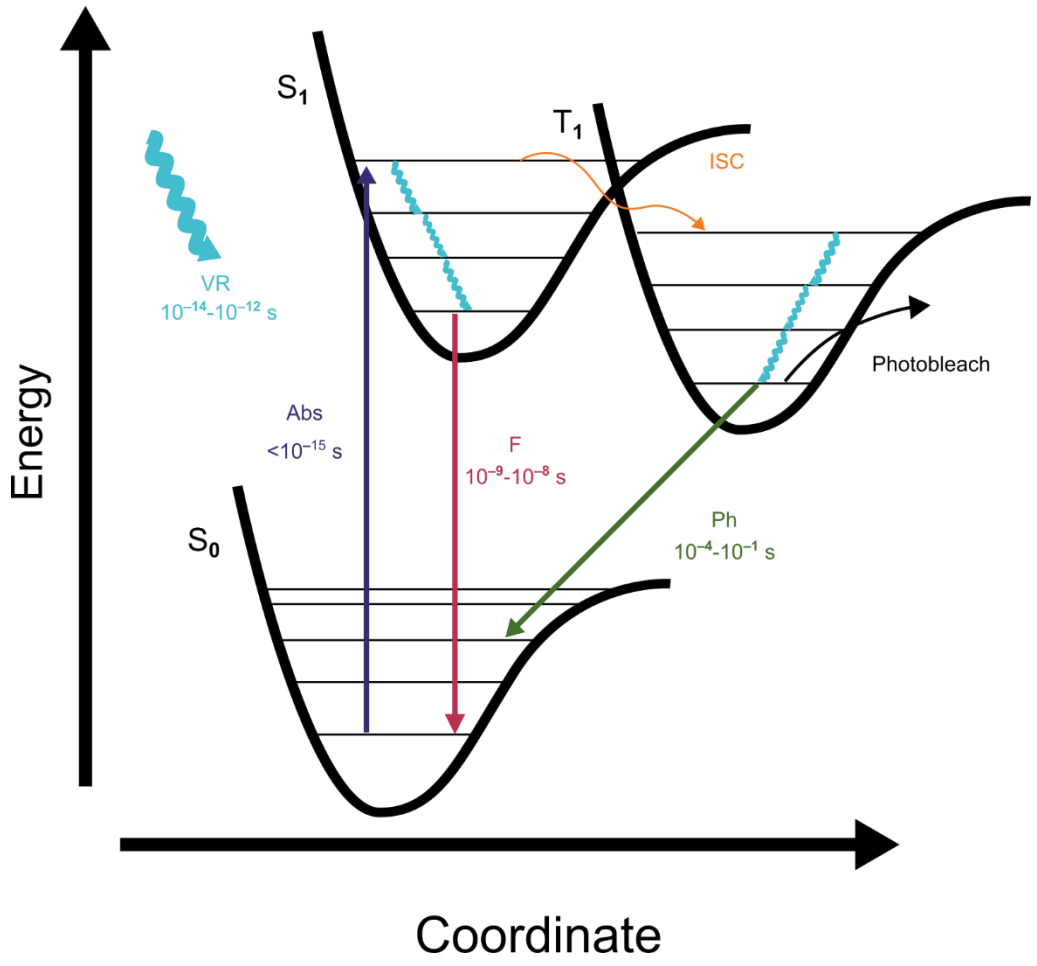

Figure 1.2: Franck-Condon energy diagram and photochemical process timescales.
S_0: Singlet Ground State, S_1: Singlet Excited State, T_1: Triplet Excited State, Abs: Absorption, F: Fluorescence, Ph: Phosphorescence, VR: Vibrational Relaxation, ISC: Intersystem crossing

Many types of fluorescent molecules and tags for fluorescence microscopy have been developed like fluorescent proteins.[27,28] These tags are selective for a target; a fluorescent protein can be genetically encoded to be attached to a specific protein in the cell

. One class of organic fluorescent molecules that illustrate the process in Figure 1.2 important to this thesis are cyanine dyes. These dyes are important for fluorescence microscopy and single-molecule microscopy because they can easily be conjugated into biomolecules like DNA or proteins.[29–33] Two nitrogen atoms in heterocyclic rings joined by an odd-numbered polymethine chain of carbon atoms are characteristic of a cyanine dyes (Figure 1.3a).[34] Indole,

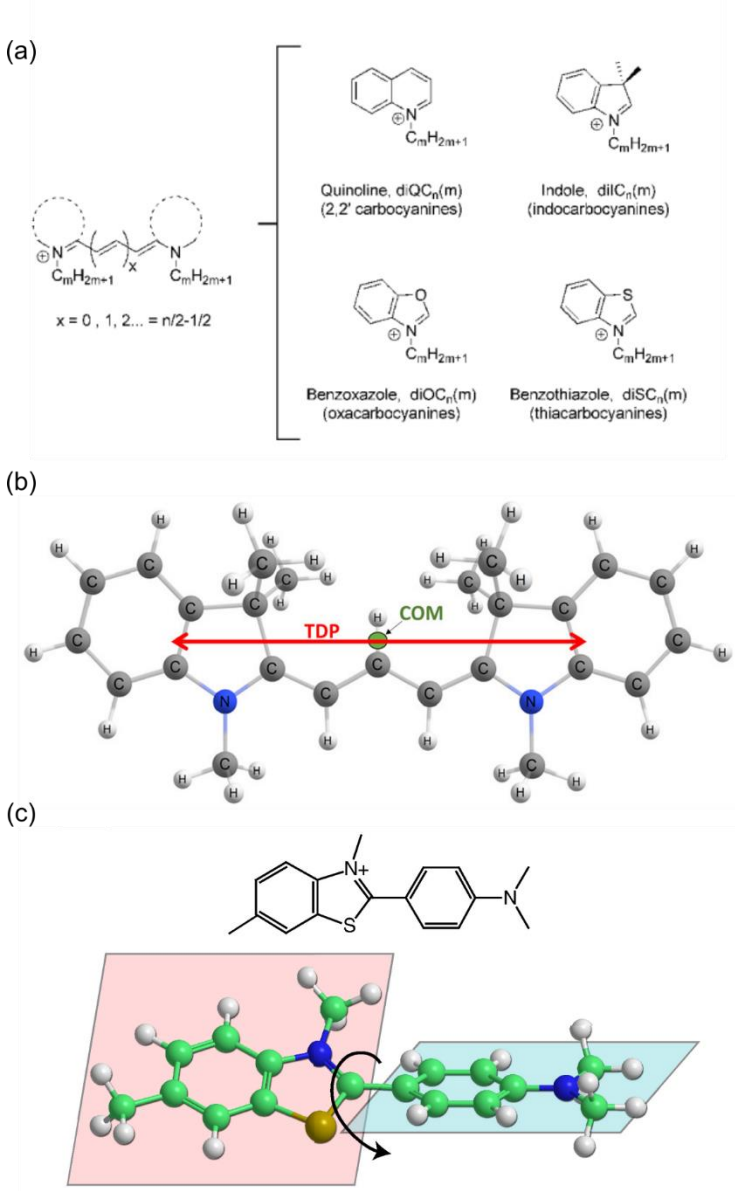

Figure 1.3: Cyanine dyes and molecular structure of electric dipole allowed transitions. (a) General structure of cyanine dyes and heterocylic moieties. Adapted from reference 30.[30] (b) Molecular structure of Cy3 with absorption transition dipole moment overlaid as a red arrow. TDP: transition dipole moment, COM: center of mass. Adapted from reference 35.[35] (c) Molecular structure of Thioflavin T (top) and the calculated geometry of this dye when bound to amyloid fibrils showing the twist (black arrow) between the benzaminic and benzothiaole rings. Adapted from reference 36.[36]

quinoline, benzoxazole or benzothiazole heterocycles are some of the most common heterocyclic rings used to stabilize these systems. The general nomenclature for cyanine dyes diXCm(n), where n is the number of carbon atoms in the polymethine chain, m is the number of carbon atoms in the

primary alkyl substituents attached to the nitrogens, and X is I, Q, O, or S for cyanine dyes containing indole, quinoline, benzoxazole or benzothiazole heterocyclic groups. In this thesis, I use the indolecyanine dye Cy5.5 which has an extra benzole ring fused to the indole which is where the extra 0.5 added to the n = 5 carbon atoms in the polymethine chain comes from.

The strong absorption in the visible range for cyanine dyes comes from a delocalized π-electron system in the polymethine conjugated chain of carbon atoms connecting the heterocyclic rings. The length of this conjugated chain can have a strong effect on the absorption and emission wavelengths for these dyes.[37,38] One additional double bond shifts the absorption and fluorescence emission by around 100 nm allowing one to choose the absorption and emission throughout the visible spectrum.[39,40]

The S_0 to S_1 transition in these dyes is a promotion of one of the π-electrons from the highest occupied molecular orbital (HOMO) to the lowest unoccupied molecular orbital (LUMO).[37] Absorption of a photon in the $S_0 \rightarrow S_1$ transition can be described as a transition between two quantum mechanical states as a result of a perturbing electromagnetic field. The absorption coefficient, ε, for such a transition can be derived to a first-order approximation from Fermi's golden rule.[41]

$$\varepsilon = \frac{N_A \pi \omega \delta(\omega - \omega_{fi})}{\varepsilon_0 \hbar c \ln 10} \frac{1}{E_0^2} |\langle f|H'|i\rangle|^2 \rho(\omega) \tag{1.3}$$

In this equation, $\hbar$ is the reduced Planck's constant, ω is the frequency of the transition, the speed of light is c, N_A is Avogadro's number, ε_0 is the vacuum permittivity, E_0 is the amplitude of the perturbing field, and $\rho(\omega)$ is the density of states at the transition frequency. The Dirac delta function, $\delta(\omega - \omega_{fi})$, for the difference in frequency between the perturbing wave, ω, and the frequency of the transition, ω_{fi} shows that the transition will only occur when the photon energy

equals the energy of the transition. $\langle f|H'|i\rangle$ is the matrix element of the Hamiltonian that describes the perturbation between the initial and final states. Fermi's golden rule is a general equation for any quantum system interaction with a time-dependent perturbation. A full derivation is beyond the scope of this thesis. Interested readers should look into Kelley's Molecular Spectroscopy Chapter 4 for a full derivation.[42]

For absorption spectroscopy, the Hamiltonian of interest for the perturbation is normally found from a Taylor series expansion of the time-dependent part of the Pauli equation which is the form of the Schrödinger equation for electrons bound to atoms.[43] The Hamiltonian operator for such a system can be written as

$$H' = -\boldsymbol{\mu} \cdot \boldsymbol{E} - \boldsymbol{m} \cdot \boldsymbol{B} + higher\ order\ terms \tag{1.4}$$

Here, $\boldsymbol{E}$ and $\boldsymbol{B}$ are the electric and magnetic parts of the electromagnetic field respectively. The electric and magnetic dipole moments, $\boldsymbol{\mu}$ and $\boldsymbol{m}$, respectively are the first and second-order terms in the Taylor series expansion. This transition electric dipole moment is the dominant term for the absorption of a photon in cyanine dyes. In the case of cyanine dyes, the transition dipole moment for electronic absorption is in the plane of the molecule along the direction of the delocalized π-electrons (Figure 1.3b).

In addition to helping us understand the absorption response of cyanine dyes, the expression in equation (1.3) can also explain why CD signals are so weak from a quantum mechanical perspective. Absorption is the result of an electromagnetic field rearranging electrons to a new stationary state.[44] The linear rearrangement of electron density during the transition by the electric field is the electron transition dipole moment, denoted $\boldsymbol{\mu}$ as above. In contrast, the magnetic field induces a circular rearrangement of electron density and is called the magnetic dipole moment, denoted $\boldsymbol{m}$.

Circular dichroism is the difference between the molar absorption coefficients for LCP and RCP, denoted ε_{LCP} and ε_{RCP}.[45] The Rosenfeld equation (equation (1.5)) can be derived using Fermi's golden rule to calculate the difference in these molar extinction coefficients, $\Delta\varepsilon$, of a molecule excited with an LCP or RCP wave. An excellent derivation of this equation can be found in reference 41.[41]

$$\Delta\varepsilon = \frac{4k}{3c} Im(\boldsymbol{\mu} \cdot \boldsymbol{m}) \tag{1.5}$$

Here k is a constant that subsumes all the terms in the first factors of equation (1.3) and c is the speed of light. The Rosenfeld equation is the theoretical starting point for most CD research. From the Rosenfeld equation, it's easy to see that CD signals will be positive if $\boldsymbol{\mu}$ and $\boldsymbol{m}$ are parallel and negative if antiparallel.[44] Additionally, we can see from a quantum mechanical perspective, CD comes about because of interference between electric dipole and magnetic dipole transitions. The magnetic dipole part of this equation comes from the second-order terms in the Taylor series expansion for the time-dependent Hamiltonian, thus the magnetic dipole terms are weak resulting in small differences in the final molar extinction coefficient.[46] Interaction energies for these magnetic dipole moments are thousands of times weaker than electric dipole interactions.[44]

The types of CD transitions important for this thesis are called exciton CD transitions that result from the interference between an electric dipole-allowed (EDA) transition and an induced magnetic moment of another EDA transition. These are important in this thesis because noble metal nanoparticle LSPRs are dominated by electric dipole responses as are small organic molecules.[47] These EDA transitions are optically active, showing differences in extinction coefficients for LCP and RCP waves, because of an induced magnetic dipole in a nearby chromophore. Thioflavin T (ThT), an important fluorescent probe in Chapter 4, is an excellent example of this kind of system. When bound to amyloid fibrils, ThT shows an induced CD signal

resulting from a chiral twist of its two aromatic moieties, the benzaminic and benzothiaole rings (Figure 1.3d). This ThT confirmation is an illustrative example of coupled-oscillator CD. A deeper discussion of this theory can be found in Chapters 8 and 10 of Rodger and Nordén's book on CD spectroscopy.[44]

1.2.2 Super-resolution, Single-molecule Localization Microscopy

Although fluorescence microscopes are powerful tools, they are limited by the wave nature of light. Even modern precision-engineered lenses can only focus light to a finite limit. This diffraction limit was first formalized by Abbe in the 1800s.[48] A single fluorescent molecule can be approximated as a point emitter. When a point dipole's emission is convolved with the microscope objective lens system, it forms a diffraction pattern at the image plane termed a point spread function (PSF). The PSF is described mathematically as an Airy disk.

Lord Rayleigh established the criterion for the resolution of point emitters in 1879.[49] The Rayleigh criterion states that two point emitters can be resolved if the point spread function maximum of one emitter appears in the first minimum of the Airy disk or beyond of the second emitter. This is quantified in the following equation:

$$Rayleigh\ Resolution = \frac{0.61\lambda}{NA} \tag{1.6}$$

where λ is the wavelength of the light and NA is the numerical aperture of the imaging lens. Figure 1.3a shows the PSF of a single emitter. Figure 1.3b shows two unresolved emitters. Figure 1.3c shows two emitters at $D = \frac{0.61\lambda}{NA}$ so they can be resolved according to the Rayleigh criterion.

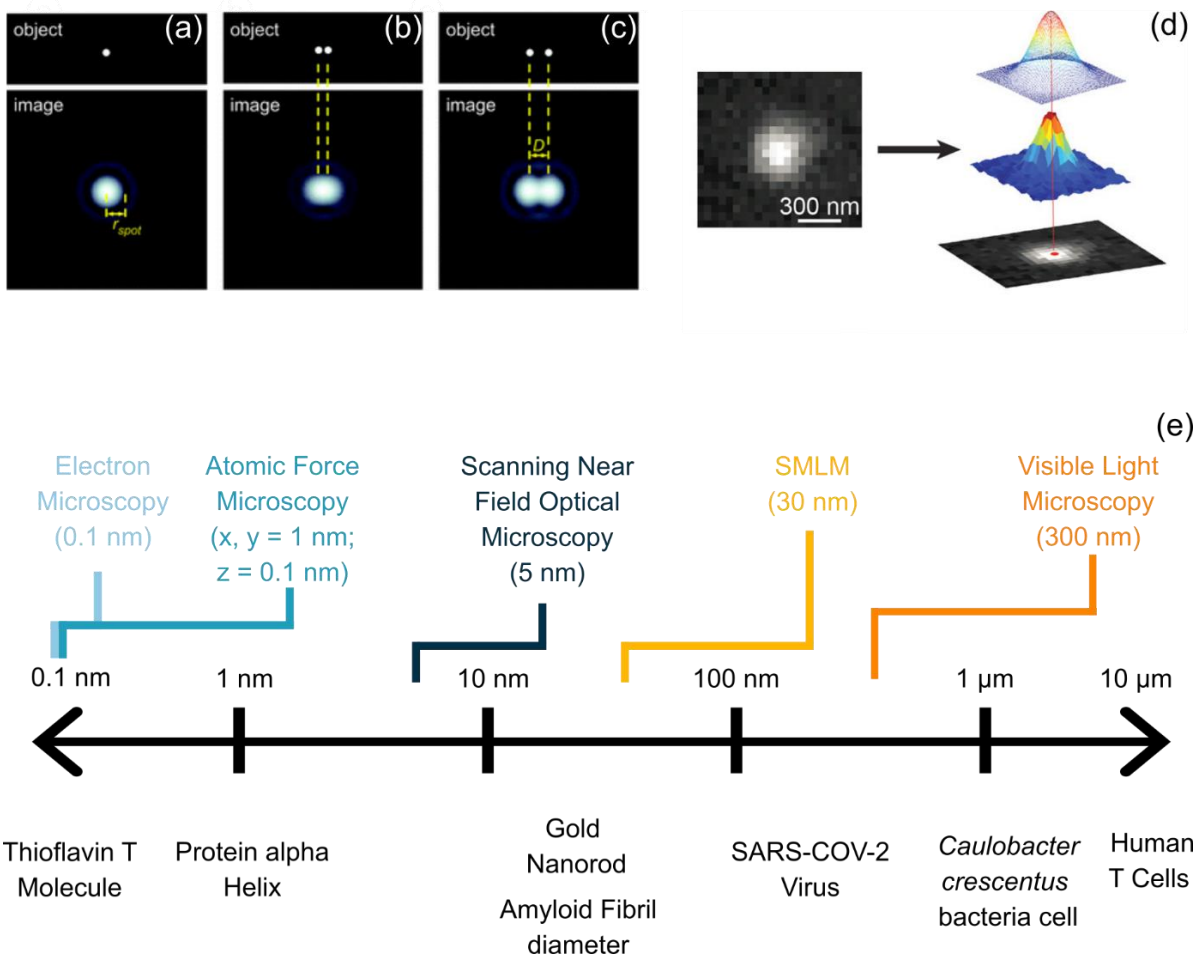

Figure 1.4: Resolution limits and localization microscopy.
(a–c are adapted from reference 50[50], d is adapted from 51[51]) (a) Simulated diffraction spot from a point emitter with marked radius to the first Airy minima, r_{spot} (b) Image of two point emitters that are unresolved (c) Image from two point emitters that are resolved. ($D = \frac{0.61\lambda}{NA}$) (d) Diffraction-limited image of a single molecule (left and bottom right) and two-dimensional Gaussian (top right). (e) Length scales of different structures relevant to this thesis or widely investigated by SMLM techniques also with the lower limits for different types of microscopy.

One way to obtain high-resolution images is to lower the wavelength in equation (1.6). Developed in the 1960s, electron microscopes use a stream of electrons, lowering the wavelength in equation (1.6), to achieve extremely high resolutions down to even angstroms with modern technology. Another method to achieve high resolution is to probe the near field with a tip sensitive

to electromagnetic fields. Near-field scanning optical microscopy (NSOM) uses special probes that can interact with electromagnetic fields to achieve single-nanometer resolution.

In the late twentieth and early twenty-first century, routes to achieve so-called "super-resolution" images at visible wavelengths were developed. One route is to shape a far-field excitation source such that the fluorescence emission comes from an area smaller than the diffraction limit. These techniques include STED (stimulated emission depletion) and SSIM (super-resolution structured illumination microscopy). A summary of various types of microscopy and their resolution limits is shown in Figure 1.3e.

Although the previously mentioned methods achieve incredible resolutions, they require complicated equipment and sample preparation. For example, electron microscopes operate in vacuum, which requires frozen biological samples, generally precluding *in vivo* imaging. NSOM and STED both are scanning techniques. Thus an n increase in resolution or the image size requires $n \times n$ more pixels in the x and y directions, so the acquisition time scales with area, which can limit their use.[52]

Single-molecule localization microscopy (SMLM) achieves resolution beyond the diffraction limit with the same conventional fluorescence microscope equipment as typical diffraction-limited fluorescence microscopy through the use of image sparsity. We fit the PSF of a single emitter to a two-dimensional Gaussian function which approximates the Airy disk very well (Figure 1.4d). We know the center position of this Gaussian with a precision in the x and y directions (the lateral precision) that scales with the inverse square root of the number of photons we detect. Modern electron-multiplying charge-coupled device (EMCCD) cameras are cooled to eliminate dark current, making the main source of noise photon shot noise, a noise source that

results from photons hitting the detector at different times. For such a case, a theoretical expression for the lateral precision, Δx of the measurement of the Gaussian maximum is[53]:

$$\Delta x = \sqrt{\frac{s^2 + \frac{a^2}{12}}{N} + \frac{8\pi s^4 b^2}{a^2 N^2}} \tag{1.7}$$

where a is the detector pixel size, b is the background noise per pixel, s is the standard deviation of the model PSF, and N is the number of photons detected.

In the limit of low background noise

$$\langle \Delta x \rangle \propto \frac{1}{\sqrt{N}} \tag{1.8}$$

With typical organic dyes or fluorescent proteins, precisions down to 20−30 nm are achievable, which represents an order of magnitude improvement on the localization precision of a conventional fluorescence microscope.[54,55]

To do this fitting, however, we must have a way of making sure we image just one point emitter, or molecule, at a time within a diffraction-limited area. To accomplish this sparsity, we need a switch to turn on and off the fluorescence from a more dense collection of molecules. Most super-resolution approaches use a stochastic switch; these stochastic methods include Stochastic Optical Reconstruction Microscopy (STORM)[56], Photoactivated localization microscopy (PALM)[57,58], and PAINT (Points Accumulation for Imaging Nanoscale Topography)[59]. The main methods I use in this thesis are different types of PAINT, in which I image one molecule at a time by relying on the adsorption and desorption of fluorophores to and from the surface.[60] Molecules diffusing in solution are motion blurred and contribute to a flat and constant background, while adsorbed molecules will be bright spots that can be fit to a 2D Gaussian. I also use a form of

PAINT microscopy, termed transient amyloid binding, which relies on the fluorogenic nature of amyloid-binding dyes like Thioflavin T. When integrated into an amyloid protein, these dyes become rigid and their quantum yield increases drastically.[54,55] This property allows high contrast between the dyes bound to an amyloid versus those diffusing freely.

1.2.3 Polarized-light Microscopy

Several microscopy techniques modulate light polarization to gain additional information about a sample. These include but are not limited to linear birefringence, differential interference contrast, and diattenuation.[61–63] In the context of fluorescence microscopy, polarization is important for the photoselection of the dipole moment of a fluorophore. It was first shown by Franz Weigert in 1920 that fluorescence could be polarized.[64] Levshin and Vaivlov then developed a theory explaining why fluorescence is polarized.[65]

The basics of the theory are that every fluorescent molecule has a transition dipole moment that describes the probability of promoting the molecule to a singlet electronic excited state. Malus's law[66] tells us that this absorption probability depends on the angle between the excitation field polarization vector and this transition dipole moment according to the following equation:

$$P \propto (\boldsymbol{\mu} \cdot \boldsymbol{E})^2 \propto \cos^2(\theta) \tag{1.9}$$

Here, θ is the angle between the transition dipole moment ($\boldsymbol{\mu}$) and the excitation electric field ($\boldsymbol{E}$). Equation (1.9) tells us that the absorption probability is maximized when the transition dipole vector and the excitation field are parallel and it is null with they are orthogonal. The consequence of this dependence on θ is that when using linearly polarized excitation, molecules that are aligned to the polarization field most often get excited.

Photons emitted during a radiative dipole fluorescence transition are polarized parallel to the molecule's transition dipole moment. The consequence of this is that the molecule's fluorescence emission will be linearly polarized if the molecule does not rotate during the time of acquisition and in the absence of any external perturbations. The absorption transition dipole moment and emission transition dipole moment are often parallel, particularly in π-conjugated fluorescent molecules like those used in this thesis. This property has led to widespread applications of polarized fluorescence microscopy to determine orientation and order in biological systems because the difference between the absorption and emission dipole moments can report on rotational diffusion.[67–69]

Polarized fluorescence has additionally been combined with microscopy to achieve the on-off blinking necessary to localize single molecules. One more widely known method using this principle is super-resolution by polarization demodulation.[70] In this method, modulating the intensity of fluorescent molecules with a rotating, linearly polarized excitation source separates the signal of differently oriented single molecules even when they are densely packed.

Recent work has extended polarization microscopy to encode information on the *z*- position of the emitter as opposed to just the azimuthal angle of the dipole. A few good references showing this work are [71,72]. Additionally, it has been shown that asymmetries in the external environment can modify the polarization of a fluorophore. For example, fluorescence from a molecule coupled to a plasmonic nanorod has been shown to appear polarized along the nanorod axis.[73,74]

1.3 Plasmonics for Enhanced Spectroscopy and Fluorescence

1.3.1 Localized Surface Plasmon Resonances

Plasmon modes are the collective oscillations of conduction band electrons in a metal.[75,76] There are several different types of plasmons. For example, the interface between metal films and dielectrics can support a surface plasmon polariton, which is generally coupled to a propagating wave by a grating or prism. This thesis focuses on localized surface plasmon resonances (LSPRs), which occur when the plasmon mode is confined to a small surface area. Noble metal nanoparticles, which have small extinction coefficients, are good plasmonic materials. For example, gold and silver metal nanoparticles support strong LSPRs.[76,77]

LSPRs have many applications from chemical catalysis to creating structural color.[*,78,79] In this thesis, we examine a metal nanoparticle's ability to act as a nanoantenna when it supports an LSPR. When a propagating light wave resonant with the nanoparticle's LSPR frequency excites a plasmonic metal nanoparticle, the metal's conduction band electrons oscillate in phase with the excitation field. This LSPR generates a local electromagnetic field with enhanced intensity in the near-field of the particle, efficiently converting the far-field propagating wave to an intense near field that decays on the ~10 nm length scale from the particle surface.[80] This local electric field intensity can be hundreds of times greater in magnitude than the far-field source, and thus molecules in this local field will absorb more photons per unit time compared to molecules excited by a far-field propagating wave alone.

LSPRs have been used to enhance spectroscopic techniques like tip- and surface-enhanced Raman spectroscopy (TERS and SERS). The enhancement factors in these techniques can be

[*] Color resulting from light scattering rather than from absorption

$10^6 - 10^8$.[81,82] These incredible enhancement factors are possible from the electric field enhancement as well as electron transfer between the metal and molecules.[82]

1.3.2 LSPRs for Enhancing Fluorescence

In addition to TERS and SERS, LSPRs have been shown to alter the emission properties of fluorophores. The fluorescence quantum yield of a molecule is the ratio of the radiative rate to the sum of the radiative and non-radiative rates:

$$\phi = \frac{\gamma_{rad}}{\gamma_{rad} + \gamma_{nrad}} \tag{1.10}$$

Where ϕ is the quantum yield, γ_{rad} is the rate of radiative transitions, and γ_{nrad} is the rate of nonradiative transitions. Properties of the molecule itself affect these rates and thus the quantum yield.

Physical chemists often describe molecule energy levels as stationary solutions to Schrödinger's equation. For spontaneous decay to occur, however, the molecule must couple to a quantized electromagnetic field. From Fermi's golden rule, we can derive that the transition probability for spontaneous decay of a two-level system in SI units is:

$$\gamma = \frac{2\omega}{3\hbar\varepsilon_0} |\boldsymbol{p}|^2 \rho(\omega) \tag{1.11}$$

where ω is the frequency of the transition, $\boldsymbol{p}$, is the dipole moment, $\hbar$ is the reduced Planck's constant, ε_0 is the vacuum permittivity, and $\rho(\omega)$ is the local density of photonic states. For our purposes, the important piece here is that the spontaneous decay rate is proportional to the local density of photonic states (LDOS). In a vacuum, the local density of states will be that of the free-space quantized electromagnetic field which is related to the speed of light in a vacuum, c, by the following equation:

$$\rho_0(\omega) = \frac{\omega^2}{\pi^2 c^3} \tag{1.12}$$

In the presence of a resonator, like an LSPR, the LDOS is modified and the spontaneous decay rates are enhanced. We can call these enhanced decay rates Γ. Thus, we can formulate a new quantum yield for the molecule near the resonator according to the following equation:

$$\phi_n = \frac{\Gamma_{rad}}{\Gamma_{rad} + \Gamma_{nrad}} \tag{1.13}$$

We can relate these enhanced rates to the power radiated by a classic dipole with the following equation.

$$\frac{P_R}{P_{R0}} = \frac{\Gamma_{rad}}{\gamma_{rad}} \tag{1.14}$$

In this equation, P_R is the power radiated in the presence of an LSPR and P_{R0} is the power radiated without an LSPR. The ratio equivalencies of these quantities have been proven elsewhere.[83,84] The total power radiated will thus depend on the enhanced radiative rate, Γ_{rad}, and the enhanced non-radiative rate, Γ_{nrad}. The main result here is that if the enhancement in the radiative rate of the molecule coupled to the plasmonic nanoparticle is greater than the enhancement in the non-radiative rate Γ_{nrad} due to thermal losses to the metal, the fluorescence will have a net increase in quantum yield relative to the uncoupled molecule.

Our research group and others have shown that the modification of these rates depends on the distance and orientation of the molecule relative to the plasmonic nanoparticle.[73,85–88] As seen in Figure 1.5a, the non-radiative losses are greatest close to the nanoparticle surface, resulting in a quenching (a net decrease in intensity versus the intensity of the fluorophore in free space) of fluorescence from 0 – ~10 nm from the nanoparticle. The non-radiative enhancement decays more quickly with distance thus radiative rate enhancement dominates and the total emission is increased

at distances greater than 10 nm in Figure 1.4. The radiative rate enhancement also decays at further distances out to around 100 nm and the quantum yield eventually just becomes that of free space.

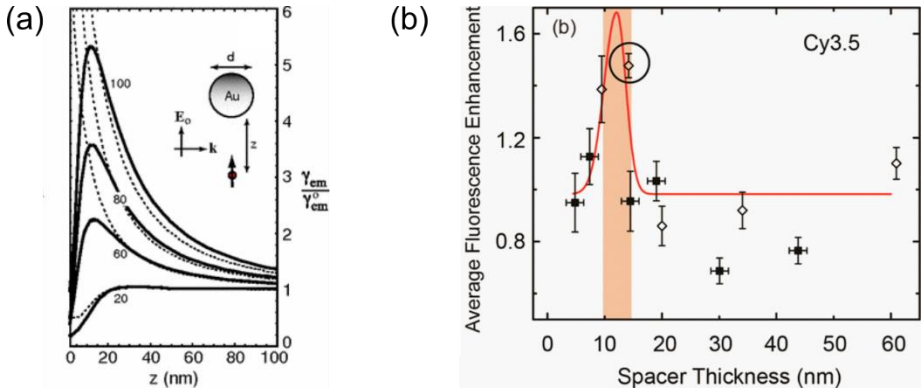

Figure 1.5: Distance dependence of radiative rate enhancement.
(a) Theoretical calculation of radiative rate enhancement of an ideal dipole as a function of distance from a gold nanosphere.[87] Black dotted lines are dipole approximations that fail at short distances. Black solid lines are calculated from the multiple multipole method. There are four lines for each of these methods at different nanosphere diameters, *d* indicated by the inset numbers. (b) Experimentally determined fluorescence enhancement as a function of spacer thickness to control the distance between Cy3.5 dye and a gold nanorod. Red line is a guide to the eye. The tan region shows the area of high enhancement.[85]

The result of emission enhancement at separation distances greater than 10 nm and quenching at distances less than 10 nm is a useful rule of thumb, but the reality is much more complicated. Things like the orientation of the emitter and particle geometry can influence the exact LDOS enhancement at any point in space. Indeed, much research into single-molecule plasmon-enhanced fluorescence from our group and others is concerned with unraveling these different effects.[73,74,80,86]

1.3.3 Chiral Plasmonic Enhancement

Plasmonic nanostructures can also create and enhance chiroptical signals.[89–91] The subfield of chiral plasmonics is the study of the manipulation and interaction of circularly polarized light with plasmonic structures.[92] A chiral plasmon mode is a plasmon mode that couples preferentially to

either LCP or RCP light, resulting in a differential absorption or scattering intensity.[93] To understand why a certain plasmon mode would be more easily induced by LCP or RCP light, consider an LSPR as a harmonic oscillator subject to the displacement force of the excitation light wave and the restoring force of the positive metal ions in the core.[93] For example, if the excitation wave is polarized along the long axis of a nanorod, the oscillation of the electrons will be stronger along this axis relative to the short axis. In the same manner, the surface current in a chiral spiral nanoparticle will oscillate more strongly when the handedness of the circularly polarized excitation wave matches that of the spiral. The opposite-wave excitation of the plasmon is hindered and will require more energy. A real-world plasmonic nanoparticle will have a much more complicated mode because of retardation and lightning rod effects, but the overarching principle applies.

An LSPR supported on a nanoparticle can also enhance chiroptical signals from nearby molecules because of the strong interactions between local electric and magnetic fields on the short length scales of evanescent waves.[94] An equation for the conserved quantity of optical chirality as formalized by Tang and Cohen (Section 1.1) is:

$$C = -\frac{\omega}{2c^2} Im(\mathbf{E}^* \cdot \mathbf{H}) = -\frac{\omega}{2c^2} |\mathbf{E}||\mathbf{H}| \cos(\beta_{\mathbf{iE,H}}) \quad (1.15)$$

where ω is the is the frequency of the light, c is the speed of light, $\mathbf{E}$ is the complex electric field vector, $\mathbf{H}$ is the complex magnetic field. $\beta_{\mathbf{iE,H}}$ denotes the phase angle. From equation (1.15), it is clear that the optical chirality will be maximized when the electric and magnetic fields have parallel components with a total phase difference that is an integer multiple of π.

Maintaining the above conditions of the phase difference for the electric and magnetic field, while bringing the electric and magnetic fields into close contact is a central problem for designing nanostructures that support LSPRs to enhance and induce chiroptical signals in nearby molecules.

Such a condition can be achieved with, for example, two offset nanoslits or a pair of offset nanorods (see Chapter 3).[94]

I recommend the works of Dionne, Okamoto, and Hentschel for further understanding of the chiroptical enhancement discussed in this thesis. These authors have shown promising experimental results demonstrating LSPR enhancement of chiroptical signals supported by theory.[19,95–97] Additionally, Lisa Poulikakos has strong work developing intuition for the physical relevance of the optical chirality quantity from the perspective of the intrinsic chiroptical interactions of the nanoparticle.[98–100]

1.4 Fabricating Chiral Plasmonic Systems

There are two major classes of methods to create chiral plasmonic nanostructures, top-down and bottom-up. In this thesis, I use two main methods for achieving nanoparticles that differentially interact with circularly polarized light. One is creating a chiral geometry with electron beam lithography (EBL) and the other is arranging nanoparticles created through wet chemistry synthesis on a chiral molecular template. These approaches are top-down and bottom-up, respectively.

1.4.1 Top-Down Approaches: EBL

EBL's major advantage is that arbitrary geometry may be created within the resolution of the instrument, which is typically 8 − 10 nm, and properties of the photoresist used. Direct scanning of an electron beam allows the creation of complex patterns similar to lithography. In my case, I use poly(methyl methacrylate) (PMMA, MicroChem), which limits us to a 20 nm feature size. Figure 1.5a shows my processing steps in EBL and 1.5b shows what a typical final EBL array looks like imaged on a dark-field microscope. The strong scattering color is easily visible in a color

photo. This method allowed me to study plasmonic nanoparticles with well-defined geometry which allowed me to simulate the known geometry for comparison.

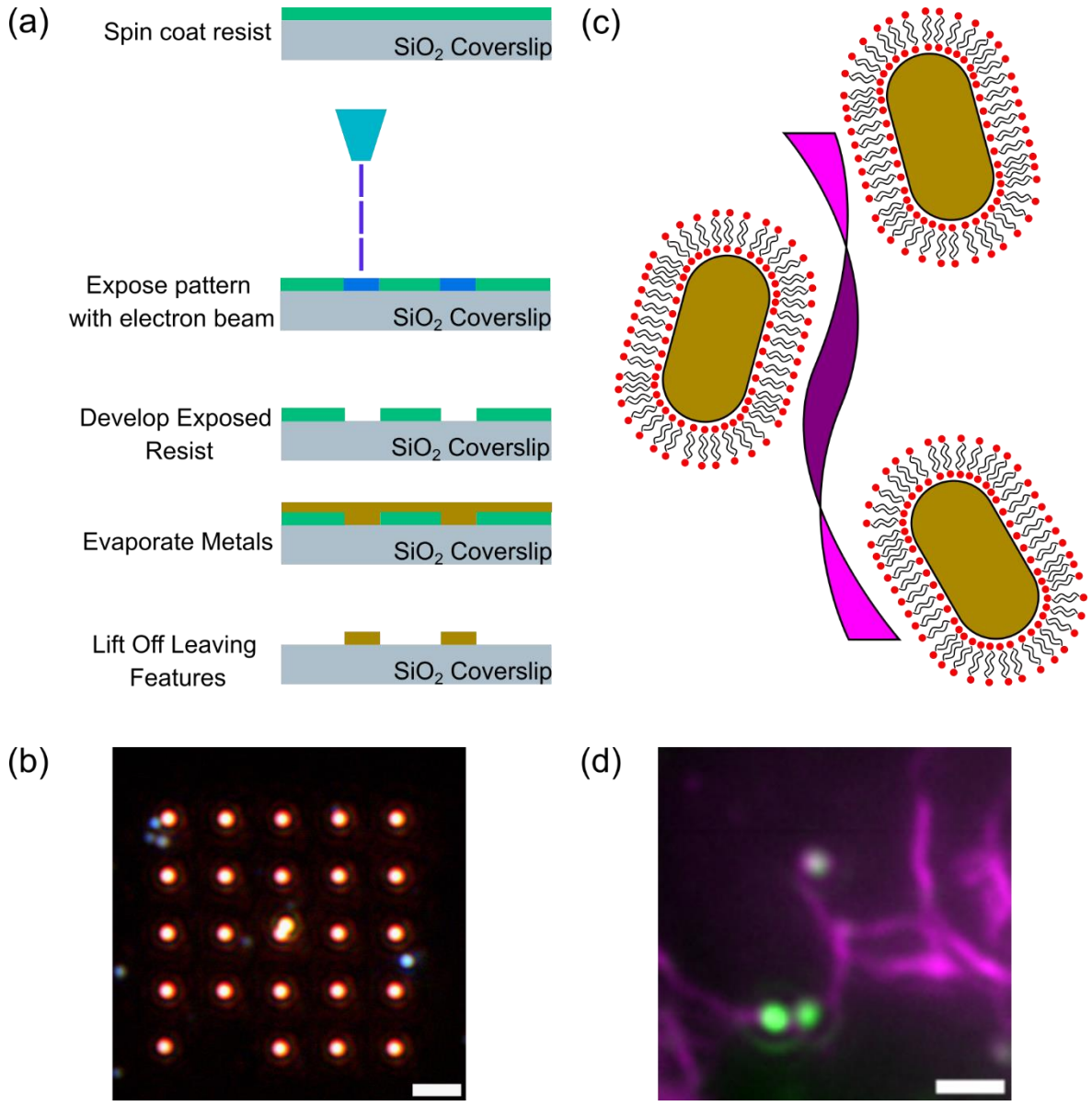

Figure 1.6: Methods for fabricating chiral plasmonic structures.
(a) E-beam lithography process steps (b) Dark-field microscopy color image of lithographically fabricated nanoparticles. Each red (700 nm) spot is one 100 nm × 60 nm gold nanorod. Scale Bar: 3 μm. (c) Diagram of CTAB-capped gold nanorods (rounded rectangles surrounded by red spots) binding to an amyloid (purple ribbon) in a spiral. (d) Composite fluorescence image of ThT-labeled fibrils (purple false color) with bound gold nanorods (green false color). Scale bars: 1 μm.

1.4.2 Bottom-Up Approaches: Amyloid Templates

Bottom-up approaches avoid the cost and labor-intensive nature of top-down approaches, though sacrifice some of the uniformity and tunability inherent to top-down structures. The bottom-up method described in this thesis achieves a chiral geometry by templating nanoparticles on natural chiral substrates from biomolecules. For this thesis, I employed electrostatic interactions for binding nanorods to a chiral template. Capping agents are molecules that allow the asymmetric growth of nanorods. In this thesis, I used cetyltrimethylammonium bromide (CTAB)-capped gold nanorods; CTAB is a detergent with a hydrophobic head and hydrophilic tail. Its positive tail sticks into an aqueous solution and additionally allows it to interact with the negatively charged backbone of the fibrils. A diagram showing Luis Liz-Marzán's lab's proposed helical geometry of gold CTAB-coated nanorods bound to amyloid is shown in Figure 1.5c.[101] A composite image of fluorescence insulin amyloid fibrils labeled with ThT excited at 488 nm and photoluminescence from gold nanorods bound to the amyloids excited at 640 nm is shown in Figure 1.5d.

1.5 Thesis Outline

This thesis extends our understanding of the interaction of fluorescent molecules with plasmonic nanoparticles to interactions that enhance signals related to molecular chirality, at the single-molecule, single-particle level. In **Chapter 2** of this thesis, I describe the construction of a polarization-resolved microscope set up for control of the excitation polarization and detection of the emission polarization state at the single-molecule level. I show that our system is capable of measuring the polarization state of emission from diffraction-limited single particles. I apply our instrument to resolve heterogeneities in printed silver nanohelicoids.

In **Chapter 3**, I show that the optical chirality conserved quantity is correlated with the emission pattern of coupled fluorescent molecules near a gold nanodimer. These results demonstrate how the emission from a coupled dye-nanoparticle system is modified compared to a dye emitting on its own. In particular, I measured a very low sample set of only ~100 zeptomoles of molecules. It opens up possibilities to characterize a chiral nanoparticle's signal-enhancing abilities through a non-perturbative route.

In **Chapter 4,** I show experimentally achiral plasmonic nanoparticles form small chiral aggregates along amyloid fibrils and have a measurable CD signal when bound to fibril templates in collaboration with Olesiak-Bańska's lab at Wroclaw University of Science and Technology. In particular, we showed a measurable CD signal without the micron-scale order of nanoparticles proposed by Luis Liz-Marzán's lab. This study shows the power of circular polarization-resolved SMLM to bring deeper mechanistic insight to studies of plasmonic chirality. Additionally, it opens new routes for sensing the chirality of amyloid fibrils at the concentration level of single fibrils and protofibrils.

Finally, in **Chapter 5**, I propose future uses for the polarization-resolved microscope system and the methods I have developed. Particularly, I propose a study of the chiral amyloid that forms the scaffold for *Escherichia coli* bacteria by using plasmonic nanoparticles as a reporter for the *in vivo* characterization of fibril chirality and a method to extend the wavelength range of chiral emission enhancement with silver nanoparticles in aqueous environments.

Together, this work extends the abilities of light microscopes to measure the property of molecular chirality to the nanoscale and advance the field of chiral plasmonic to the single-molecule level.

Chapter 2
Methods for Single-Particle Polarimetric Microscopy†

2.1 Introduction

In this chapter, I describe the design and construction of a single-particle polarimetric microscope I used for many of the experiments in this thesis. I modified both the emission and excitation pathways of the microscope using liquid crystal variable retarders (LCVR). These LCVRs have several advantages over typical solid-state wave plates; they are switchable on the milliseconds (ms) timescale and tunable for different wavelengths. Additionally, I present an application of the polarimetric microscope system to characterize nanohelicoid particles fabricated by my collaborators in Dr. Nicholas Kotov's lab.[102]

2.1.1 Light Polarization and Manipulation

The polarization of light has been responsible for numerous scientific discoveries and has a long history that intertwines with microscopy and chemistry (Chapter 1). The property of

† *This chapter describes Zechariah Pfaffenberger's contributions to work under review as well as supplementary information from work published in J. Phys. Chem.C. I performed the experiments and analysis in Figures 2.2 – Figure 2.7 and Tables 2.1 – 2.3. Ji-Young Kim developed and performed the synthesis of the nanohelicoids (Section 2.4.1):*
Kim, J. Y.; McGlothin, C.; Cha, M.; Pfaffenberger, Z.; Emre, E. T.; Choi, W.; Kim, S.; Biteen, J.; Kotov, N. Direct Printing of Helical Metal Arrays by Circularly Polarized Light. ChemRxiv March 21, 2023. https://doi.org/10.26434/chemrxiv-2023-b342r.[102]
Pfaffenberger, Z. J.; Chattopadhyay, S.; Biteen, J. S. Far-Field Polarization Optics Control the Nanometer-Scale Pattern of High-Fluorescence Dissymmetry Emission from Achiral Molecules near Plasmonic Nanodimers. *J. Phys. Chem. C* **2023**. https://doi.org/10.1021/acs.jpcc.3c00467.[103]

polarization refers to the orientation of the oscillating wave in a beam of light.[‡] If the oscillation traces a line in a plane orthogonal to the propagation direction, the light is said to be linearly polarized (Figure 2.1a). This line can be at any angle relative to the *x*-axis (Figure 2.1a). The electric field vector in the orthogonal plane can be decomposed into orthogonal *x* and *y* components. For example, linear polarized light at 45° relative to the *x* axis results from equal amplitudes of the *x* and *y* components in phase. However, if a phase delay is introduced between the components, the resultant electric field vector twists (Figure 2.1b and c). In general, the field vector traces an ellipse in the plane perpendicular to the propagation direction when the phase delay is not an integer multiple of 180°. The special cases of $\pm 90°$ phase differences result in perfect circles. The phase delay of $-90°$ results in a clockwise rotation called right circular polarization (RCP, Figure 2.1b), and $+90°$ results in a counterclockwise rotation called left circular polarization (LCP, Figure 2.1c).

Here, I define circular polarization according to Hecht's convention: from the receiver's point of view looking back up the beam toward the source.[13] This convention means the handedness of a circularly polarized wave is defined by a right-hand rule: if you point your right thumb in the direction of propagation, your fingers will follow the direction of the electric field vector as it twists in time. Additionally, the phase difference is calculated from the *y*- component relative to the *x*- component.

[‡] Not all light is polarized. For example, light from an incandescent bulb is completely unpolarized.

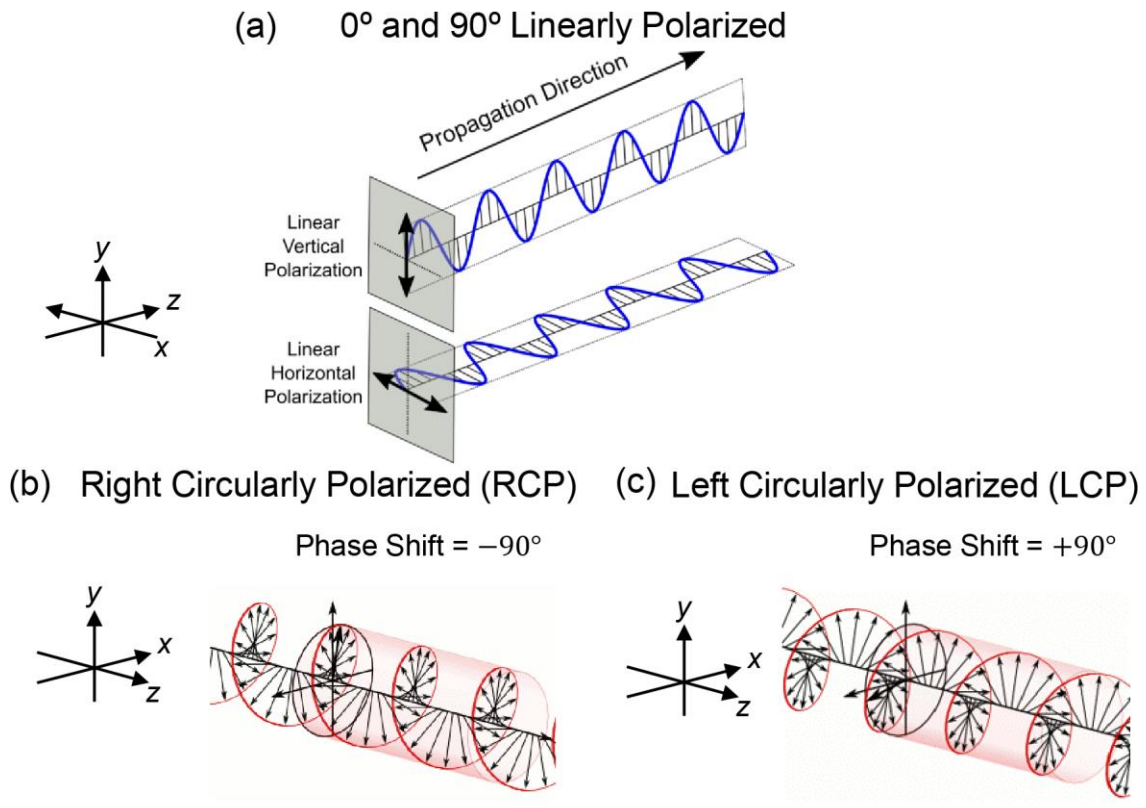

Figure 2.1: Diagrams of electric fields for various polarization states of a propagating light wave.
(a) Vertical and horizontal linearly polarized light waves. Blue lines show the oscillation of the wave and black double-headed arrows show the trace in a perpendicular plane. (b) Right circularly polarized light wave.[104] Red lines show the helix traced out by the vector over time and black arrows show the electric field vectors. (c) Left circularly polarized light wave. Lines and arrows denote the same things as in panel (b). Figures reproduced from reference 104.[104]

2.1.2 Stoke's Parameters

The most complete way to describe light polarization is with Stoke's parameters and Mueller calculus.[105] Jones matrices and calculus are also useful in the case of coherent radiation, but they cannot describe unpolarized light. The Stoke's vector, *S*, for a light beam is a 4 × 1 vector that can be written as follows:

$$S = \begin{bmatrix} S_0 \\ S_1 \\ S_2 \\ S_3 \end{bmatrix} = \begin{bmatrix} I_x + I_y \\ I_x - I_y \\ I_{+45^\circ} - I_{+135^\circ} \\ I_{RCP} - I_{LCP} \end{bmatrix} \tag{2.1}$$

In this equation, I_x, I_y, I_{+45°, and I_{+135° are the intensities of linearly polarized light along the $+x$, $+y$, $+45°$, and $+135°$ axes, respectively, and I_{RCP} and I_{LCP} are the intensities of RCP light and LCP light, respectively.[106] These intensities are physically measurable using a linear polarizer and a quarter wave plate.[107]

Mueller matrices, $\boldsymbol{M}$, are 4 × 4 matrices that describe how different optical components transform the input and output Stoke's vectors, S_{in} and S_{out}, respectively.

$$S_{out} = \boldsymbol{M} S_{in} \tag{2.2}$$

For example, a linear polarizer oriented along the *x*-axis is described by the following Mueller matrix:

$$\boldsymbol{M_{LP}} = \frac{1}{2}\begin{bmatrix} 1 & 1 & 0 & 0 \\ 1 & 1 & 0 & 0 \\ 0 & 0 & 0 & 0 \\ 0 & 0 & 0 & 0 \end{bmatrix} \tag{2.3}$$

And the output state of purely *x*-polarized light ($I_x = 1$, $I_y = I_{+45^\circ} = I_{+135^\circ} = 0$) through this linear polarizer can be found according to equation (2.2):

$$\boldsymbol{S_{out}} = \frac{1}{2}\begin{bmatrix} 1 & 1 & 0 & 0 \\ 1 & 1 & 0 & 0 \\ 0 & 0 & 0 & 0 \\ 0 & 0 & 0 & 0 \end{bmatrix}\begin{bmatrix} 1 \\ 1 \\ 0 \\ 0 \end{bmatrix} = \begin{bmatrix} 1 \\ 1 \\ 0 \\ 0 \end{bmatrix} \tag{2.4}$$

The polarization state of *x*-polarized light is unchanged by a linear polarizer oriented along the *x*-axis. If however, the input polarization is along the *y*-axis ($I_y = 1$, $I_x = I_{+45^\circ} = I_{+135^\circ} = 0$), the light intensity completely cancels out according to equation (2.2):

$$\boldsymbol{S_{out}} = \frac{1}{2}\begin{bmatrix}1 & 1 & 0 & 0\\ 1 & 1 & 0 & 0\\ 0 & 0 & 0 & 0\\ 0 & 0 & 0 & 0\end{bmatrix}\begin{bmatrix}1\\ -1\\ 0\\ 0\end{bmatrix} = \begin{bmatrix}0\\ 0\\ 0\\ 0\end{bmatrix} \quad (2.5)$$

The bottom right 3 × 3 elements of the Mueller matrix describe how the retardance of the light waves phase transform and thus are the main pieces that affect the elliptical polarization properties I am interested in for this thesis.

Several excellent resources for learning about Mueller matrix algebra and light polarization are Schoeche, Hong, and Hilfiker's review of Mueller matrix ellipsometry, Eugene Hecht's *Optics* textbook Chapter 8, and Edward Collet's *Field Guide to Polarization*.[13,105,106] These references all walk through the theory and practical aspects of polarization control. For future applications of this polarimetric microscope, I recommend gaining a strong understanding of Mueller matrix algebra through these resources.

2.2 Polarization State Generator (Excitation Pathway)

2.2.1 Excitation Pathway Design

One of the main hurdles I had to overcome to perform the experiments in this thesis was to precisely control the polarization of the excitation source, which is a solid-state continuous wave laser (Coherent CUBE 640-40C). Many types of lasers, including the laser I used, emit linearly polarized light.[108,109] Therefore, I used a set of optics to convert the laser polarization state from linearly polarized to circularly polarized or generally any elliptical polarization state. I chose Thorlabs Liquid Crystal Variable Retarders (LCVRs, Model Numbers LCC1223T-A and LCC1413-A) for this purpose because it is tunable for wavelengths from 350– 700 nm and has a switching time on the order of ms (Figures 2.2a and Figure 2.3).

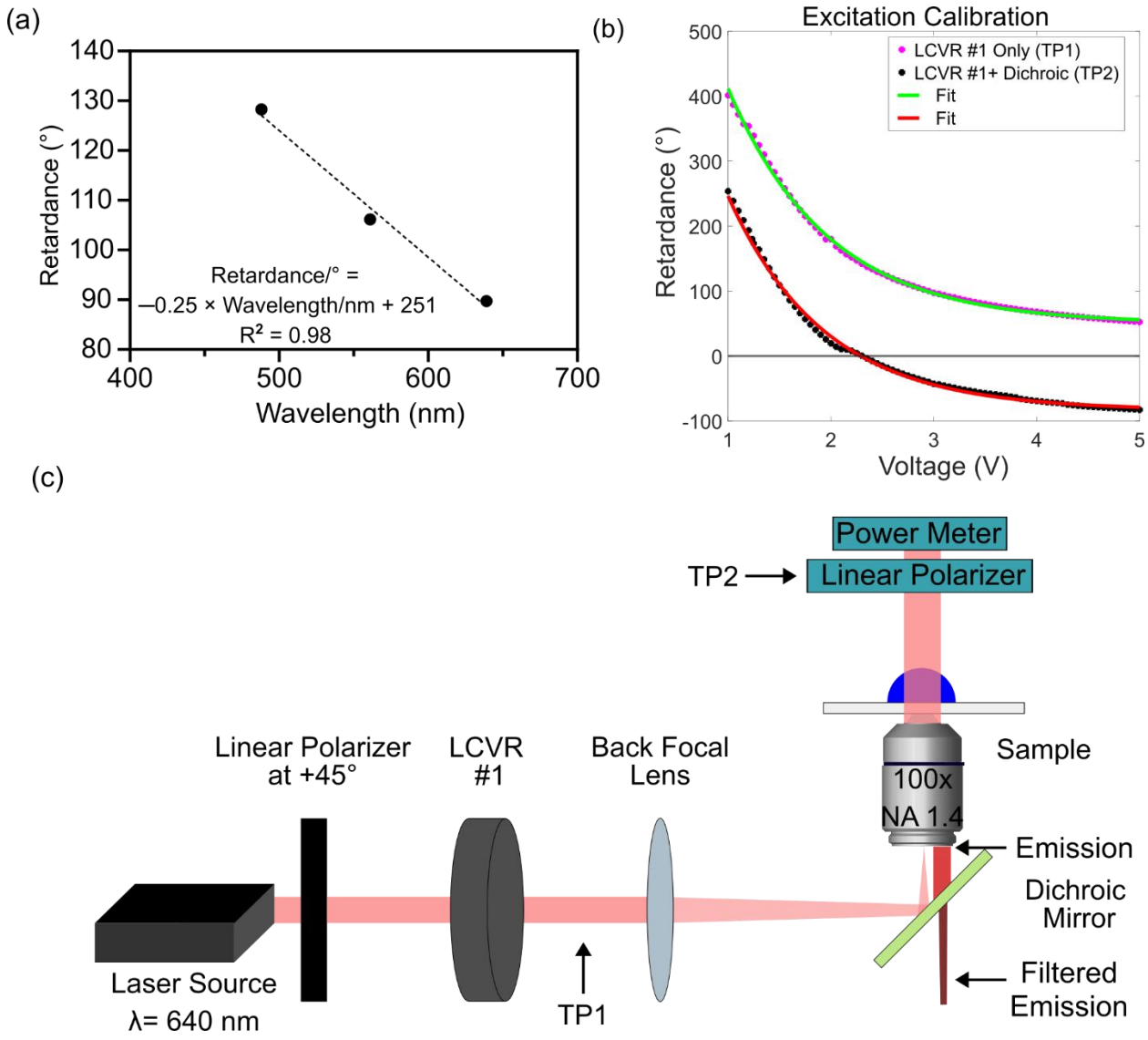

Figure 2.2: Characterizing microscope excitation polarization.
(a) The measured retardance of LCVR #1 without the dichroic (measured at TP1 in panel c) at a fixed voltage (2.5 V) for three laser wavelengths. The line and equation are best fit by a simple linear regression as the wavelength response is expected to be linear in this voltage range according to the manufacturer's data.[110] (b) Retardance of LCVR #1 measured at TP1 in panel c (pink dots) and retardance in the excitation path by LCVR #1 plus the dichroic mirror measured at TP2 (black dots). (c) Schematic of the excitation pathway showing test positions (TP) where the analyzer system was placed.[103,111]

I term all the optics needed for the precise polarization control the "polarization state generator" (PSG). In my setup (Figure 2.2c), I employed a half wave plate and linear polarizer to control the linearly polarized laser emission and rotate it to a 45° angle relative to the slow axis of

the LCVR (LCVR #1 in Figure 2.2) to generate circular polarization states. I can also generate linearly polarized light at any angle by setting the LCVR to half-wave retardance and rotating this combination of an achromatic half-wave plate and linear polarizer together. Indeed, with my PSG, any arbitrary polarization state may be generated at the microscope sample stage. This optics setup can enable many polarization-sensitive microscopy experiments in the future.

2.2.2 Error Introduced by Dichroic Mirror

Dichroic mirrors are an important part of a typical epifluorescence microscope system. The mirror's transmittance is a function of wavelength.[112] Therefore, a long-pass dichroic mirror can be selected to reflect the laser beam while transmitting the high-wavelength fluorescence emission (Figure 2.2c).

Dichroic mirrors possess linear birefringence.[113] Linear birefringence is the difference in the speed of light between linear polarizations oriented along perpendicular planes due to differences in refraction.[114] This linear birefringence changes the polarization state of light that reflects off the dichroic. Therefore, it is important to calibrate the PSG for the state generated *at the sample position.*

Two linear polarizers with orthogonal transmission axes are termed crossed polarizers. This configuration is useful for measuring the retardance properties of optical elements placed between the polarizer at 45° relative to the first polarizer's transmission axis by isolating the matrix elements associated with retardance.[115] I placed two crossed linear polarizers before and after the LCVR (at positions TP1 and TP2 in Figure 2.2a), scanned through voltages, and measured the output power from the second linear polarizer as a function of voltage. I converted the output power to retardance using a known phase unwrapping procedure to generate a voltage versus retardance curve (Figure 2.2b).[115] The dependence of the retardance on voltage is roughly

an exponential decay. I fit a single exponential with an offset to the data between 0.5 and 10 V to make predictions. Particularly, I found the appropriate voltages to attain phase delays of 90°, 180°, and 270°. At these important values, the LCVR acts as a quarter-wave, half-wave, and three-quarter wave plate, respectively, which allows us to generate both handednesses of circular polarizations and to rotate a linearly polarized light 360° relative to the *x* axis. The parameters found for the different LCVRs are tabulated in Table 2.1.

Table 2.1: Calibrated voltages and retardance for the LCVRs with 640-nm wavelength light as used in this thesis.

LCVR Model	Retardance (°)	Dichroic?	Voltage (V, from fit)	Voltage (V, Experimentally Measured)	Error
LCC1223T-A	360	Y	NA	NA	
LCC1223T-A	270	Y	1.121	0.950	15.3%
LCC1223T-A	180	Y	1.404	1.253	10.8%
LCC1223T-A	90	Y	1.768	1.595	9.8%
LCC1223T-A	0	Y	2.414	2.155	10.7%
LCC1413-A	360	N	0.984	NA	
LCC1413-A	270	N	1.272	NA	
LCC1413-A	180	N	1.713	1.700	0.7%
LCC1413-A	90	N	2.575	2.520	2.1%
LCC1413-A	0	N	13.400	12.500	6.7%
LCC1223T-A	360	N	1.162	1.170	0.7%
LCC1223T-A	270	N	1.485	1.490	0.3%
LCC1223T-A	180	N	2.010	1.960	2.5%
LCC1223T-A	90	N	3.141	3.150	0.3%
LCC1223T-A	0	N	NA	NA	

After calibrating the parameters needed for generating specific polarization states directly after the PSG, I placed the second linear polarizer and a photodetector at the sample stage by mounting them above the objective (TP2 in Figure 2.2a). Placing the second polarizer after the dichroic

allowed me to find the retardance of both the LCVR and the dichroic mirror. I again swept through voltages and measure the output power. Using the same procedure to correct the phase, I got a curve of retardance versus voltage and fit the data to a single exponential decay based on the data provided by the manufacturer (Figure 2.2b).[110]

This procedure will need to be performed for each laser wavelength used in future experiments as the LCVR response is wavelength-dependent (Figure 2.2a). I fit my data to a linear curve over the wavelength range from 488 – 640 nm as the wavelength response is linear in this range based on the data from the manufacturer.[110] Longer wavelengths experience a lower retardance than shorter wavelengths through this LCVR at a fixed voltage.

2.2.3 LCVR Switching Time Measurements

In future experiments, I recommend generating additional excitation polarization states and to measure all the Stoke's parameters of the fluorescence emission (Section 2.3). These additional parameters will help clarify relative contributions[116] from enhanced linear dichroism, circular dichroism, and other chiral light-matter interactions and for induced and enhanced circular polarization spectroscopies (Chapters 3 and 4). To obtain these parameters, one needs to modulate the retardance of the LCVR. It takes a certain amount of time for the liquid crystal molecules to reorient in the LCVR: after the voltage is changed, the retardance state of the plate gradually reaches the new value.[110,117] This switching time ranges from 1 to 100 ms. Several factors affect the switching time, including temperature (higher temperatures result in a faster switching time) and operating voltages (switching between higher voltages will be faster than switching between lower voltages). The electron-multiplying charge-coupled device (EMCCD) camera exposure times in the experiments in this thesis are on the order of tens of ms. Therefore, the first step for

measuring the complete Stoke's parameters is to characterize the switching times for the different voltage transitions needed to switch and measure the S_1, S_2, and S_3 parameters.[117]

In Figure 2.3, I show a curve of measured intensity versus time obtained from a photodiode while switching the retardance of the LCVR between 0° and 90° which corresponds to a transition from measuring S_1 to S_3. I calculate the response time as the time it takes for the curve to change from 10% to 90% of the maximum intensity.[117,118] This is a common metric for determining the switching time of liquid crystal devices. A summary of the switching times I measured for different transitions is presented in Table 2.2. The voltages are indicated in the table as resulting in the high intensity or the low intensity from Figure 2.3. Two of the transitions presented switch the PSG to change the excitation polarization at the sample stage. This sort of modulation could be useful in studies involving the differential absorption of circularly polarized light.

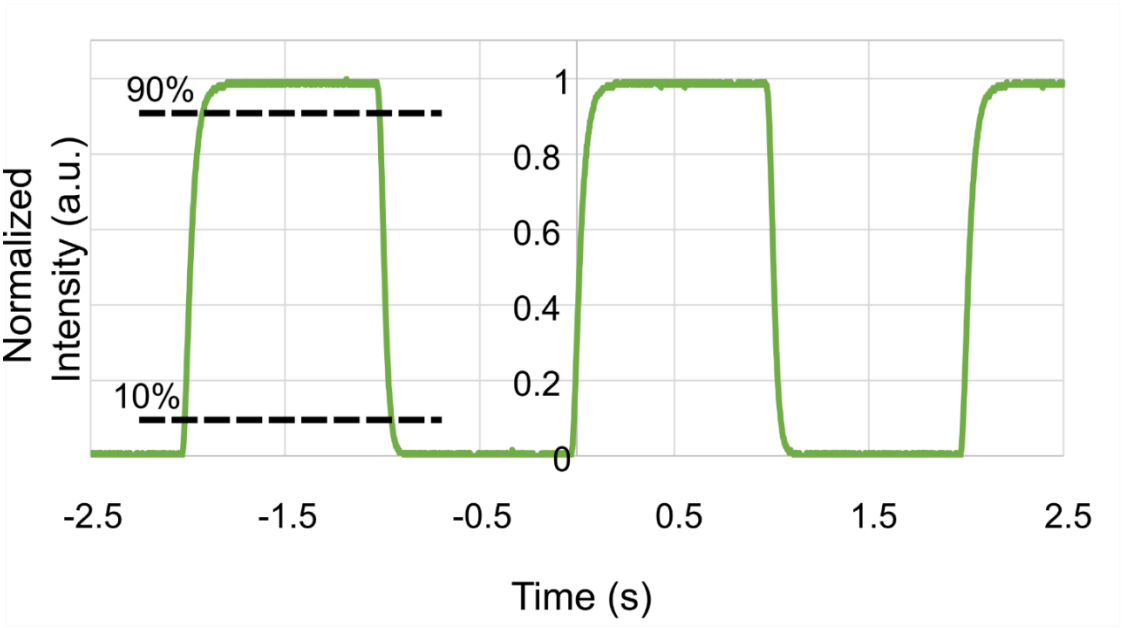

Figure 2.3: LCVR Switching Time Measurement.
Power transmitted through crossed polarizers and LCVR measured on a photodiode as a function of time. The black lines denote the values to calculate the rise and fall times for the transition.

Table 2.2: Measured switching times for various retardance transitions of the LCVRs used in this thesis.
Data is taken using the 640-nm laser.

LCVR Model No.	High-intensity Voltage (V)	Low-intensity Voltage (V)	Retardance Difference (°)	Rise Time (ms)	Fall Time (ms)	Transition
LCC1413-A	12.500	2.520	90	35 ± 2	33 ± 2	S_1 to S_3 emission
LCC1223T-A	2.300	1.235	180	62 ± 2	31 ± 2	0° to 90° linearly polarized excitation
LCC1223T-A	0.950	1.590	180	82 ± 2	58 ± 2	RCP to LCP excitation

2.3 Emission State Analyzer

2.3.1 Emission Pathway Design

The second important part of my polarimetric microscope system is a device to measure the polarization state of the fluorescence emission from a microscope. I refer to this device as the emission state analyzer (ESA). I initially coupled a single linear polarizer to a second LCVR for this purpose. This configuration allowed me to access only one polarization intensity measurement at a time, thus reducing the signal-to-noise ratio, and required switching the retardance of the LCVR to obtain the polarization components needed, resulting in a longer experiment. Therefore, I updated the design with a polarizing beam displacer (PBD) to obtain both LCP and RCP components in one camera frame.

A diagram of the final polarimeter setup using a PBD is shown in Figure 2.3. In Figure 2.3(a), LCP emission from the microscope enters the LCVR set to quarter-wave retardance and is converted to linearly polarized emission at +45°. RCP emission enters the LCVR and is converted

to linearly polarized emission at +135°. Thus, the LCP and RCP components of the emission are now orthogonal linear components and can be separated by the PBD into two images on an EMCCD camera.

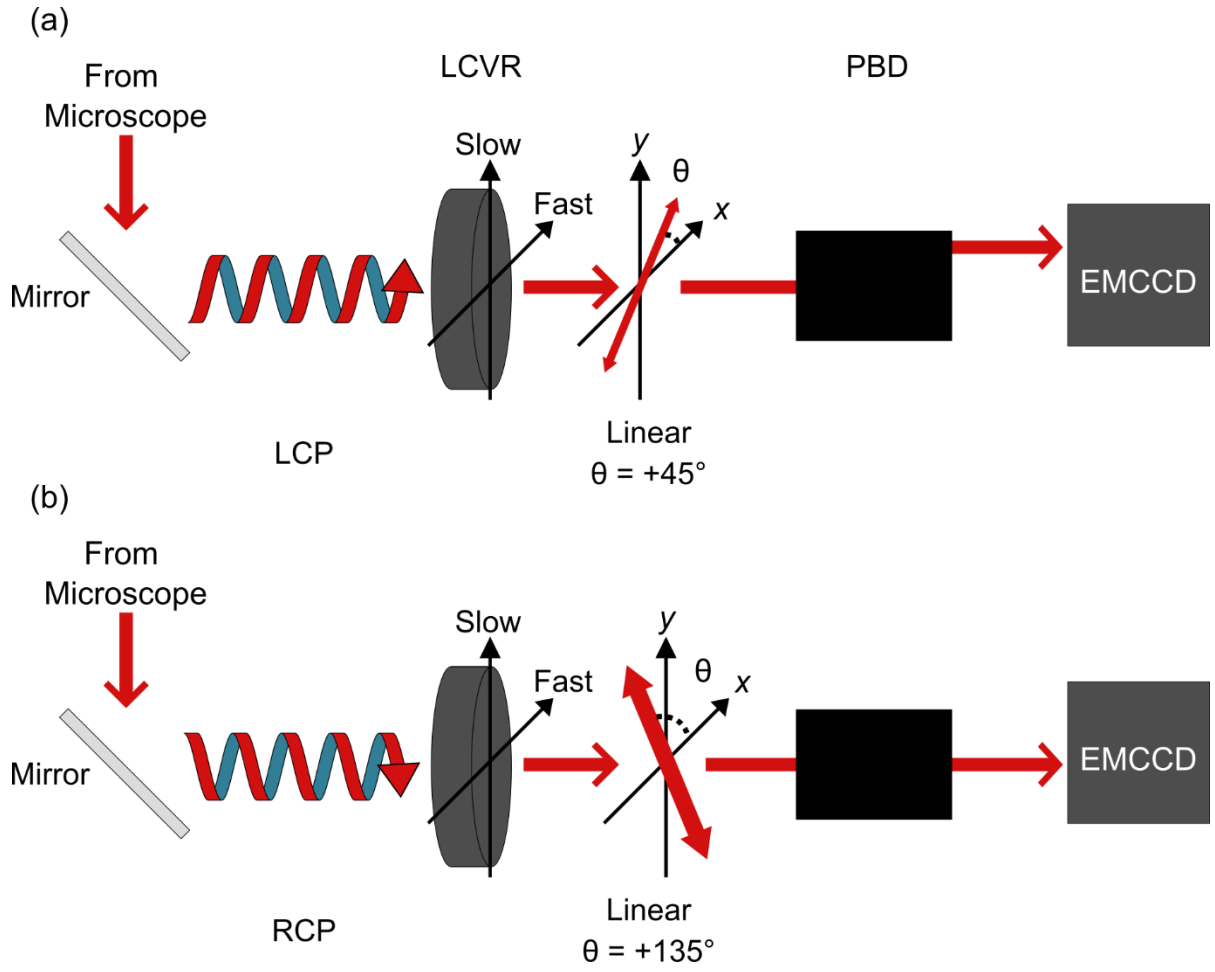

Figure 2.4: Optics diagram of polarimetric microscope system and the emission polarization state.
(a) LCP light entering the polarimeter will be converted to linearly polarized light at θ = +45° and thus be deflected by the PBD. θ is the angle of the linear polarization in the *xy* plane relative to the *x*-axis. (b) RCP light entering the polarimeter is converted to linearly polarized light at θ = +135° and thus will not be deflected.

2.3.2 Demonstration of the LCP and RCP Channels in the ESA

To determine if the polarimeter was performing as predicted, I used circular polarizers to convert any input polarization to LCP or RCP light at several test points in the microscope setup (Figure 2.4a).

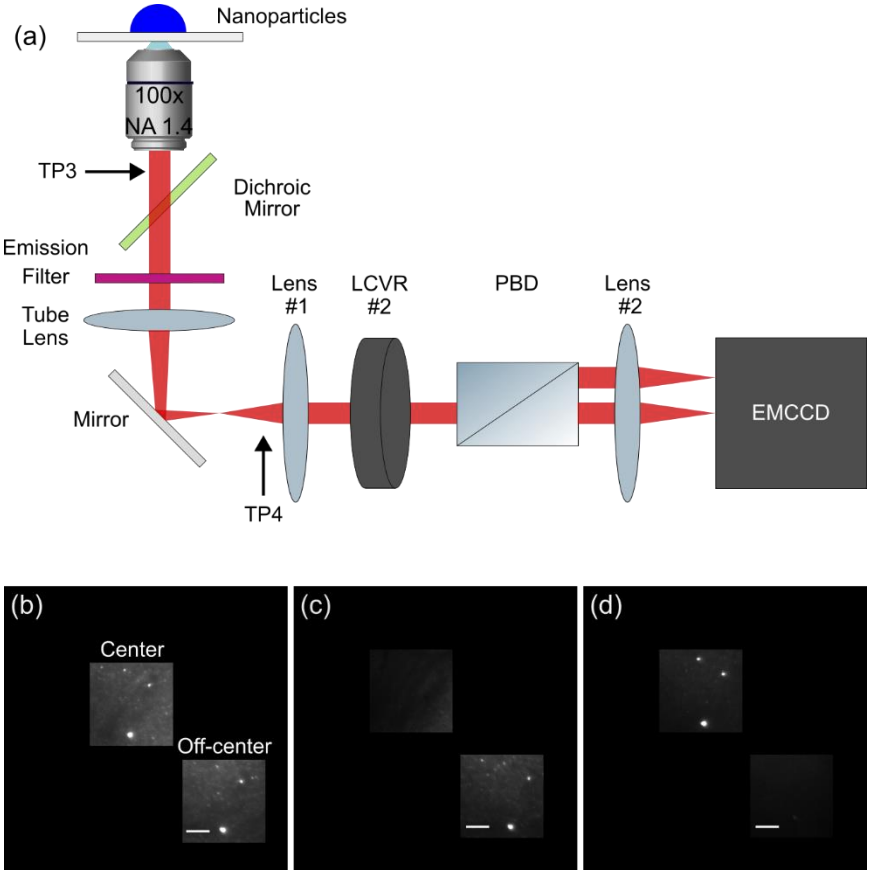

Figure 2.5: Determination of emission polarization.
(a) Schematic of the emission pathway showing test positions TP3 and TP4. (b)–(c) Determination of polarization channels using fluorescent beads. (b) Images of fluorescent beads under 640-nm excitation with no additional polarization optics; the emission is collected for wavelengths greater than 655 nm and split into an on-center channel and an off-center channel with a polarizing beam displacer (PBD, panel a). (c) Image of the same sample with a left-handed circular polarizer (LHCP) at position TP4. (d) Image of the same setup with a right-handed circular polarizer (RHCP) at position TP4. Scale bars: 4 μm; all images are on the same colorscale.

Figure 2.5 shows images of fluorescent beads (TetraSpeckTM microspheres 0.2 μm, ThermoFisher Catalog Number T7280). The emission from the beads themselves is unpolarized. To determine how the optic system affects polarization, we put known polarizing optics in the pathway at various test positions (TPs). In the absence of a circular polarizer in the emission pathway, the fluorescent beads show a signal in both channels with a 1:1 ratio on the camera when a quarter-wave potential is applied to LCVR #2 (Figure 2.4b). When an LHCP (Edmund optics #88-098) was introduced at TP4, the fluorescent bead signal was almost entirely in the off-center channel (on-center/off-center intensity ratio = 1/10; Figure 2.4c). When an RHCP (Edmund optics #88-101) was introduced at TP4, the fluorescent bead signal was almost entirely in the on-center channel (on-center/off-center intensity ratio = 10/1; Figure 2.4d).

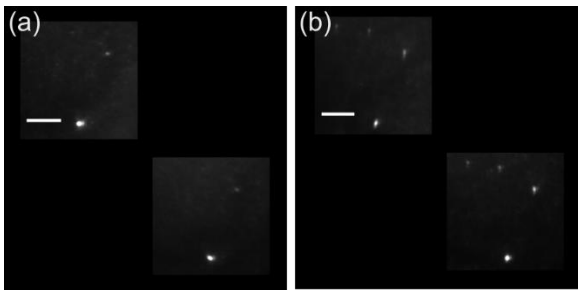

Figure 2.6: Circularly polarized emission test images.
Images of fluorescent beads when (a) an LHCP, or (b) an RHCP is placed in position TP3 of Figure 2.4a. Scale bars are 4 μm; All images are on the same colorscale.

When an RHCP is placed between the objective and the dichroic at position TP3 of Figure 2.4a, the fluorescent bead intensity is greater in the off-center channel than the on-center channel (on-center/off-center intensity ratio = 1.6/1). When an RHCP is placed at position TP3 of Figure 2.4a, the fluorescent bead intensity is greater in the on-center channel than in the off-center channel (on-center/off-center intensity ratio = 1/1.6). Therefore, we define I_{RCP} to be the intensity in the off-center channel and I_{LCP} to be the intensity in the on-center channel.

The flipped and reduced ratio of intensities between TP3 and TP4 results from ellipticity introduced by the optics (including the tube lens and output mirror) in the emission pathway. We are, however, still able to discriminate between left circularly polarized (LCP) and right circularly polarized (RCP) emission with a 1.6/1 ratio, which allows us to analyze the relative circular polarization of molecules in our system. These distortions, together with additional errors from the high NA objective, broaden the distributions of single-molecule dissymmetry.

2.3.3 Future Methods for Calibration of the ESA

In this thesis, the characterization of emission presented in section 2.3.2 is enough to obtain significant results (Chapter 3). In the future, it will be important to characterize the microscope emission pathway to obtain more precise information on emission dissymmetry.[§,119] Finely aligning the optical components is difficult, and there will always be some level of error in the angles set between polarizers and wave plates due to the limitations of the optomechanical components. In the case of this particular polarimeter, additional errors could be introduced from the retardance of the LCVR deviating from a perfect quarter-wave retardance due to the broadband nature of fluorescence and because of the optics in the collection pathway of the microscope.

Methods for calibrating a polarimeter generally involve placing a known polarization optic into the path as a test sample. For example, you can place a linear polarizer or a solid-state quarter wave plate just before the polarimeter and measure the various Stoke's parameters as a function of the angle of the optic.[120] You can then compare these measured Stoke's parameters to the calculated theoretical values of an ideal polarimeter and obtain empirical error terms that you can

[§] Camacho's fluorescence anisotropy review[119] discusses the importance of characterizing errors in the microscope emission pathway. Particularly, section 8 discusses methods for characterizing and correcting polarimetric measurements in a microscope.

add to your intensity measurements to account for deviation of the retardance or misalignment of polarization optic angles.

In addition to errors in the polarimeter setup itself, distortions to the polarization state could be introduced by the collection pathway through the objective, dichroic, and microscope side port mirror (between the nanoparticle sample and TP4 in Figure 2.4). It is challenging to account for all of these distortions for single fluorescent molecules because the molecules are at the focal plane of the objective thus preventing placement of any polarization optics in this space.[71,113,119,121,122] Therefore, the only way to calibrate the polarimeter at the sample plane is to find the Mueller matrix for the emission pathway up until the ESA. This requirement to measure the Mueller matrix of polarimeters in various reflectance configurations has led to the development of eigenvalue calibration methods (ECMs).[123] Such methods are performed by generating known polarization states, sending them through known calibration samples, and measuring the output polarization with your polarimeter. One takes measurements with the test samples at various locations in the optic pathway until they have enough values that the Mueller matrices for the various pieces of the path become overdetermined. At the end of the procedure, you have the Mueller matrix for the PSG, ESA, and the optics system in between them. In this case, the optics system is the widefield microscope consisting of the back focal lens, dichroic mirror, objective lens, tube lens, and output mirror (Figure 2.4). One way to measure intensity at the sample plane is by placing a mirror on top of a glass coverslip and measuring the changes to the polarization of the excitation laser itself as it reflects through the emission pathway. One disadvantage to this method is that you cannot have the emission filter in so you are calibrating at the excitation wavelength rather than the specific fluorescence wavelengths of interest. However, my analysis of the retardance as a function of wavelength shows that the retardance only changes by 10° over a 40 nm range. One should

consider the bandwidth range they are collecting and whether the deviation of the retardance will majorly affect the experiment.

2.4 Characterizing Silver Nanohelicoids with Circularly Polarized Luminescence

One of the first applications of my ESA was done in collaboration with Dr. Nicholas Kotov's group in the Chemical Engineering department at the University of Michigan. Dr. Ji-Young Kim in the lab had developed a technique to 3D print helical nanostructures that exhibit a strong chiroptical response. I present here my contribution to this study where I measured the polarization state of the photoluminescence emission from samples Ji-Young prepared.[102] These experiments were done with the preliminary version of the ESA consisting of a single linear polarizer coupled to an LCVR.

2.4.1 Methods for Preparation and Circularly Polarized Luminescence Characterization of Nanohelicoids

To synthesize the silver helicoids, silver nitrate ($AgNO_3$, Cat.# 209139) and trisodium citrate dihydrate (Cat.# S4641) were purchased from Sigma-Aldrich (Milwaukee, WI). Ultrapure water from a Direct-Q3 system (18.2 MΩ·cm, Millipore; Billerica, MA) was used in this work. A glass coverslip substrate was submerged in a solution of silver precursor ($AgNO_3$, 2.5 mM) and citrate (12.5 mM), while the height from substrate to surface of the solution was fixed at 3 cm. Three different lasers (wavelength of 405, 532, and 660 nm), modulated to emit either left- or right-circularly polarized light (LCP light and RCP light, respectively), were directed perpendicular to the substrate with varying power density for different times up to 30 minutes depending on the purpose of experiments. The substrates illuminated with LCP light are referred

to as Δ-helicoids and those with RCP light as Λ-helicoids. The patterned substrates were immersed in a DI water solution and washed three times before imaging analysis.

Helicoids were prepared on glass coverslip substrates as described in the above section and imaged by single-particle spectroscopy.[80] 80-nm diameter spherical Au nanoparticles (AuNPs, Nanopartz) were drop cast on glass coverslips as an achiral reference sample. Sparse arrays of helicoids or AuNPs were excited by a 488-nm continuous wave (CW) laser source on an Olympus IX71 microscope equipped with a 100× Olympus UPlanFL N objective. The excitation was randomly polarized using a depolarizer (Thorlabs DPP25-A). Excitation intensity: 3.87×10^5 mW/cm^2. Red-shifted luminescence was collected in epifluorescence geometry with a 505 nm long-pass dichroic and a 505 nm long-pass filter. The circular polarization of the emission was analyzed by transmission through a liquid crystal variable retarder (LCVR, Thorlabs LCC1223T-A) followed by a linear polarizer with its transmission axis oriented at −45° relative to the slow axis of the retarder. After expansion with a 3× beam expander, the image was formed on an electron-multiplying charge-coupled detector camera (Andor iXon3). The LCVR was switched between 90° and 270° retardance at 10 Hz and synchronized with the camera acquisition time (50 ms) with a 50 ms delay between frames to allow for the LCVR switching time. By altering the LCVR retardance, I selected RCP emission at 90° retardance and LCP emission at 270°, taking into account the reflections in the microscope.

Tiff stacks of 100 imaging frames were collected and the images were analyzed in Fiji.[124] A flat-field correction was applied, then a median projection in time of the video stacks was taken. Single particles were identified in these average images by thresholding to visualize the top 0.5% brightest pixels and identifying bright spots that comprised 20 pixels with brightness above the threshold and for which the luminescence was detectable over the course of the whole movie in

both polarization channels. Ten particles were therefore selected for analysis in each of the helicoid samples and three 80-nm spherical gold nanoparticle control particles were analyzed. The emission dissymmetry g-factor, g_{em}, was calculated for each particle as:

$$g_{em} = 2\frac{I_{LCP} - I_{RCP}}{I_{LCP} + I_{RCP}}$$

where I_{LCP} and I_{RCP} are the time-averaged maximum pixel intensities of the particle in each odd (RCP) or even (LCP) imaging frame normalized by the median pixel intensity in a 1 μm by 1 μm box about the particle.

2.4.2 Single-particle Nanohelicoid Data

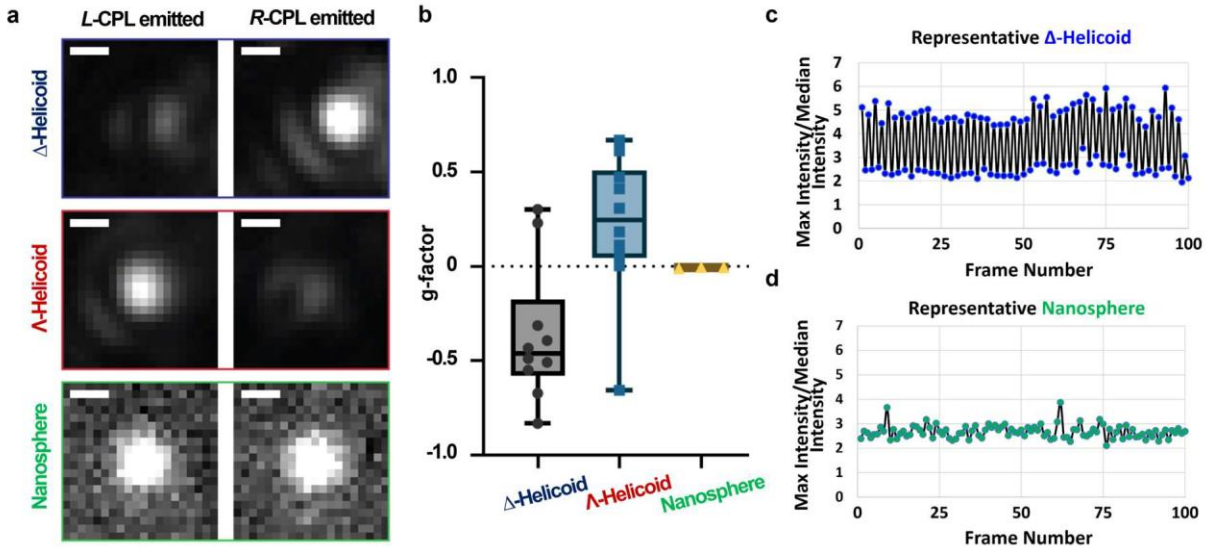

Figure 2.7: Single-particle analysis of chiroptical scattering from silver helicoids on substrate.
(a) Single-particle optical microscopy images of Δ-helicoids, Λ-helicoids, and AuNPs during collection of LCP or RCP emission upon excitation with randomly polarized 488-nm continuous wave laser light (scale bars: 250 nm); (b) Dissymmetry g-factor for Δ- and Λ-helicoids and AuNPs. Each point is a single-particle measurement. The control experiment with an achiral AuNPs shows nearly zero dissymmetry factor. (c) Repeated observations of the max intensity/median intensity of scattered light from a single Δ-helicoid and achiral nanosphere (odd frames: RCP detection; even frames: LCP detection).

The surface exposed to LCP light for 15 min (Δ-helicoids metasurface) started to have visible brightness variations between LCP and RCP emission (Figure. 2.6a). For further investigation of such scattering dissymmetry from helicoids, I measured the differential intensity from multiple single particles. I placed Δ- and Λ-helicoid samples prepared on cover slides under a randomly polarized focused laser beam at a wavelength of 488 nm and analyzed single-particle circularly polarized luminescence (see methods above for the details). As expected, single helicoids with different handedness displayed distinctly different circular polarizations (Figure 2.6b). The average dissymmetry *g*-factor reached as high as −0.33 for the Δ-helicoids, indicating that they emit RCP light stronger than LCP light, and vice versa for Λ-helicoids: g = +0.15 while the achiral AuNP shows nearly zero dissymmetry factor (Figure 2.6b, Table 3). The repeated observations of the circularly polarized emission intensities from a single Δ-helicoid compared to achiral nanosphere control over a hundred imaging frames demonstrates not only selectively polarized emission but also their robustness and photostability (Figure 2.6 c,d).

Table 2.3: Average single-particle g-factor calculated from circularly polarized luminescence measurements of Λ-helicoids and Δ-helicoids, with spherical (achiral) AuNPs as the control.

Sample	g_{em}	Standard deviation
Λ-helicoids	+ 0.2140	± 0.363
Δ-helicoids	− 0.3461	±0.350
AuNPs	− 0.0006	±0.003

2.5 Conclusions

I constructed a polarimetric microscope system capable of measuring the polarization state of nanoparticles. By performing several tests and calibrations, I ensured that I am correctly measuring the emission polarization state and that the excitation beam polarization is precisely

controlled. Additionally, I showed that I can measure polarization states from single nanohelicoid structures with a known chiroptical response.[102]

Chapter 3

Far-Field Polarization Optics Control the Nanometer-Scale Pattern of High Fluorescence Dissymmetry Emission from Achiral Molecules near Plasmonic Nanodimers

The work presented in this chapter was published in Journal of Physical Chemistry C. Pfaffenberger, Z.; Chattopadhyay, S.; Biteen, J. Far-Field Polarization Optics Control the Nanometer-Scale Pattern of High Fluorescence Dissymmetry Emission from Achiral Molecules near Plasmonic Nanodimers, *J. Phys. Chem. C.* 2023. https://doi.org/10.1021/acs.jpcc.3c00467[103]

3.1 Introduction

Chirality is an important feature in biology because the handedness of a molecule can determine its function. For example, the natural amino acids almost exclusively exist as L-enantiomers,[3] and this preference results in higher order structures that are also preferentially handed, such as right-handed α-helices within proteins.[125] On the other hand, the presence of the opposite enantiomer can be pathological. For example, the notorious story of birth defects from the drug thalidomide resulted from one molecular enantiomer having harmful biological effects.[126] Sensitive and specific detection of the chirality of a molecule is therefore needed to detect and avoid molecular pathologies.

Optical probes have long been used to probe the chirality of molecules; indeed Louis Pasteur discovered chiral molecular structure when he observed that tartaric acid crystals interact differently with the left circular polarization (LCP) vs. right circular polarization (RCP) of light.[10]

Spectroscopic techniques such as circular dichroism (CD) and optical rotatory dispersion (ORD) quantify the average chirality by measuring how chiral molecules interfere with the polarization of incident light: CD directly measures the differential absorption of left and right circularly polarized light while ORD measures the angle between the incident linear polarization and the transmitted linear polarization. However, CD and ORD require highly concentrated samples for detection above the noise floor due to the mismatch between the size of molecules (up to a few nanometers) and the wavelength of propagating ultraviolet or visible light (hundreds of nanometers).[15,127–129] Such low molecular signals limit the use of these techniques to large-volume samples and high concentrations in the 1 – 100 μM range.[89,97]

These length scales can be bridged by compressing or twisting the electromagnetic field. Tang and Cohen showed theoretically that the conserved quantity of optical chirality describes how electromagnetic waves couple to molecular chirality and predicted that certain standing waves could be constructed with an optical chirality exceeding that of a propagating circularly polarized wave.[17,18] It has since been demonstrated theoretically and experimentally that plasmonic nanostructures can act as antennas to generate these high optical chirality fields in their surroundings, and thus enhance absorption dissymmetry in nearby molecules.[19,20,130–133]

High-sensitivity fluorescence detection down to the single-molecule scale requires a nanostructured substrate that twists light enough to detect subtle differential absorption while minimizing the background signal sufficiently to isolate the fluorescence emission from a single molecule. Though plasmonic nanoparticles cannot intricately control electromagnetic fields to the same extent as metasurfaces, the background fluorescence from noble metal plasmonic nanoparticles is low enough to enable single-molecule localization.[76,80,134] However, plasmonic nanoparticles interfere with nearby fluorescent molecules to modify the detected fluorescence

pattern, creating an apparent mislocalization or mispolarization.[77,80,135,136] While chiral nanoparticles can increase the differential absorption, the coupling will also redirect the emission polarization.[74,137] The apparent fluorescence dissymmetry detected from a single molecule coupled to a chiral nanoantenna is therefore biased by the substrate, and even an achiral molecule will have apparent fluorescence dissymmetry upon coupling to a chiral nanoantenna. The induced single-molecule fluorescence dissymmetry and modified emission pattern of an achiral molecule must be quantified as the first step toward chirality sensing and chiral sources at the single-molecule level using chiral plasmonic substrates.

Ensemble measurements of achiral molecules near chiral plasmonic nanoantennas have provided a baseline for the induced dissymmetry.[138–140] In particular, these plasmonic particles have been shown to induce a fluorescence dissymmetry signal in nearby achiral infrared dye molecules by circularly polarized luminescence (CPL), which measures the difference in the emission intensities of LCP and RCP light.[139] This dissymmetry can be attributed to the directional coupling of the molecular fluorescence with the chiral substrate: though the molecular emission is linear (equal RCP and LCP emission intensities), the substrate preferentially re-radiates the RCP and LCP light into different hemispheres such that an apparent fluorescence dissymmetry is detected; this dissymmetry is equal and opposite in the forward and backward directions.[140] Accordingly, electromagnetic simulations predict a spatial dependence for the sign of the optical chirality over the volume of the structure: the induced emission dissymmetry will indicate more LCP emission in some sample regions and more RCP in other sample regions.[139] However, in such ensemble measurements, these diffraction-limited heterogeneities cannot be measured and the average experimental dissymmetry has a single sign. Experimental evidence is required to map

and quantify the heterogeneity in the induction of fluorescence dissymmetry due to emission coupling.

In this chapter, I use single-molecule super-resolution fluorescence microscopy to determine how the emission pattern and polarization of achiral dyes change in the near field of a chiral plasmonic nanoantenna. The goal of this approach is to control the near-field environment of single molecules based on the far-field excitation polarization and to measure the induced difference in fluorescence handedness using a far-field instrument. First, I implement a new single-molecule microscope to characterize the apparent fluorescence dissymmetry of nanomaterials with polarization-resolved super-resolution microscopy.[113,121,141] Next, I perform finite-difference time-domain (FDTD) electromagnetic simulations to calculate the differential far-field scattering spectrum and optical chirality near a chiral nanoantenna (a dimer of offset gold nanoparticles). With the single-molecule polarimeter, I measure the polarization information for each achiral fluorescent molecule (Cy5.5) with localization precision on the scale of 30 – 50 nm as single molecules adsorb near the nanoantenna.[60,142] These findings can guide the development of future platforms for ultrasensitive enantiomeric detection and generation of high-dissymmetry luminescence from small volumes.

3.2 Materials and Methods

3.2.1 Electron-Beam Lithography of Nanodimers

Glass microscope coverslips (24 × 40 mm, Fisher Scientific 12545D) were plasma cleaned with oxygen (Yield Engineering Systems, YES-CV200RFS) for 180 s. 200 nm poly(methyl methacrylate) (PMMA, MicroChem) electron beam resist was spin-coated onto the slips and an 8-nm gold layer was thermally evaporated (Angstrom Engineering Evovac) in dark conditions on

top as a conductive layer for electron-beam lithography. The resist was patterned (JEOL JBX-6300FS) from an original design file. After patterning, the conductive layer was removed chemically in gold etch, potassium iodide, and iodine. The resist was developed with a 1:2 mixture of isopropanol and methyl isobutyl ketone for 1 min followed by a cleaning with isopropanol alone. 3 nm titanium followed by 60 nm gold were evaporated onto the sample by electron-beam evaporation (Denton Enerjet Evaporator). Undeveloped PMMA was lifted off in acetone at 20 °C overnight.

A layer-by-layer method was used to create a 6 ± 1 nm polyelectrolyte spacer on top of the lithographically created nanoparticles to avoid quenching and to provide a suitable surface for adsorption and desorption of Cy5.5 as described previously.[85] Three layers were spin coated at 300 µL, 15 s, 4000 rpm: a poly(diallyldimethylammonium chloride) layer (PDADMAC, SigmaAldrich, average molecular weight 200,000 − 350,000, diluted to 2 mM); a poly(sodium 4-styrene) layer (PSS, Sigma-Aldrich, average molecular weight 70,000, diluted to 2 mM); then a final layer of PDADMAC.

3.2.2 Polarimetric Microscope

A polarimetric microscope system capable of polarization-resolved excitation and detection of single dye molecules (Figure 3.1a) was built onto an Olympus IX71 inverted epifluorescence microscope as described in Chapter 2.

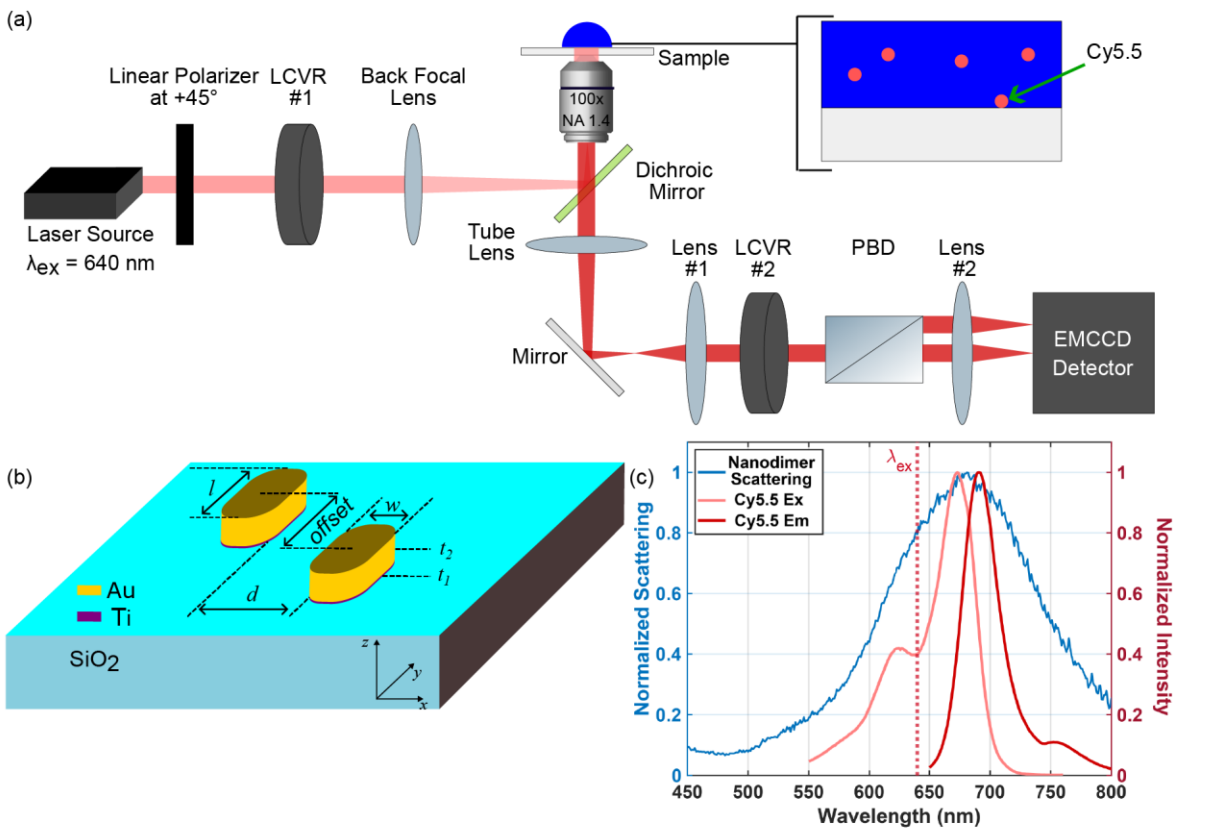

Figure 3.1: Single-molecule polarization-resolved microscope setup and nanodimer antenna design.
(a) Single-molecule circular polarization microscope schematic. LCVR: liquid crystal variable retarder, PBD: polarizing beam displacer, EMCCD: electron-multiplying charge-coupled device. (b) Schematic of chiral nanoparticle dimer on glass. l = 100 nm, w = 60 nm, d = 30 nm, Ti thickness: t_1 = 3 nm, Au thickness: t_2 = 60 nm, variable offset. (c) Dark-field scattering spectrum of a single nanodimer with −50 nm offset (blue), Cy5.5 excitation and emission spectra (light red and dark red, respectively). Dotted line indicates excitation wavelength (λ_{ex} = 640 nm).

3.2.3 Dark-Field Scattering Spectroscopy

The nanodimers were characterized by dark-field scattering spectroscopy in the microscope. Each array was excited with a broadband halogen lamp through a water-immersion dark-field condenser, and scattered light was collected through a dark-field oil-immersion objective (NA 0.6). The image of each nanodimer was aligned to the entrance slit of an imaging spectrograph (Acton 2300, Princeton Instruments), and spectral data were collected on an EMCCD detector (1 s integration time, electron-multiplying gain 200; Andor iXon). Background spectra

collected from nearby positions with no nanodimer on the spectrograph entrance slit were subtracted from measured spectra, and all data were divided by the broadband spectrum of the halogen light source with an ND 2.0 filter to correct for the system spectral efficiency.

3.2.4 Cy5.5 Characterization

Cy5.5 maleimide dye (Cytiva Life Sciences, PA15631) was purchased from the manufacturer and diluted in DMSO for storage. The stock was diluted in distilled de-ionized (DDI) water to the correct concentration on the day of each experiment. The dye fluorescence excitation (at 770-nm emission) and emission (upon 640-nm excitation) were characterized at 0.2 μM (Horiba Quanta Master fluorescence spectrophotometer).

3.2.5 Super-Resolution Single-Molecule Microscopy

The polyelectrolyte-coated nanodimer sample was covered with 100 μL DDI water in a clean rubber O-ring, and the nanodimer photoluminescence polarization was measured. The water was then replaced by 100 μL of 1 nM Cy5.5, and Points Accumulation for Imaging Nanoscale Topography (PAINT) Microscopy was used to detect the fluorescence from one Cy5.5 molecule at a time as the molecules adsorbed onto the surface as described previously.[60,80] When adsorbing to the coverslip, previous work has found that the Cy5.5 molecules have a well-defined transition dipole orientation in the imaging plane during the course of fluorescence imaging for integration times up to 340 ms. In particular, Zuo et al. measured the linear polarization of the fluorescence from single Cy5.5 molecules adsorbed to substrates like the ones used in this work for integration times between 20 – 340 ms and observed no significant change in the variance of the measured Cy5.5 polarization angles for integration times between 20 – 140 ms.[74] Thus, I expect that each adsorbed molecule is stationary during the fluorescence dissymmetry measurements in this work,

which use a 40-ms integration time. The 640-nm excitation intensity was 2.15 ± 0.04 μW/μm^2 for the +50 nm, −50 nm, and no-offset nanodimers, and excitation polarizations are noted in the text. Images were recorded continuously on the EMCCD at 40 ms/frame such that only adsorbed molecules were detected.

3.2.6 Single-Molecule Localization and Image Analysis

The images of the two channels on the camera were registered using Control Points Registration (MATLAB Image Processing Toolbox) in which the off-center channel image was chosen to be the moving image and the center channel image was chosen to be the fixed image. Within a median projection of all the frames in each movie, a control point on each of 22 – 25 nanodimers was selected for each channel and these coordinates were fine-tuned by a phase correlation. A projective transformation was applied to every frame in the movie using the transformation matrix made from the control point coordinates. To maximize the signal-to-noise ratio for single-molecule localization, the transformed off-center channel frames and the unchanged center channel frames were summed. The SMALL-LABS algorithm[134] was used to localize single Cy5.5 molecules in each frame of these summed movies: for each localization, the local background for each molecule including any gold nanodimer photoluminescence was subtracted based on the images before and after Cy5.5 adsorption. In each imaging frame, the intensity of each molecule was calculated as the summed counts from this background-subtracted single-molecule image. After detecting and localizing Cy5.5 molecules in the summed image, the polarization information was accessed by comparing the intensities in the separate emission channels.

The single-molecule fluorescence dissymmetry factor ($g_{\mathrm{fl,sm}}$) is:

$$g_{fl,sm} = 2\frac{I_{LCP} - I_{RCP}}{(I_{LCP} + I_{RCP})} \tag{3.1}$$

where I_{LCP} is the intensity of fluorescence in the LCP channel and I_{RCP} is the intensity of fluorescence in the RCP channel. These channels are characterized as described in Chapter 2.

The distributions of apparent localizations of Cy5.5 molecules near 22 – 25 nanodimers in each condition were analyzed. The number of molecules per nm^2 was calculated using Voronoi cells at each point (*scatplot* function from MATLAB File Exchange). In this plot, each point represents a molecule, and its color indicates the density of molecules near that point. Each molecule localized for ≥ 2 successive frames is plotted as a single point at the track center of mass. Additionally, the localization probability was calculated as the number of molecules falling into each 30 nm × 30 nm 2D bin in a histogram. Within these distributions, regions of high localization density were identified based on a threshold for high-density points that is two standard deviations greater than the maximum density from a simulation of the same number of completely spatially random points over the same area (Figure 3.2).

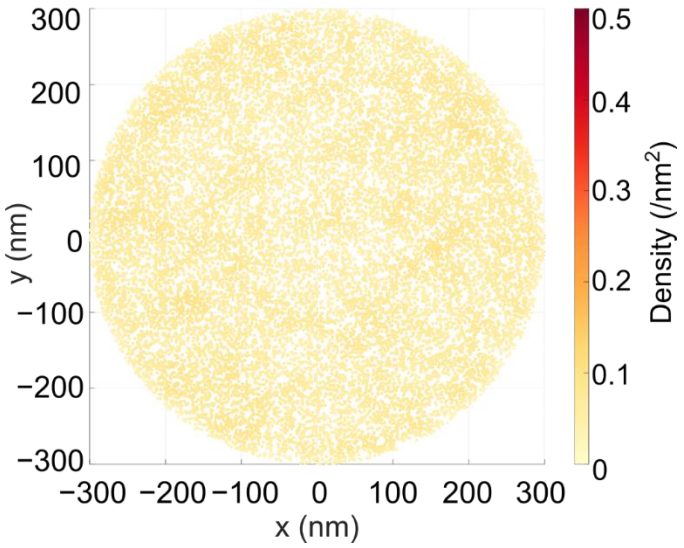

Figure 3.2: Density of Cy5.5 away from a nanodimer.
Density of Cy5.5 localizations in a region away (greater than 600 nm) from any nanodimers. RCP excitation. Each point is the apparent position of one randomly adsorbing Cy5.5 molecule in the summed movie.

Table 3.1: Detection frequencies of Cy5.5 near nanodimers.
Frequency of detecting single molecules in the region near the nanodimer (< 475 nm from the nanodimer center) and in a region far from any nanodimers (900 nm^2 is the size of the pixels in Figure 3.10): in this experiment where the probability of molecules adsorbing is constant, there is a bias toward detecting molecules in the enhanced field region near the nanodimers.

	Number of localizations per 900 nm^2 near the nanodimers	**Number of localizations per 900 nm^2 away from the nanodimers**
+50 nm nanodimer	3.2	1.6
0 nm nanodimer	6.3	1.8
−50 nm nanodimer	8.1	1.6

The 2D histograms of $g_{fl,sm}$ (Figure 3.10) depict the average dissymmetry factor of all molecules falling in each 30 nm × 30 nm bin. This 30-nm bin length is half the mode of the distribution of confidence intervals for our single-molecule localizations. The color of each bin corresponds to $g_{fl,sm}$ and the transparency of each bin reports on the uncertainty of this average: the transparency of any bin with a number of localizations below the average is 10%, and the

transparency for the rest of the bins varies linearly according to the standard deviation of each bin from 100% (lowest standard deviation) to 10% (highest standard deviation).

3.2.7 Electromagnetic Simulations of Scattering and Near-Field Optical Chirality

Full-field electromagnetic simulations of the nanodimers were performed with a finite-difference time-domain (FDTD) software package (Ansys Lumerical FDTD). The nanodimer on SiO_2 was modeled as a pair of rectangular prisms with rounded corners and tops (Figure 3.1b). The frequency-dependent complex permittivities of Ti and Au were obtained by an analytical fit to experimental data.[143,144] The SiO_2 base was explicitly included (n = 1.5, k = 0), and the nanodimers were immersed in water (n = 1.333, k = 0). The total simulation volume was 8 μm^3; near the nanodimer, the fixed mesh had 8 nm^3 voxels and an adaptive mesh was used elsewhere. Perfectly matched layer boundary conditions were used.

3.2.8 Near-field Optical Chirality and Local Dissymmetry Factor

The near-field optical chirality, C, was determined from the electric and magnetic field results calculated with the FDTD software. To simulate the laser direction, the nanodimers were excited from below by a broadband plane wave source located at the bottom of the simulation volume. The median optical chirality was calculated in the gap region of the nanodimers (an 18 nm × 48 nm × 24 nm box centered at the nanodimer centroid; Figure 3.3a) for different offsets between the two particles. A 27 nm^3 grid size was used in these simulations for faster simulation times.

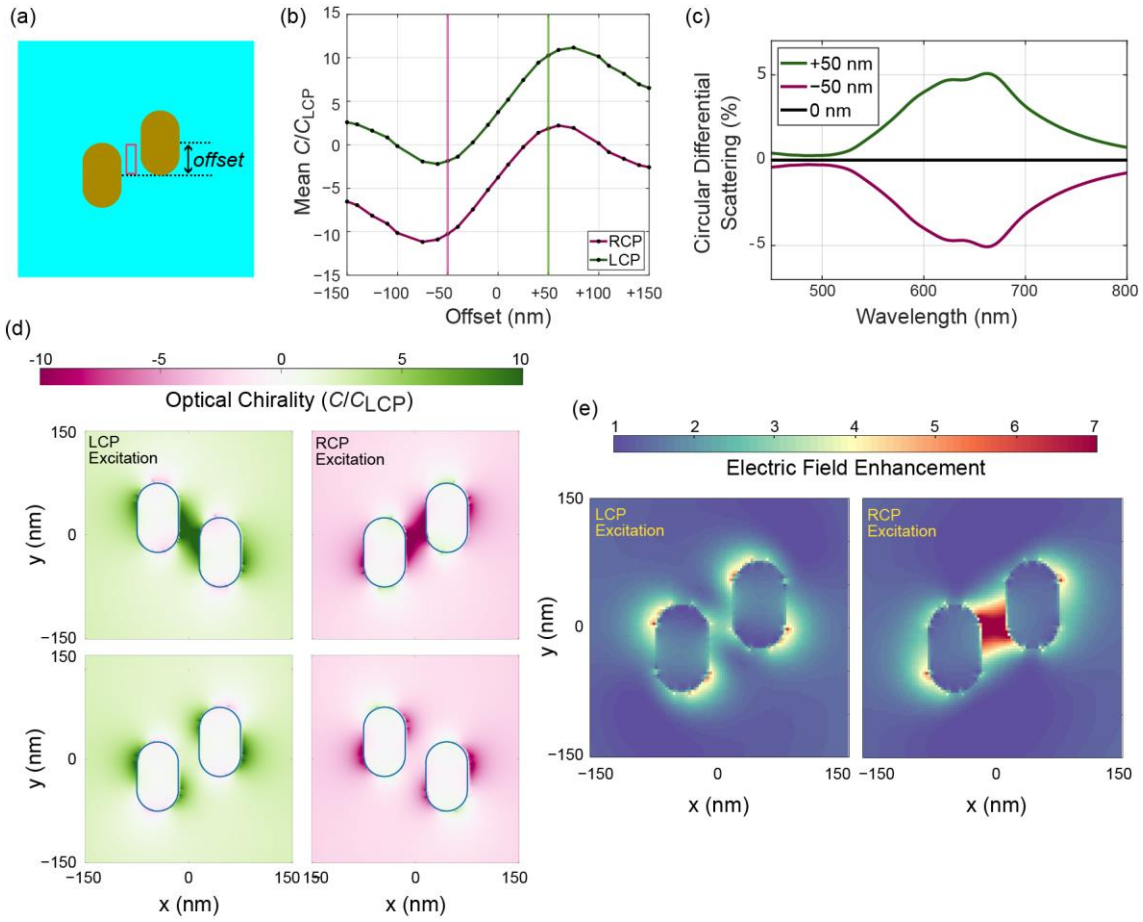

Figure 3.3: Finite-difference time-domain electromagnetic simulations of optical chirality near a nanodimer.
(a) Schematic of the −50 nm nanodimer from above. (b) Calculated normalized optical chirality averaged over an 18 nm × 48 nm × 24 nm box centered at the nanodimer center (pink box in 'a') as a function of offset. (c) Calculated circular differential scattering in the far field. (d) Calculated optical chirality upon excitation by LCP light (left) or RCP light (right) in the near field of the −50 nm nanodimer or +50 nm nanodimer. The simulations are averaged over four 300 nm × 300 nm planes going from 6 nm above the coverslip to 36 nm above the coverslip. (e) Calculated electric field magnitude enhancement upon excitation by LCP light (left) or RCP light (right) in the near field of the −50 nm nanodimer.

To calculate the far-field scattering spectra, the nanodimer was excited from above with a superposition of two broadband plane wave sources with propagation direction, *z*, normal to the substrate. These sources were linearly polarized along the *x* and *y* axes, respectively. A ±90° phase delay was added to the *y*-polarized source to create a left or right circularly polarized source. The scattered power was monitored in a plane below the nanodimers (in the glass substrate) and

projected to the far field to match the objective lens in our scattering spectrum experiments. The scattering spectra were measured for LCP and RCP excitation, and the difference between the two spectra is the circular differential scattering (CDS) spectrum.

The simulation geometry in Figure 3.3a was also used to calculate maps of the electric and magnetic fields at 2D *xy* plane monitors, and the average optical chirality, *C* was calculated from the electrical and magnetic fields at four *xy* planes from z = 6 nm above the coverslip to z = 36 nm above the coverslip, a depth range that corresponds to the experimentally accessible volume for the dyes, and then averaged to produce 2D maps. The maps were calculated at the experimental laser excitation wavelength of 640 nm.

3.2.9 Standard Deviational Ellipse Calculation

I determined the size and shape of the high optical chirality regions in the optical chirality maps under different excitation polarizations (Figure 3.4a). I used a threshold of two standard deviations above the mean optical chirality, *C*, or two standard deviations below *C* for LCP and RCP excitation, respectively. These pixel positions are converted from the simulations to *xy* coordinates and calculated the standard deviational ellipse by finding the eigenvalues and eigenvectors of the covariance matrix for this subset with a 90 % confidence interval for the χ^2 distribution.[S1] This calculation gives the length, width, and angle of the high optical chirality field region near the nanodimer.

I determined the size and shape of the region of high induced dissymmetry in the experimental fluorescence localization maps by calculating the standard deviational ellipse on the subset of high-density, high-dissymmetry points (Figure 3.4b). High density was defined as two standard deviations greater than the maximum density in a simulation of the same number of completely spatially random points in the same area. High dissymmetry was defined as values

greater than the median of the distribution of the single-molecule dissymmetry values (Figure 3.5a).

3.3 Results and Discussion

The dark-field scattering spectrum of the fabricated –50 nm nanodimers peaks at 680 nm (Figure 3.1c). This peak matches well with the scattering maximum predicted by finite-difference time-domain (FDTD) simulations, and the peak position and scattering intensity are insensitive to the nanodimer offset over the range investigated in this work (Figure 3.6).

Both absorption and emission enhancements will contribute to the fluorescence intensity enhancement because the nanodimer size is tuned to produce a broad plasmon resonance with maximal spectral overlap with the Cy5.5 excitation and emission spectra (Figure 3.1c). With RCP excitation, I observe a 1.4-fold increase in the summed fluorescence emission intensity from both channels for Cy5.5 molecules that are within 300 nm of the –50 nm nanodimer center relative to molecules > 600 nm from any nanodimer (Figure 3.7). On the other hand, the induced fluorescence dissymmetry that we record is due to emission coupling alone as the dyes are achiral. Earlier work has established that single-molecule mislocalization and mispolarization result from emission coupling.[74,136,142]

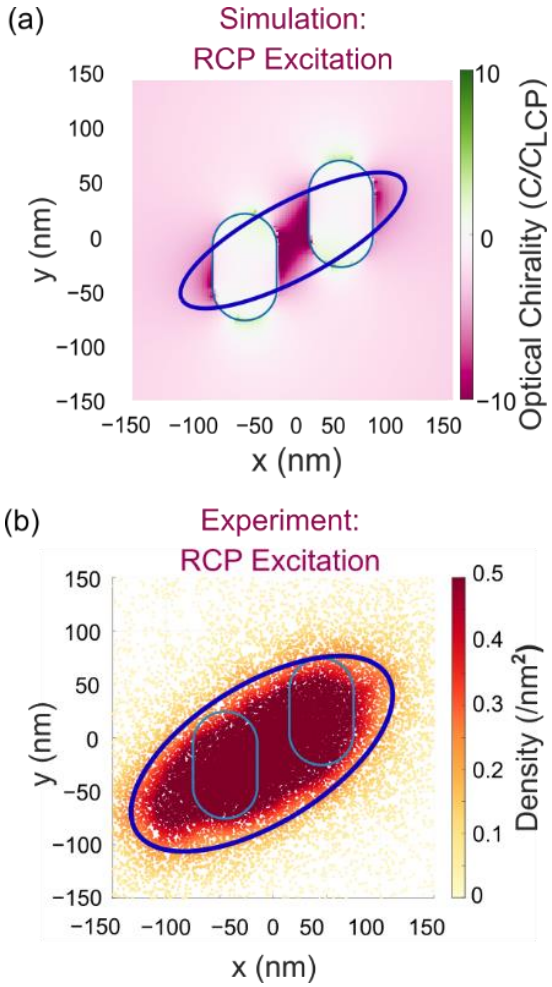

Figure 3.4: Standard deviational ellipse results for the −50 nm nanodimer.
(a) Calculated optical chirality in the near field of the −50 nm nanodimer excited. Blue oval: standard deviational ellipse calculated from pixels with C values greater than two standard deviations below the mean optical chirality. (b) Density of Cy5.5 localizations about the −50 nm nanodimers under RCP excitation with high apparent dissymmetry ($g_{\mathrm{fl,sm}} < -0.464$). Blue oval: ellipse calculated from points with a density two standard deviations above the mean density of complete spatial randomness (Figure 3.2). The experimental localization density map and the simulated optical chirality calculation correspond spatially: the ellipse major axis radius is 138 nm in the localization density experiments and 117 nm in the simulations; the minor axis is 65 nm in the experiments and 35 nm in the simulation data; and the angle of the major axis relative to the nanodimer x-axis (defined in Figure 3.1) is 32° for the experimental data and 27° for simulated data. The experiments and calculations agree qualitatively, and the discrepancy of ~30 nm between the ellipse axis lengths falls within the typical 30 – 50 nm confidence intervals for our localizations.

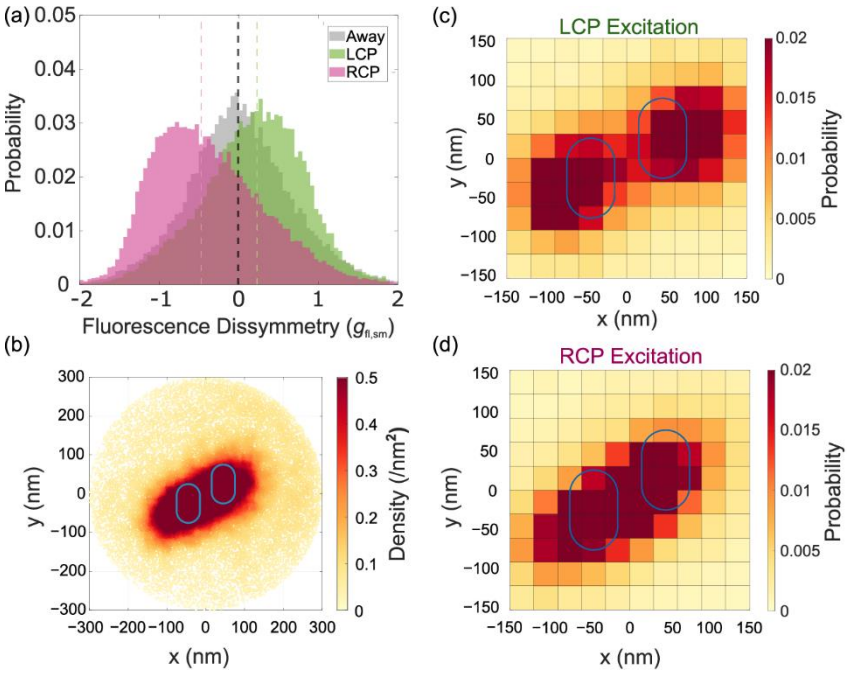

Figure 3.5: Single-molecule microscopy fluorescence dissymmetry and localization results for Cy5.5 molecules near the −50 nm nanodimers at emission wavelengths greater than 655 nm.

(a) Fluorescence dissymmetry, $g_{fl,sm}$, distributions from 30,000 localizations near 25 nanodimers under LCP or RCP excitation as well as from 30,000 localizations farther than 600 nm away from any nanodimers. Dotted lines indicate the median $g_{fl,sm}$ for each distribution. (b) Density of all Cy5.5 localizations within a 300 nm radius of the nanodimer centroid for RCP excitation. Each point is the apparent position of one randomly adsorbing Cy5.5 molecule in the summed movie. The figure includes molecules with positive and negative dissymmetry. (c) – (d) Two-dimensional histograms of localization probability for molecules with (c) dissymmetry $g_{fl,sm} > +0.241$ for excitation with LCP light, and (d) dissymmetry $g_{fl,sm} < -0.464$ for excitation with RCP light.

(a)

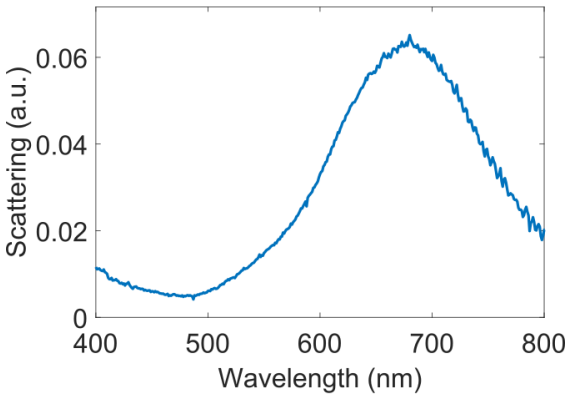

(b)

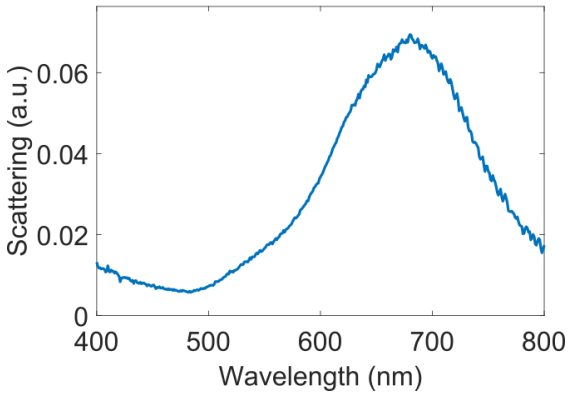

Figure 3.6: Dark-field scattering spectra of nanodimers.
Measured dark-field scattering spectra from (a) +50 nm nanodimers and (b) –50 nm nanodimers. Each spectrum is the average of the scattering signal from five nanodimers.

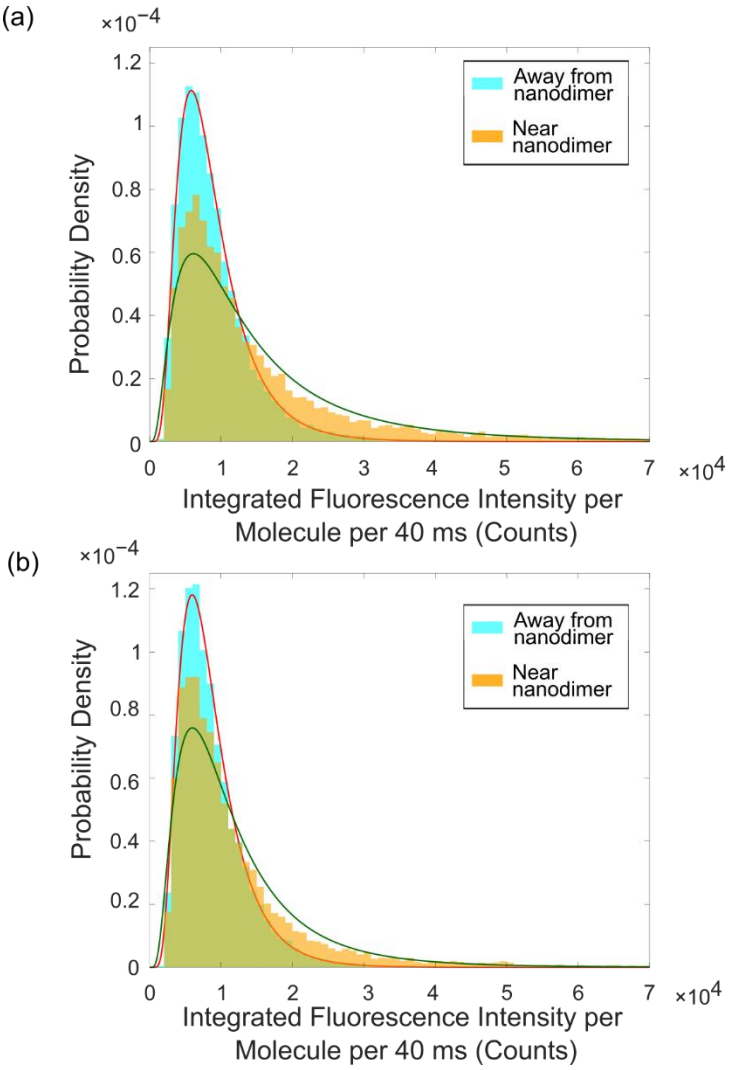

Figure 3.7: Single Cy5.5 molecule intensity distributions.
Distribution of fluorescence intensities from single Cy5.5 molecules near and away from a −50 nm nanodimer excited with (a) RCP light and (b) LCP light. The single-molecule intensities are calculated from the integral of the Gaussian fit for the image of molecules in the summed two-channel movie. Solid lines: fits to a log-normal distribution. Cy5.5 molecules are "near" when within 300 nm of a nanodimer center (orange) and "away" when over 600 nm from the nearest nanodimer center (cyan). (a) For RCP excitation, the fluorescence enhancement factor of 1.4 is calculated from the ratio of the median brightness of Cy5.5 molecules near a nanodimer (10500 counts/40 ms) to the median brightness of Cy5.5 molecules away from the nanodimers (7660 counts/40 ms). (b) For LCP excitation, the fluorescence enhancement factor of 1.2 is calculated from the ratio of the median brightness of Cy5.5 molecules near a nanodimer (8950 counts/40 ms) to the median brightness of Cy5.5 molecules away from the nanodimers (7520 counts/40 ms).

We quantify the chiral near-field interaction of these nanodimers with nearby fluorescent molecules based on the time-averaged optical chirality, C:[17]

$$C = -\frac{\omega}{2c^2} Im(\mathbf{E}^* \cdot \mathbf{B}) \tag{3.2}$$

where **E** and **B** are the complex electric and magnetic field vectors, respectively, ω is the angular frequency of the radiation, and c is the speed of light. We normalize C by the optical chirality of an LCP propagating wave, C_{LCP}:[17,145]

$$C_{LCP} = +\frac{\varepsilon_0 \omega}{2c} |\mathbf{E}|^2 \tag{3.3}$$

The offset between the monomers in a plasmonic dimer has a strong effect on C.[140,146] To determine which offsets are suitable for the study of optical chirality in our nanodimer system, we calculated the average optical chirality in the gap region (pink box in Figure 3.3a) as a function of the offset for each excitation polarization (Figure 3.3b). Greater than ten-fold chirality enhancement occurs for offsets between 50 and 100 nm with LCP excitation and between −50 and −100 nm with RCP excitation. Previous work has shown that an offset equal to half the monomer length results in high apparent fluorescence dissymmetry from achiral dyes, so I investigated the coupling of fluorescent molecules to the −50 nm and +50 nm nanodimers.[138,140] These two nanodimers (with ±50 nm offsets), as well as the achiral control ("no-offset") are the focus of the rest of this work.

The simulated far-field circular differential scattering (CDS) shows only a single-sign response in the visible wavelength region (all-negative for the −50 nm nanodimer and all-positive for the +50 nm nanodimer, Figure 3.3c). At all wavelengths, as expected based on the near-field response in the gap (Figure 3.3b), the +50 nm nanodimer scatters LCP light more strongly and the −50 nm nanodimer scatters RCP light more strongly. Additionally, I detect no CDS signal for the no-offset nanodimers, consistent with the fact that this nanodimer is achiral.

To predict the heterogeneous induced dissymmetry in the near field, I mapped the optical chirality near the nanodimer (Figure 3.3d). I averaged the results from planes from 6 – 36 nm above the coverslip because experimentally, a 6-nm polymer spacer layer separates dye molecules from the plasmonic nanodimer on the glass slide in our experiments, so molecules access the region from 6 – 36 nm. As expected, the right-handed −50 nm nanodimer interacts more strongly with RCP light and the +50 nm nanodimer interacts more strongly with LCP light; the optical chirality patterns for these situations are mirror images and both predict average optical chirality enhancement of ~10 in the gap. Interestingly, the near-field maps for LCP light interacting with the right-handed −50 nm nanodimer also show areas of optical chirality enhancement, and the mirror-image response is predicted for the +50 nm nanodimer under RCP light excitation (Figure 3.3d). In these cases, however, the regions of enhanced optical chirality are close to each monomer within the dimer rather than located in the gap and the enhancement is smaller: the average optical chirality enhancement is ~5-fold. I expected that the regions of high optical chirality of the incident light would indicate where the directional coupling of the fluorescence emission with the antenna is the strongest.

Based on previous work, I predicted that an average negative fluorescence dissymmetry will be induced near the −50 nm nanodimer and that an average positive fluorescence dissymmetry will be induced near the +50 nm nanodimer.[139,140] In addition, I controlled the incident polarization to change the pattern of regions with high electric field magnitudes (Figure 3.3e), which also happen to be regions of high optical chirality. In this way, I biased the detection (Figure 3.2b) to molecules that adsorb to the substrate in different regions based on the excitation polarization. I recorded the fluorescence from single Cy5.5 molecules adsorbing on the sample surface near the −50 nm nanodimer (Figure 3.1a inset), and for each localized molecule, I calculated the single-

molecule fluorescence dissymmetry factor, $g_{fl,sm}$ (equation (3.1), Methods). The distribution of $g_{fl,sm}$ for 30,000 single molecules detected within 300 nm of the center of a −50 nm nanodimer has a median $g_{fl,sm} = -0.464$ when the −50 nm nanodimers are excited with RCP light and a median $g_{fl,sm} = +0.241$ when the −50 nm nanodimers are excited with LCP light (Figure 3.5a). The two-fold larger absolute value of the median fluorescence dissymmetry factor of $g_{fl,sm} = -0.464$ when the −50 nm nanodimers are excited with RCP light is consistent with the stronger interaction of the −50 nm nanodimer with RCP light (Figure 3.3) is consistent with stronger coupling of the Cy5.5 fluorescence when the molecule adsorbs in the gap region versus when the molecule adsorbs elsewhere on the substrate.

These measured median fluorescence dissymmetry factors for Cy5.5 dye molecules about the nanodimers are similar to the induced fluorescence dissymmetry factors of achiral dyes coupled to nanodimers previously reported in bulk experiments.[139,140] The experiment also estimates a lower limit for the detectable median fluorescence dissymmetry factors from dye molecules adsorbing to the substrate > 600 nm from the center of any nanostructure. In the absence of coupling to the nanodimers, the noise in the measurement of $g_{fl,sm}$ is on the order of 10^{-3}. The median fluorescence dissymmetry factors of −0.464 and +0.241 measured for molecules near the nanodimers are therefore increased ~100-fold from the median away from nanodimers (Figure 3.5a).

The broad distribution of the measured fluorescence dissymmetry values away from nanodimers in Figure 3.5a reflects the measurement error: the median dissymmetry is near zero, but the distribution tails extend out to the theoretical maximum dissymmetry of ±2. In the case of Cy5.5 away from nanodimers, this broad distribution arises from distortions introduced by collection optics: mirrors in the emission pathway and the high-NA objective accepting off-axis

fluorescence emission components (Figure 3.1a, Chapter 2 Figures 2.5 – 2.6).[133] Despite this broadening, the measured fluorescence dissymmetry values near the nanodimers are significantly shifted from the median fluorescence dissymmetry away from nanodimers, and the fluorescence dissymmetry distribution near the nanodimers is skewed whereas the fluorescence dissymmetry distribution is symmetric for Cy5.5 away from nanodimers. Therefore, despite the collection optic errors on the measured fluorescence dissymmetry values, I am still able to induce a measurable shift in the median fluorescence dissymmetry between Cy5.5 near the nanodimer versus that away from the nanodimer as a result of the heterogeneous near-field environment near the nanodimers.

In addition to providing average fluorescence dissymmetry values, single-molecule super-resolution microscopy can access the nanometer-scale spatial distribution of the apparent single-molecule localizations near a nanoparticle. Because the dye molecules are stochastically adsorbing from the solution to the substrate, their actual positions should be random, and indeed far from the nanodimers, the localization map is homogeneous (Figure 3.2a). On the other hand, the interaction of a dye molecule with a plasmonic nanoantenna changes its apparent single-molecule position,[80,147,148] and when the −50 nm nanodimers are excited with RCP light, I find that more detected molecules appear along a ~30° angle line relative to the nanodimer *x* axis for localizations detected in the summed movie from both channels (Figure 3.4). This skew in the localization density (Figure 3.5b) is not present for dye molecules near the achiral control (no-offset nanodimer), and a similar skew in the localization pattern appears along the opposite direction for the case of the +50 nm nanodimer excited with LCP light (Figures 3.8 – 3.9). I attribute this skew to two factors: mainly, the emission of a dye molecule near a resonant plasmonic nanoantenna will interfere with the plasmon mode to produce an emission pattern that reflects the emission from the

coupled system,[137] and also the absorbance and emission intensity of dye molecules along this nanodimer axis will be enhanced, leading to a bias toward detecting those molecules.

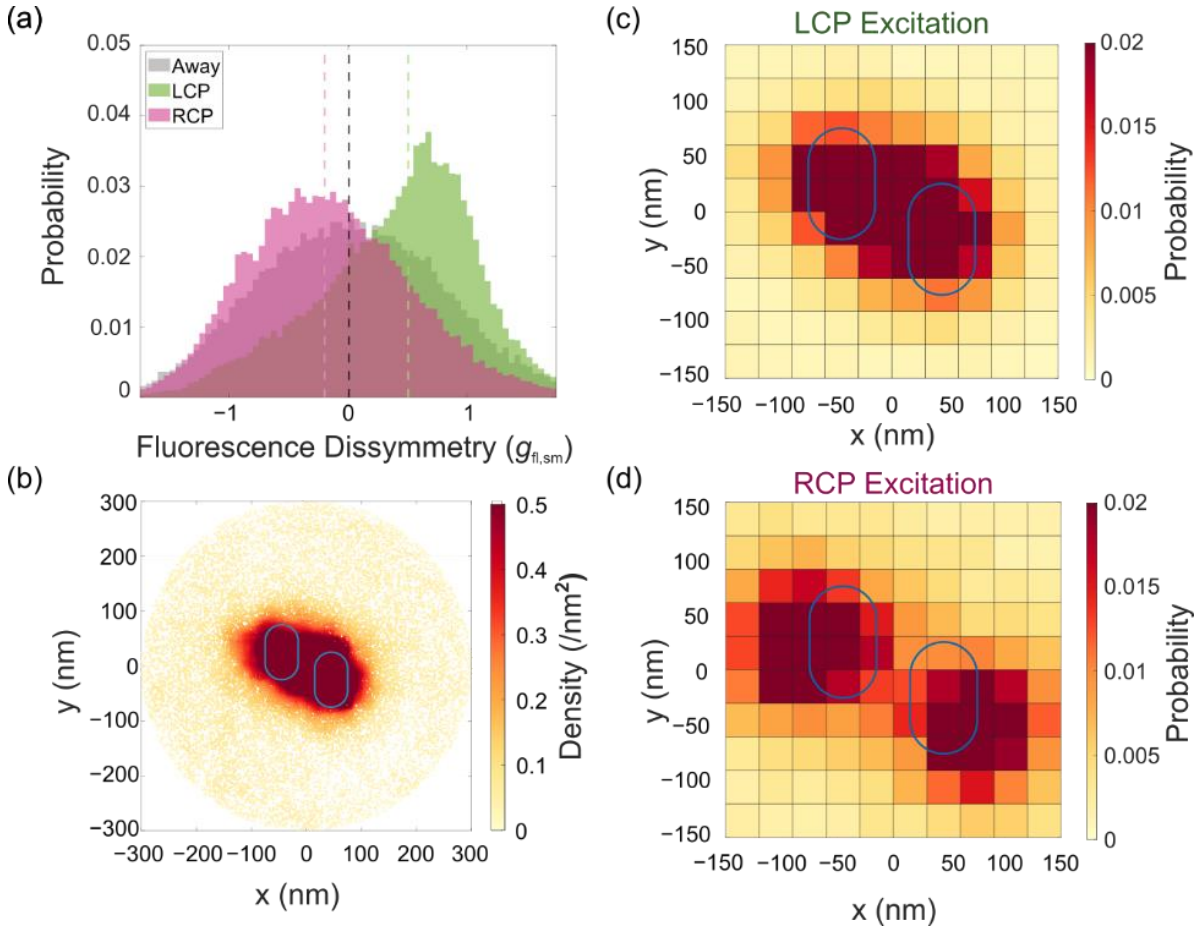

Figure 3.8: Single-molecule microscopy fluorescence dissymmetry at wavelengths greater than 655 nm and localization results for Cy5.5 molecules near the +50 nm nanodimers.
(a) Fluorescence dissymmetry, $g_{fl,sm}$ distributions from 30,000 localizations near 25 nanodimers under LCP or RCP excitation as well as from 30,000 localizations away from any nanodimers. Dotted lines indicate the median $g_{fl,sm}$ for each distribution. (b) Density of all Cy5.5 localizations within a 300 nm radius of the nanodimer centroid for LCP excitation. Each point is the apparent position of one randomly adsorbing Cy5.5 molecule in the summed movie. The figure includes molecules with positive and negative dissymmetry. (c) – (d) Two-dimensional histograms of localization probability for molecules with (c) dissymmetry $g_{fl,sm} > +0.507$ for excitation with LCP light, and (d) dissymmetry $g_{fl,sm} < -0.198$ for excitation with RCP light.

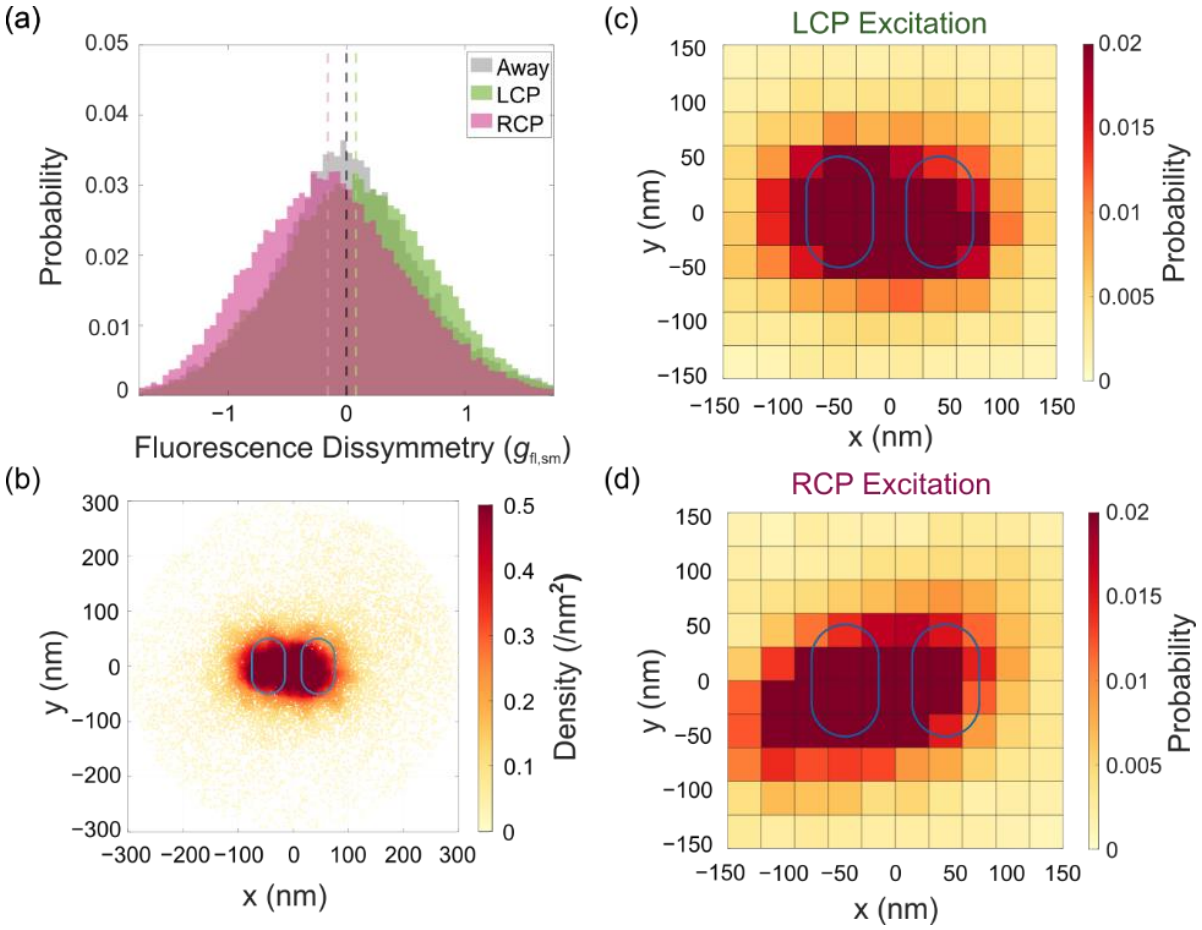

Figure 3.9: Single-molecule microscopy fluorescence dissymmetry at wavelengths greater than 655 nm and localization results for Cy5.5 molecules near the no-offset nanodimers. (a) Fluorescence dissymmetry, $g_{fl,sm}$ distributions from 30,000 localizations near 22 nanodimers under LCP or RCP excitation as well as from 30,000 localizations away from any nanodimers. Dotted lines indicate the median $g_{fl,sm}$ for each distribution. (b) Density of all Cy5.5 localizations within a 300 nm radius of the nanodimer centroid for LCP excitation. Each point is the apparent position of one randomly adsorbing Cy5.5 molecule in the summed movie. The figure includes molecules with positive and negative dissymmetry. (c) – (d) Two-dimensional histograms of localization probability for molecules with (c) dissymmetry $g_{fl,sm} > +0.081$ for excitation with LCP light, and (d) dissymmetry $g_{fl,sm} < -0.156$ for excitation with RCP light.

Each detected molecule is characterized by its apparent position (Figure 3.5b) and its fluorescence dissymmetry factor (equation (3.1)). We reconstructed the 2D probability histogram for only the molecules with dissymmetry factors greater than the median from Figure 3.5a (Figures 3.5c – d). Similar to the super-resolution map in Figure 3.5b, the super-resolution map for the molecules with the most RCP emission ($g_{fl,sm} < -0.464$) is skewed along a line connecting the

centers of each individual particle in the nanodimer system (Figure 3.5d). On the other hand, the super-resolution map for the molecules with the most LCP emission ($g_{fl,sm}$ >+ 0.241) shows that the highest probability of apparent localizations is outside the nanodimer gap. The apparent localization maps in Figure 3.5c – d strongly resemble the optical chirality patterns predicted in Figure 3.3d, indicating that the coupled emission pattern is strongly affected by the local optical chirality. Highly modified polarization indicates a strong interaction between a molecular dipole and a plasmon mode.[73,74,86] The results here show that nanoparticles induce fluorescence dissymmetry and modify emission polarization angles. When the emission from a fluorophore is strongly coupled to a plasmon mode, the localization pattern reflects scattering from the dye-nanoparticle system and informs on the local electromagnetic field strength and polarization.[73]

The apparent localization patterns for the induced fluorescence dissymmetry about the nanostructures are shown in 2D histograms for the +50 nm, −50 nm, and no-offset nanodimers under different excitation polarizations (Figure 3.10). For LCP excitation of the +50 nm nanodimer, a maximum dissymmetry of +0.76 occurs in the gap region (Figure 3.10a, 60 nm × 60 nm square centered at the origin). For the achiral no-offset nanodimer, the induced dissymmetry in the gap region reaches a maximum of +0.18 (Figure 3.10b). For the −50 nm nanodimer, the dissymmetry reaches a maximum dissymmetry value of +0.45 outside of the gap region; the dissymmetry in the gap region is relatively low (Figure 3.10c). Similar trends are observed for the mirror-image RCP excitation (Figure 3.10d – f). Particularly striking is the spatial patterning of the dissymmetry near the +50 nm and −50 nm nanodimers (Figure 3.10c and f). In these cases where the excitation polarization is opposite their handedness from the bulk spectrum in Figure 3.3c, I observe the lowest induced dissymmetry from any of the particles in their gap region, but a strong induced dissymmetry twice that of the no-offset nanodimer outside of the gap region.

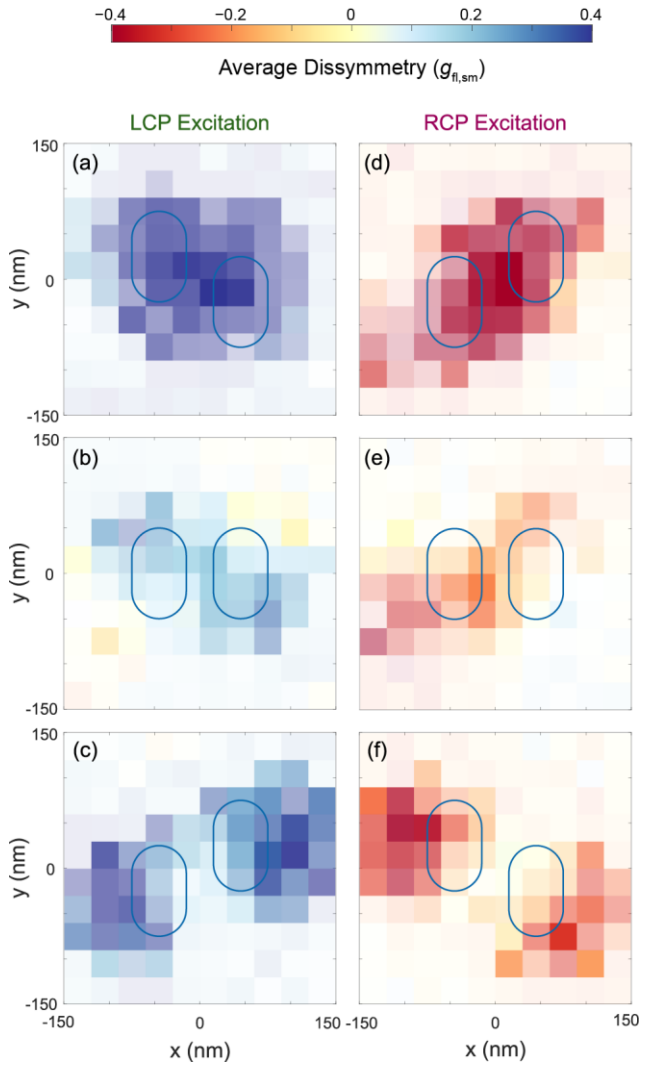

Figure 3.10: Maps of induced fluorescence dissymmetry for emission from Cy5.5 molecules at wavelengths greater than 655 nm.
(a – c) Fluorescence emission under LCP excitation near (a) a +50 nm nanodimer, (b) a no-offset nanodimer, or (c) a −50 nm nanodimer. (d – f) Fluorescence emission under RCP excitation near (d) a −50 nm nanodimer, (e) a no-offset nanodimer, and (f) a +50 nm nanodimer. The dissymmetry factor in each bin is the mean dissymmetry of all the localizations in that 30 nm × 30 nm bin (colorscale). The transparency of each bin reports on the number of localizations detected and the standard deviation (Methods).

The simulated optical chirality enhancement pattern (Figure 3.3d) correlates with the experimental induced fluorescence dissymmetry patterns (Figure 3.10), including mirror image responses for the +50 and −50 nm nanodimers, which supports our hypothesis that regions of high optical chirality indicate regions of maximal directional coupling. Additionally, the induced

dissymmetry is an order of magnitude larger for the offset nanodimer pairs relative to the achiral control nanodimer (Figure 3.9). Though the emission from an achiral molecule is linear, nanoparticles can redirect RCP and LCP light in different ways, leading to highly circularly polarized light emitted in directions normal to the excitation direction.[131,132,140] The net effect is the detection of highly circularly polarized emission.

3.4 Conclusions

I have demonstrated a new method to measure the apparent fluorescence dissymmetry from single molecules near chiral metal nanoparticles using super-resolution microscopy. I produced dissymmetry factors 100 times above both the noise floor and the dissymmetry factors of synthesized chiral fluorescent molecules.[128,149] Indeed, I detected median dissymmetry factors of up to ~|0.5| from samples as small as ~100 zeptomoles (~60,000 molecules) of achiral molecules. By localizing one molecule at a time, I mapped out where the highest induced dissymmetry occurs relative to the chiral plasmonic nanostructure, and I determined that the modified fluorescence emission pattern correlates with the near-field optical chirality controlled by the polarization of the excitation plane wave.

This single-molecule method and instrument could be applied to characterize samples for ultrasensitive CD or CPL spectroscopy. Additionally, platforms that take advantage of the high optical chirality fields near plasmonic nanostructures for all-optical separation have been proposed.[150,151] These platforms rely on large variations of the optical chirality over a small volume to generate forces on a chiral molecule. Future work will focus on the interaction between chiral nanoparticles and fluorescent molecules that possess intrinsic chirality to guide designs to detect chiral molecules via single-molecule fluorescence microscopy or to characterize platforms for

separating enantiomers in all-optical approaches. This setup also produces molecular sources of circularly polarized light, which will be useful in nanophotonic applications.

Chapter 4
Circular Dichroism of Gold Nanorods Bound to Insulin Amyloids and Measured with Polarization-resolved Fluorescence Microscopy[**]

4.1 Introduction

Amyloids are protein aggregates characterized by a cross β-sheet motif arranged into a helical shape termed fibrils. Since their discovery, amyloids have been associated with various neurodegenerative diseases such as Alzheimer's disease, Parkinson's disease, and type II diabetes.[152,153] In recent years, the amyloid structure has been recognized to be a common protein structure in nature, reported to have healthy biological functions such as in bacteria biofilms.[154] Moreover, the versatility and strength of the amyloid structure have led some researchers to

[**] *This chapter describes Zechariah Pfaffenberger's contributions to a collaborative project with Joanna Olesiak-Bańska's lab at Wroclaw University of Science and Technology in Wroclaw, Poland. My main collaborator on the project is Maciej Lipok. A co-written manuscript is in preparation.*

I performed the fluorescence microscopy experiments and analysis in Figures 4.3 and 4.6. Maciej Lipok performed the bulk circular dichroism (CD) spectroscopy and analysis, atomic force microscopy (AFM), and transmission electron microscopy (TEM) in Figures 4.2, 4.4, and 4.5. Additionally, Saaj Chattopadhyay helped acquire the super-resolution data in Figure 4.3.

propose novel materials using amyloid fibrils as scaffolds for applications as diverse as light harvesting and drug delivery.[155,156]

Because of the implication of amyloid proteins in various diseases, detecting fibrils at very low concentrations for early diagnosis is an area of intense research. In particular, the earliest stages of fibril formation, in which oligomers combine into protofibrils, are poorly understood. Since the early stages of fibril formation are thought to generate toxic species in neurodegenerative diseases, there is much interest in better characterizing these stages when the fibril concentration is still very low. Additionally, these early stages are predicted to control the chirality of the final amyloid fiber helix.[157] For example, bovine insulin typically forms a right-handed fibril structure but can be "seeded" by small amounts of human insulin fibrils to form a left-handed structure.[158]

Circular dichroism (CD) spectroscopy, which measures the difference in absorbance between left circularly polarized (LCP) and right circularly polarized (RCP) light, can be used to detect the formation of amyloid fibrils, but CD is limited to the micromolar concentration regime due to the size mismatch between the β-sheets and the wavelengths of propagating visible light.[159] Several recent studies have shown that plasmonic nanoparticles can be used to detect fibril formation and chirality at very low concentrations.[101,160,161] Noble metal nanoparticles have extinction maxima at visible wavelengths, which are easier to detect using typical instrumentation than ultraviolet wavelengths, where the signals from many biomolecules including amyloid proteins, are located. By converting the UV biomolecule signals to visible wavelengths, these plasmonic antennas allow the detection of fibrils at nanomolar concentrations and in higher background environments than ordinary CD spectroscopy.

Particularly, Luis Liz-Marzán's group showed that positively charged gold nanorods will bind to negatively charged amyloid fibrils at biological pH based on electrostatics. As the fibrils

form, achiral nanorods show an induced CD signal that grows with fibril formation (Figure 4.1a).[101]

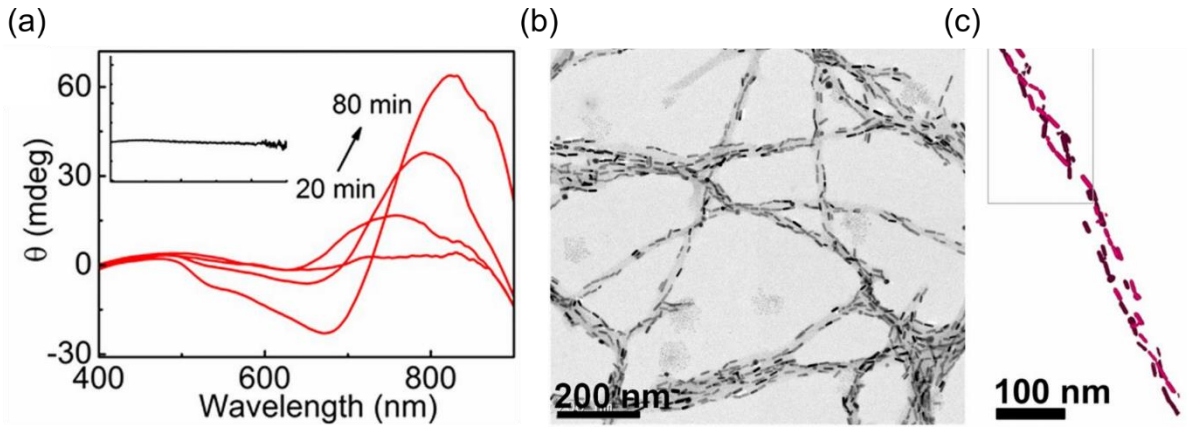

Figure 4.1: Induced CD signal from micron-scale order of nanorods bound to fibrils.
(a) CD spectra of gold nanorods mixed with α-synuclein protein undergoing fibril formation over time. Inset shows CD of nanorods in the absence of protein. (b) TEM image of nanorods bound to α-Synuclein fibrils. Dark black dots are nanorods. Light grey objects are fibrils. (c) Three-dimensional Cryo-EM reconstruction of nanorods bound to α-synuclein fibrils. Shaded pink and purple pill shapes are single nanorods. Figures are reproduced from reference 101.[101]

Liz-Marzán's group attributed the induced signal to the micron-scale helical arrangement of plasmonic nanorods. Their TEM and cryo-EM images show a micron-range chiral helix ordering of the nanorods bound to fibrils (Figure 4.1b). However, theoretical calculations of single chiral dipoles interacting with plasmonic nanoparticles have shown that a chiral dipole can also induce a circular dichroism signal in a single plasmonic nanoparticle, rather than the induced signal resulting from a micron-scale helical order. No published experimental evidence shows such an induced signal in a single nanoparticles or single-nanoparticle assemblies near an amyloid fibrils.[162]

In this chapter, I test whether micron-scale helical order, dipole coupling between a single nanoparticle and transition dipole of the amyloid, or chiral arrangement between a small number of nanorods on the 100 nm scale is the major factor in induced CD signal.[163] I tested this hypothesis

using a combination of bulk CD spectroscopy, TEM, AFM, and polarization-resolved fluorescence microscopy (PR-FM) in collaboration with Maciej Lipok from Joanna Olesiak-Bańska's lab at the University of Wroclaw. We found that 80 nm × 40 nm achiral gold nanorods can show an induced CD signal when bound to insulin amyloids without any micron-scale helical arrangement. Furthermore, my results suggest that the signal mainly arises from side-to-side aggregates of two or more nanorods, rather than from dipole-dipole coupling of the nanorod dipoles to the transition dipoles in the amyloid β-sheet[162,164] as we observe no induced CD from monomeric fibril-bound nanorods.

4.2 Methods

4.2.1 Preparation of Insulin Amyloid Fibrils

Bovine pancreas insulin (Sigma-Aldrich, ≥ 25 units/mg (HPLC), I5500) was used as received. Insulin was dissolved in double-distilled H_2O to a concentration of 10 mg/mL. The pH was adjusted to < 2 using HCl (25 mM final concentration). 1 mL of the insulin solution was incubated in an Eppendorf thermomixer for 18 hours at 70° C at 700 RPM which should result in the formation of fibrillar aggregates.[165]

4.2.2 CD Spectroscopy

Cetyltrimethylammonium bromide (CTAB)-stabilized gold nanorods in DI water (80 × 40 nm, A12-40-650-CTAB-DIH-25) were purchased from Nanopartz and used as received. Samples were prepared for bulk CD spectroscopy by diluting the stock nanorods to a final concentration of 0.025 nM in ddH_2O and mixing this dilute nanorod suspension with the prepared fibril solution (section 4.2.1) in a 3:1 ratio for a final nanorod concentration of 0.019 nM. Samples also had thioflavin T (ThT, Sigma T3516) added to a final concentration of 100 μM. NaCl was also added

to a concentration of 100 mM. The final pH was adjusted to pH = 6 with potassium hydroxide. The spectra were taken in a 500 µL, 0.2 cm path-length quartz cuvette.

4.2.3 Atomic Force Microscopy and Transmission Electron Microscopy

Samples were prepared for AFM and TEM by diluting prepared fibrils $1{:}10^6$ in ddH_2O and adjusting the pH to 6 with potassium hydroxide. 20 µL of the nanorod stock (0.05 nM) was mixed with 100 µL of the pH-adjusted fibril suspension.

4.2.4 Sample Preparation for Fluorescence Microscopy

Glass microscope coverslips (24 × 40 mm, Fisher Scientific, 12545D) were plasma cleaned with oxygen and then coated with poly-l-lysine (PLL, 0.1% w/v solution) by incubating them for 30 seconds in the PLL solution. Fibrillated insulin was diluted 1:10000 in fresh ddH_2O and incubated with ThT (final concentration 0.2 µM, Anaspec AS-88306) and potassium hydroxide to adjust the pH to 6 (solution #1). A volume of 50 µL of solution #1 was added on top of the PLL-coated coverslip on the microscope. The coverslip was imaged under 488-nm excitation to ensure fibrils were sticking to the coverslip. Then, 1 µL of gold nanorod stock was added to this volume of solution #1. After a 30-minute wait, the coverslip was washed 3 times by adding 70 µL of ddH_2O and pipetting off the majority of the volume of liquid. This process removed unbound material, but not the PLL, so that only well-bound fibrils and nanorods were imaged.

4.2.5 Polarization-resolved Fluorescence and Dark-field Microscopy

The 640- and 488-nm CW lasers (Coherent CUBE 640-40C and Coherent Sapphire 488-50, respectively) were cleaned up with laser excitation filters (Chroma Z640 and Semrock LL01-488-12.5, respectively). The excitation linear polarization was controlled with a half-wave plate (Thorlabs AHWP10M-600) and cleaned up with a linear polarizer (Thorlabs LPVISB-050-M).

The source then went through a liquid crystal variable retarder (LCVR, Thorlabs LCC1223T-A) before being focused onto the back focal plane of a 100×, 1.30 numerical aperture (NA) objective (Olympus UPlan FLN) after reflection off a dichroic mirror (Di01-R640 or Di01-R488). We controlled the polarization of the excitation light at the sample stage and corrected for the linear birefringence of the dichroic mirror by applying a voltage to tune the LCVR retardance.[113,121,166] We characterized the polarization of the laser by placing an analyzer (Thorlabs LPVISE100-A) in front of a photodiode above the sample stage (Chapter 2, Figure 2.2c). We characterized the ellipticity, ε, of the beam as the square root of the ratio of the minimum power to the maximum power, and all experiments were performed with $\varepsilon > 0.95$ for circularly polarized excitation.[113,167]

Emission was collected with the same objective, and the excitation light was rejected with the same dichroic mirror as well as an appropriate long-pass filter for each laser (Semrock EdgeBasicTM 635 nm or Semrock EdgeBasicTM 532 mm) in the objective infinity space before being focused by a tube lens. A lens relay system consisting of an f = 50 mm lens (Thorlabs AC254-050-AB-ML) and an f = 150 mm lens (Thorlabs AC254-150-AB-ML) expanded the image 3× before the image was focused onto a 512 × 512 pixel Andor iXon3 electron-multiplying charge-coupled device (EMCCD) camera (1 camera pixel = 53 nm in the imaging plane).

To obtain dark-field scattering images and spectra of the gold nanorods, the sample was excited with a broadband halogen lamp through a water-immersion dark-field condenser, and scattered light was collected through a dark-field oil-immersion objective (NA 0.6). To take a scattering spectrum, the image of each nanorod was aligned to the entrance slit of an imaging spectrograph (Acton 2300, Princeton Instruments), and spectral data was collected on an EMCCD (1 s integration time, electron-multiplying gain 200; Andor iXon). A background spectrum collected from a nearby position with no particle on the spectrograph entrance slit was subtracted

from the measured spectrum, and all data were divided by the normalized detected broadband spectrum of the halogen light source with an ND 2.0 filter to correct for the system spectral efficiency.

4.2.6 Correlated Dark-field and Fluorescence Imaging Procedure

After a fibril sample on a microscope slide was prepared as described in section 4.2.4, the sample was examined by switching back and forth between the 488-nm excitation fluorescence mode and the dark field mode on the inverted microscope. I looked for sample areas with red (650-700 nm) diffraction-limited spots (as detected in dark-field mode by a CMOS color camera, Amscope AF205), which is the characteristic color of single 80 × 40 nm gold nanorods. We then identified fibrils in the fluorescence mode by adding 1 μL of 200 μM ThT, an amyloid probe, to the sample on the coverslip. The ThT-labeled fibrils fluoresced brightly upon 488-nm excitation. We identified nanorods with a $\leq$ 200 nm distance from the center peak of the nanorod's diffraction-limited spot to the center axis of the nearest fibril. We then measured the dark-field scattering spectrum of each nanorod and identified isolated nanorods based on spectra that showed a single peak with full width at half maximum ~ 70 nm as expected for the longitudinal plasmon mode of an isolated nanorod (Figure 4.6b).

4.2.7 Transient Amyloid Binding (TAB)

Once an area of fibrils with bound nanorods was identified, 1 μL of the 2 μM ThT stock was added to 50 μL ddH_2O on top of the sample. ThT is a fluorogenic dye: the fluorescence intensity of ThT molecules bound to the fibril is much greater than that of ThT in solution.[54] In a process known as TAB, we detected isolated ThT molecules one at a time as they adsorbed and then desorbed from the fibrils based on fluorescence imaging with 488-nm laser excitation as

described above and as described previously.[54,55,68] In each region, 18000 40-ms imaging frames were obtained before most of the ThT photobleached under 488-nm excitation. The laser power densities for this TAB imaging were 13.1 ± 0.5 μW/μm^2 for 488-nm excitation.

4.2.8 Analysis of ThT Single-Molecule Localizations and Image Reconstruction

Movies were analyzed using the SMALL-LABS algorithm.[134] For each localization, we subtracted the local background, including the gold nanorod photoluminescence, by calculating the mean intensity of all frames in which no other ThT localizations were detected in that area over a range of 100 frames before and after that frame.

Super-resolution images were reconstructed by creating a scatter plot of the localization positions from SMALL-LABS where each point is a circle with an area from calculated from the 95% confidence interval and the color of each point corresponds to the density of nearest neighbors near that point. The density of molecules per nm^2 is calculated using Voronoi cells at each point (Figure 4.3a, *scatplot* function from MATLAB File Exchange).

4.2.9 Analysis of Photoluminescence Intensity

Tiff stacks of 1000 imaging frames each under LCP and RCP 640-nm excitation at 15.1 ± 0.5 μW/μm^2 were collected and the images were analyzed in Fiji. A median projection in time of the video stacks was taken. Single diffraction-limited spots corresponding to monomeric nanorods or nanorod aggregates were identified in these average images by thresholding to visualize the top 2% brightest pixels and identifying bright spots that comprised 20 pixels with brightness above the threshold.

To measure the photoluminescence intensity of the nanorods bound to fibrils stained with ThT, I took the time average of the sum of pixel intensity in a 800 nm × 800 nm (15 × 15 pixel)

square around the center of the identified spot and subtracted the background as the time average of the same area away from any nanorod or fibril.

Based on the standard definition for the dissymmetry of a chiral species, the photoluminescence dissymmetry factor, g_{PL}, was defined as:

$$g_{PL} = \frac{2(I_{LCP} - I_{RCP})}{(I_{LCP} + I_{RCP})} \tag{4.1}$$

where I_{LCP} is the background-subtracted summed pixel intensity under LCP excitation and I_{RCP} is the background subtracted summed pixel intensity under RCP excitation.

4.3 Results and Discussion

4.3.1 Bulk CD Spectroscopy of Insulin Amyloid and Gold Nanorods

With my collaborator Maciej Lipok, I tested whether gold nanorods bound to ThT-stained insulin exhibited chirality transfer in bulk. Gold nanorods in solution do not exhibit any chirality as evidenced by their zero CD spectrum (Figure 4.1a, black line). The addition of ThT-stained insulin amyloids induces a CD signal at visible wavelengths near the nanorod's longitudinal localized-surface plasmon resonance (LSPR) of 650 nm (Figure 4.1a, red line), reaching an ellipticity of −0.75 millidegrees (mdeg) at 625 nm. This slight blue shift in the peak in the absorbance spectrum from 650 nm to 630 nm upon addition of ThT-stained insulin (Figure 4.2b, red line vs. black line) may correspond to the side-to-side alignment of nanorods.[168,169]

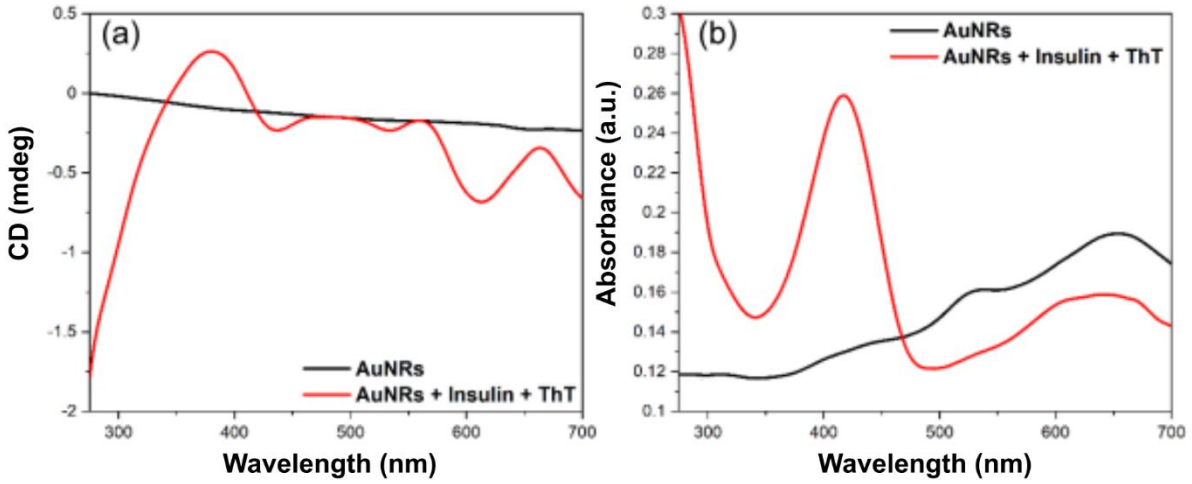

Figure 4.2: Induced CD in gold nanorods from insulin amyloid.
(a) Circular dichroism and (b) absorbance spectra of nanorods before (black) and after (red) the addition of bovine insulin amyloids and the amyloid-specific dye ThT. Insulin amyloids are diluted 2× from the original fibrillation stock. 300 µL of this solution is mixed with 100 µL of a 2× dilution solution of gold nanorods diluted. ThT concentration was 100 µM. pH = 6.

4.3.2 Microscopy of Fibril-bound Nanorods

We performed three types of imaging to confirm that the nanorods were bound to the amyloid fibrils and to test whether they exhibited long-range chiral order. I examined the fibril-bound nanorods using correlated dark-field and super-resolution fluorescence imaging (Figure 4.3) and Maciej examined the fibril-bound nanorods using AFM (Figure 4.4) and TEM (Figure 4.5).

I confirmed I could image fibrils labeled with ThT and then added gold nanorods to the microscope slide (Sections 4.2.4 - 4.2.6). Most of the nanorods are not bound to fibrils (Figure 4.3a, green arrow) because the nanorods are in excess of the fibrils. Roughly 10% of the nanorods I observed were found arranged along the axis of fibrils stained with ThT (Figure 4.3b). The pattern of the nanorods in the dark field imaging matches the bright punctate spots observed in a summed fluorescence image. The center of the bright punctate spots fall within 200 nm of the axis of the fluorescently labeled fibril.

Using TAB, I reconstructed a super-resolution image of a fibril to further confirm that we were observing nanorods bound to the fibril (Figure 4.3c). I reconstruct the image as a scatter plot where each point is the *x* and *y* peak fit position from SMALL-LABS (Section 4.2.8). Each circular data point has radius equal to our localization precision (30 nm for the 95% confidence interval on the Gaussian fit). The highest density areas (> 9 localizations/nm^2) are near two nanorods. The high probability of localizing ThT molecules in these regions is due to moderately increased fluorescence intensity, biasing detection of molecules to those areas, and to mislocalization. Molecule localizations appear closer to the center of a plasmonic nanorod when their fluorescence is coupled to the plasmonic antenna. This mislocalization occurs occurs for separation distances around 100 nm.[80,136,147] The strong shift of ThT localizations indicates the nanorods are able to interact with the fluorescent ThT and thus the nanorods are within 100 nm the fibril.

Across several samples, I found fibrils 1– 10 μm in length, with widths 50-150 nm as measured by the full-width half-maximum from the super-resolution reconstruction of the ThT molecules. We are limited by our resolution to ~30 nm, so the fibrils may be even narrower than 30 nm, and we are also biased towards finding larger fibrils because of the larger amount of binding sites for ThT. Fibrils, even those assembled in the same condition from the same monomer, vary broadly in width and length.[170]

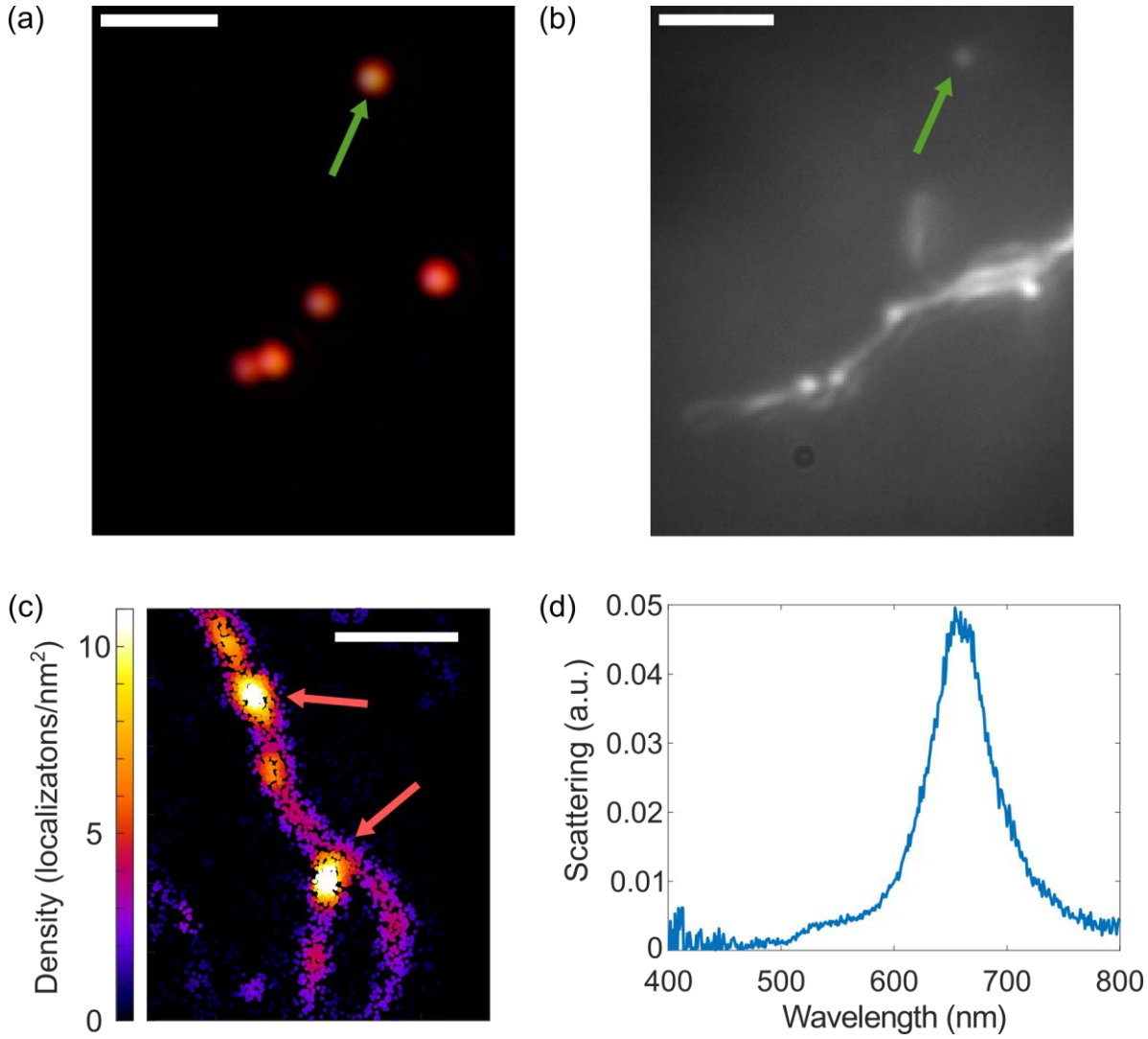

Figure 4.3: Fluorescence microscopy of nanorods with amyloid fibrils.
(a) Dark-field color microscopy image of nanorods. The green arrow indicates a nanorod not bound to a fibril based on the fluorescence image in panel b. (b) Bulk fluorescence image of the same region as in panel a showing nanorods bound to a ThT-labeled fibril. The image is an average of 1000 frames. (c) Super-resolution image reconstruction of nanorods bound to fibrils using TAB. Red arrows indicate nanorods identified by dark field imaging. Scale bars in a-c are all 1 μm. (d) Dark-field scattering spectrum of the nanorod is indicated by the top red arrow in (c).

I confirmed that the diffraction-limited spots observed in fluorescence and dark-field images were monomeric nanorods by taking their dark-field scattering spectra (Figure 4.3d). The intense single peak at 660 nm with a full width at half maximum of ~70 nm is characteristic of the

LSPR longitudinal mode of a monomeric 80 by 40 nm nanorod, while the smaller shoulder at 530 nm is characteristic of the LSPR transverse mode.

My collaborator Maciej performed AFM on a sample of fibrils and nanorods in the same conditions I used for fluorescence microscopy. Without the addition of nanorods, we observed single insulin fibrils (Figure 4.4a). Most of the fibrils observed were a few µm long, around 25 nm wide, and had an average height of around 5-6 nm. After the addition of gold nanorods to insulin amyloids prepared in the same manner as for super-resolution measurements (section 4.2.3), we observed nanorods binding to amyloid fibrils as evidenced by the 100-nm long white ovals along the fibril (Figure 4.4b).

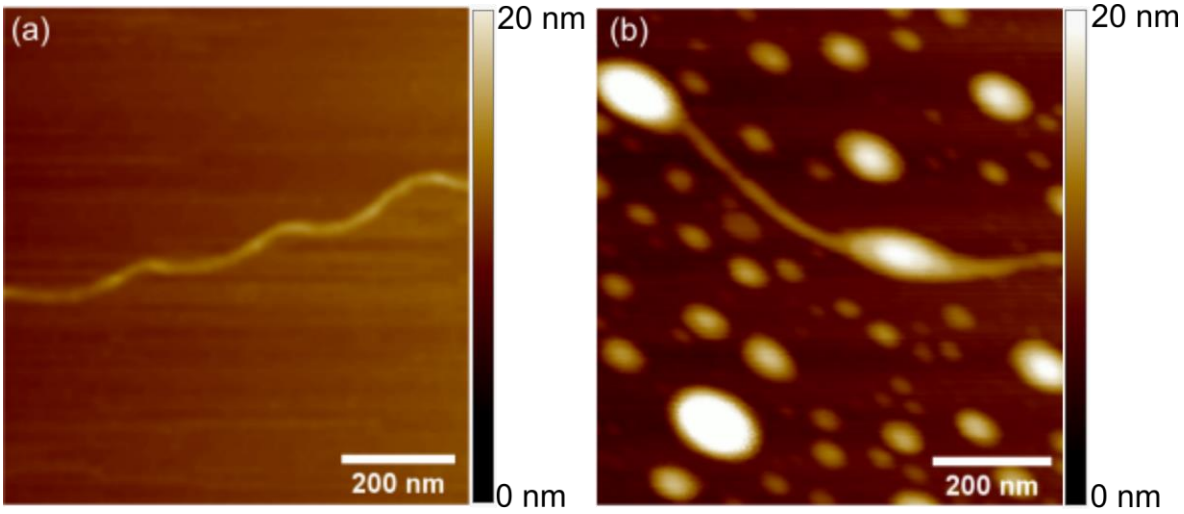

Figure 4.4: AFM of insulin amyloid and gold nanorods.
Bovine insulin amyloid fibrils (a) before and (b) after the addition of gold nanorods imaged by AFM.

Together, these imaging results prove that the sample preparation conditions result in monomeric nanorods bound to fibrils. Additionally, no long-range chiral helix structure was observed with either imaging technique.

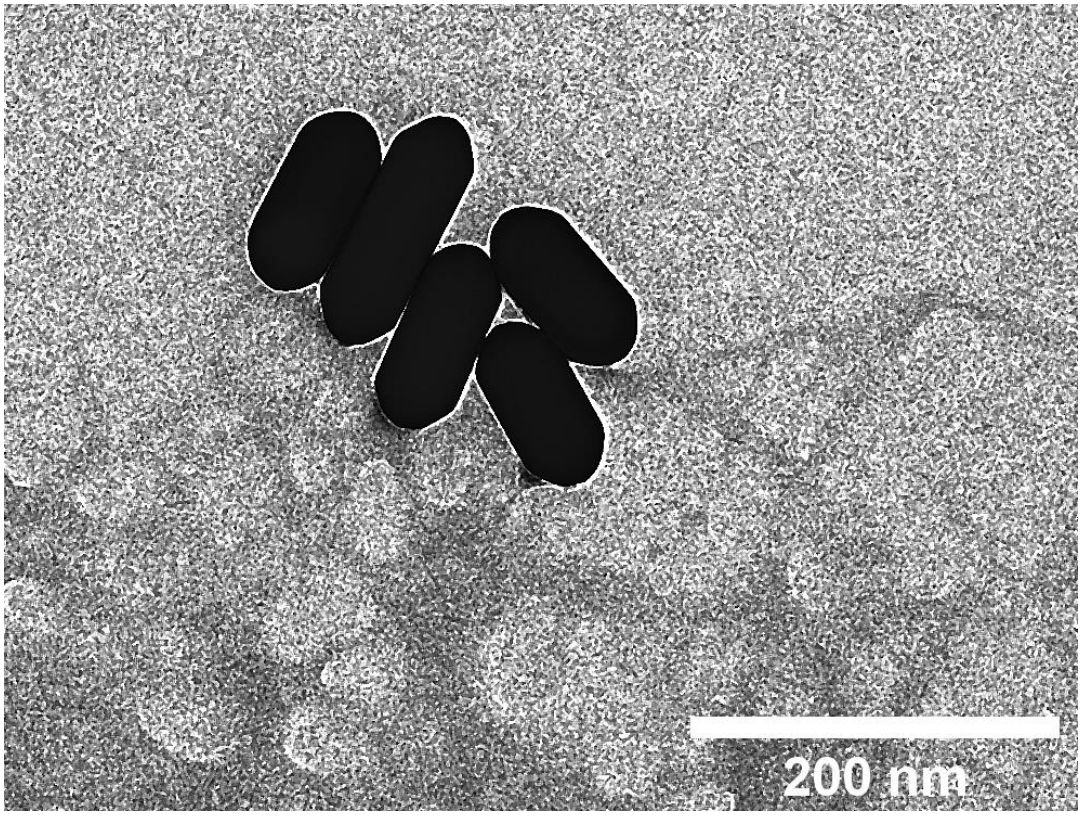

Figure 4.5: TEM of insulin amyloid and nanorods.
Bovine insulin amyloids mixed with gold nanorods and stained with thioflavin T imaged by TEM.

Under TEM, aggregates comprised of many fibrils were observed (light grey lines, Figure 4.5). Such aggregation often occurs for fibril samples prepared in this manner. There was still no long-range chiral ordering to the nanorods, but the nanorods formed small clusters of between two and five nanorods on the fibril aggregates (dark pill shapes, Figure 4.5). Additionally, the TEM images make clear an important difference between our work and the work from Liz-Marzan's group: the nanorods used in that study had dimensions of 23 nm × 7 nm, which allowed them to intercalate into the fibril grooves,[171] whereas we used nanorods of 80 nm × 40 nm to achieve high enough signal-to-noise for the single-particle scattering spectroscopy and fluorescence imaging. These larger gold nanorods still bind to amyloid fibrils due to electrostatic interaction with the fibril backbone. However, because of their size, they do not intercalate into the fibril groove and

thus can aggregate into side-to-side dimers, trimers, and bigger oligomers. This arrangement is also supported by the observed blue shift in the CD and absorbance spectra (Figure 4.2).[172]
In all three types of imaging, we observed a nearly equal portion of small aggregates and isolated monomeric nanorods bound to the fibril (Figure 4.6c). Long-range helical ordering of nanoparticles can be ruled out as the reason for induced CD from the current microscopy data, but we asked whether isolated single nanorods or these small aggregates are majorly responsible for the induced CD signal.

4.3.3 Photoluminescence-detected Circular Dichroism (PDCD) of Amyloid-bound Nanorods

Polarization-resolved fluorescence microscopy has a unique ability to probe the question of whether single nanorods or small aggregates are responsible for the induced CD signal near the LSPR wavelength. The image of both small aggregates and monomeric nanorods are diffraction-limited in the light microscope, so we are unable to observe the number or arrangement of the nanorods in an aggregate by fluorescence microscopy. However, monomers can be distinguished from aggregates based on their dark-field scattering spectra. Using the same method as in section 4.3.2, I searched for diffraction-limited spots that were ≤ 200 nm from the center peak of the nanorod's diffraction-limited spot to the center axis of the nearest fibril imaged under 488-nm excitation (Figure 4.6a). I then took a dark-field scattering spectrum from each of these spots (Figure 4.6 a-b, indicated by colored arrows). Monomeric nanorods were classified as those diffraction-limited spots with a single peak between 640 nm and 700 nm with a full-width at half maximum less than 70 nm (Figure 4.6b, top), whereas diffraction-limited spots were classified as aggregates when the scattering spectrum had a full-width at half maximum greater than 70 nm or when multiple peaks were identified (Figure 4.6b, bottom). Additionally, the scattering intensity

of the aggregates was ~2 × greater than that of the single nanorods (Figure 4.6b, bottom). From a sample of fibrils and nanorods across 5 days of imaging, 55% of the observed diffraction spots on fibrils were aggregates while 45% were to monomeric nanorods (Figure 4.6c).

After determining whether the spots were aggregates or monomeric nanorods, I switched to the 640-nm excitation channel, which falls near the maximum CD signal (Figure 4.2). The polarization microscope does not directly probe the absorbance of the nanorods and aggregates, but the photoluminescence of nanorods is a linear process, so I used the photoluminescence intensity as an indicator of the relative absorption between LCP and RCP excitation (sections 4.2.9 and 4.4.2). I term this method photoluminescence-detected circular dichroism (PDCD) and quantify the response with the photoluminescence dissymmetry factor, g_{PL}, (equation (4.1)). I collected a data set from of PDCD data from for six nanorod aggregates and six monomeric nanorods as determined by their dark-field scattering spectra (Figure 4.7).

The distribution of the measured g_{PL} values is shown for six nanorod aggregates and six monomeric nanorods in Figure 4.6c. The monomeric nanorods show negligible g_{PL} with an average of +0.31% (orange). In contrast, the g_{PL} values measured from nanorod aggregates (blue) vary widely with a meidan g_{PL} of −8.36%. A negative g_{PL} is observed for ~80% of the observed aggregates, which correlates with the observed negative bulk CD signal.

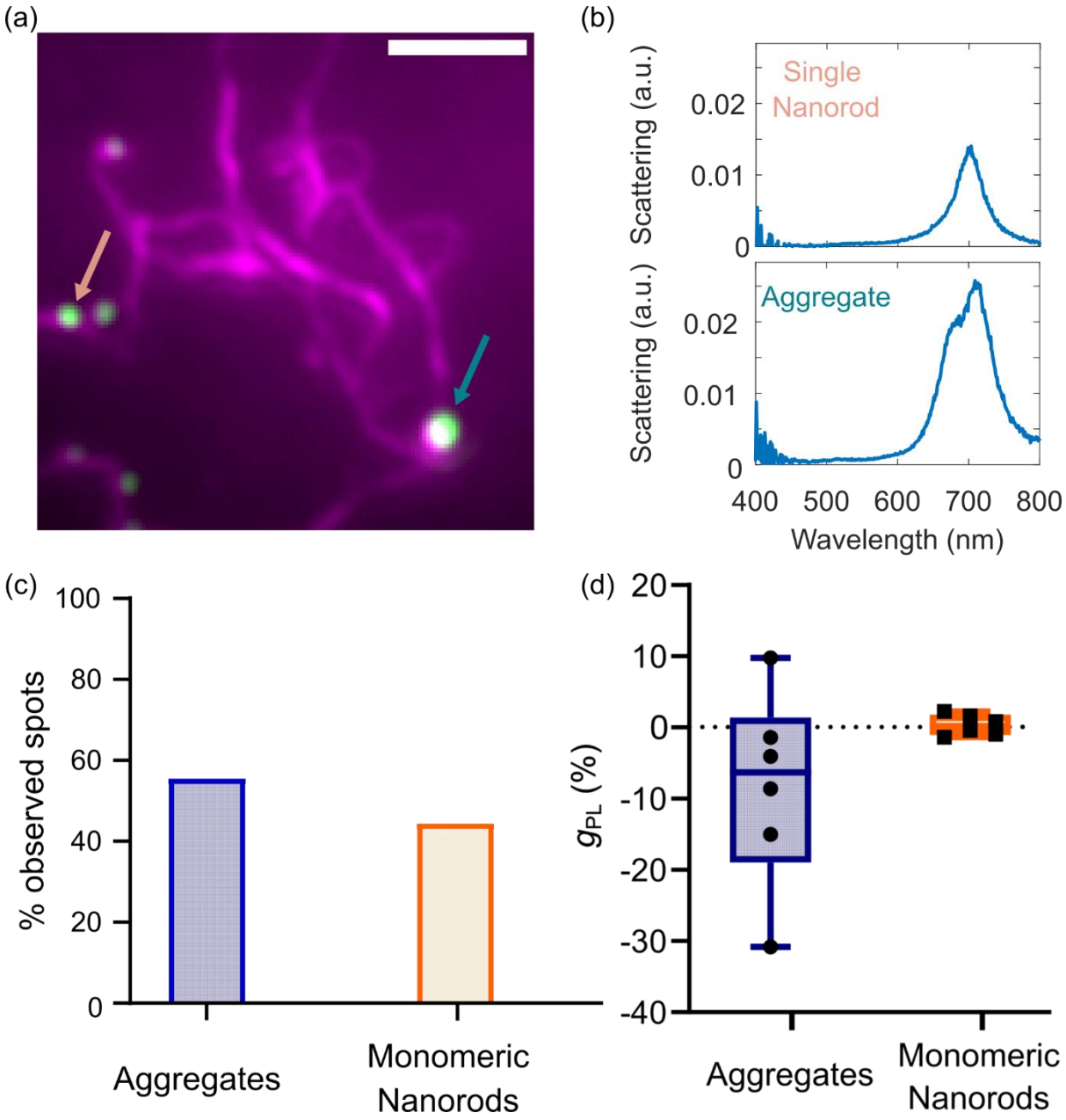

Figure 4.6: Polarization-resolved Fluorescence Microscopy of Monomeric Nanorods and Aggregates.

(a) Composite fluorescence image of ThT-labeled fibrils (purple) with bound gold nanorods (green). Scale bar: 1 μm. (b) Top: Scattering spectrum from the representative monomeric nanorod indicated by the orange arrow in (a). Bottom: Scattering spectrum from the representative nanorod aggregate indicated by the teal arrow in (a). (c) Bar chart showing relative percentages of aggregates and monomeric nanorods observed. (d) Box-and-whisker plot of measured g_{PL} values from six nanorod aggregates and six monomeric nanorods.

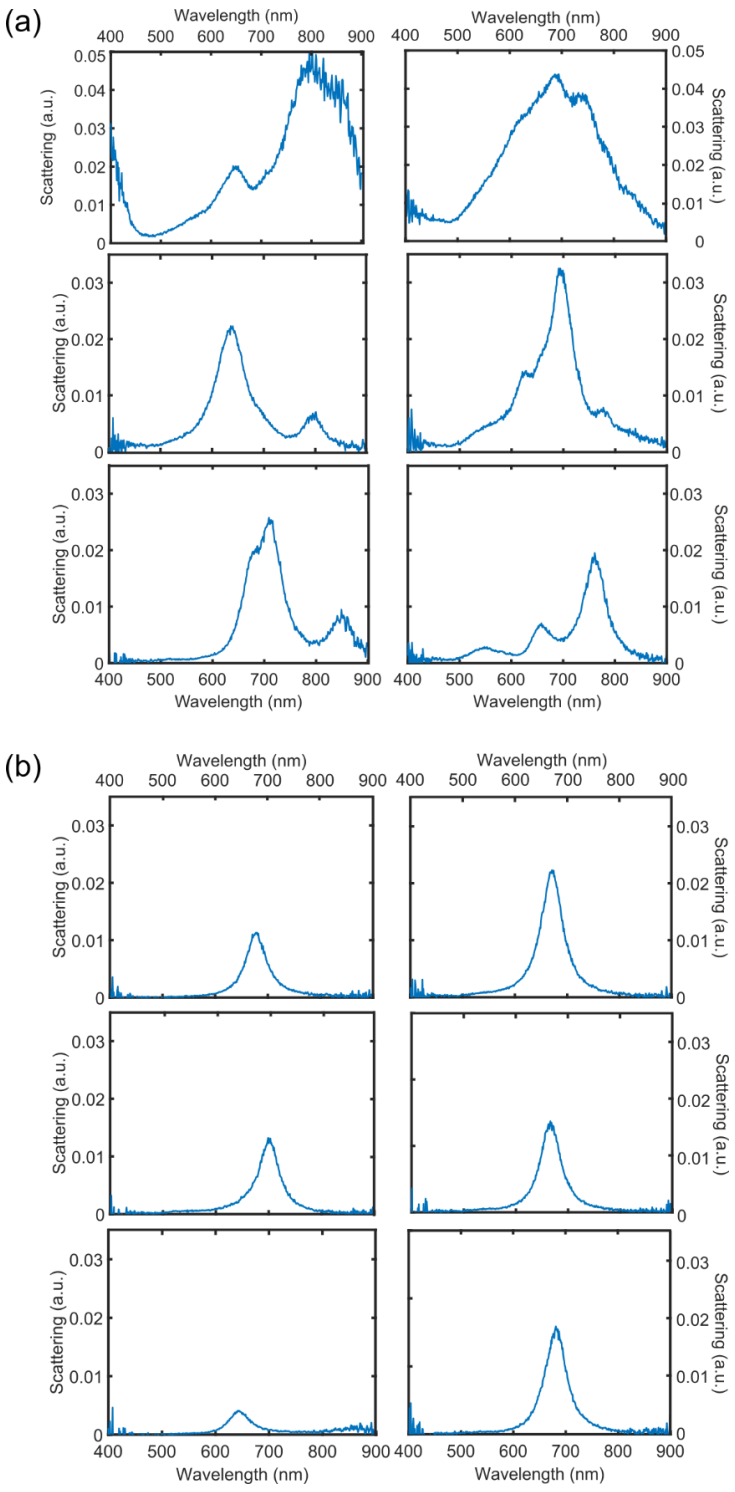

Figure 4.7: Dark-field scattering spectra from PDCD data set.
(a) Dark-field spectra from aggregates (b) Dark-field spectra from monomeric nanorods.

4.4 Conclusions and Outlook

4.4.1 Current Conclusions

With my collaborator Maciej Lipok, I showed that binding gold nanorods to ThT-stained insulin amyloids can induce a bulk CD signal at the LSPR wavelength. This induced signal occurs without the long-range helical order observed by Liz-Marzán's group.[171] Although I observed no detectable PDCD from monomeric nanorods, I observed a PDCD signal from small aggregates reaching a minimal dissymmetry of g_{PL} of −8% which is an order of magnitude greather than that for typical chiral organic molecules and twice the absorption dissymmetry factor observed by Liz-Marzán's group.[171,173] Most of the aggregates observed had the same sign for their PDCD as the bulk CD, indicating that this method may be able to detect fibril chirality while simultaneously performing fluorescence imaging.

4.4.2 Limitations on the Photoluminescence Dissymmetry Factor

One limitation of the study thus far has been the very small magnitude of the observed CD signal in bulk. I performed dimensional analysis to determine the expected magnitude of the photoluminescence dissymmetry factor from a monomeric nanorod based on the signal from the bulk spectrum. I use the Beer-Lambert law and the CD spectrum data to determine the absorption dissymmetry factor near the 640-nm wavelength from Figure 4.2 to assess if our microscope system can detect this dissymmetry factor. The absorption dissymmetry factor, g_{abs}, is calculated as:

$$g_{abs} = \frac{\Delta\varepsilon}{\varepsilon} \tag{4.2}$$

where $\Delta\varepsilon$ is the difference in molar absorption coefficient under LCP or RCP light:

$$\Delta\varepsilon = \varepsilon_{LCP} - \varepsilon_{RCP} \tag{4.3}$$

and ε is the molar absorption coefficient of an absorbing molecule or particle under randomly polarized light. In the power regimes used in this work, photoluminescence, like fluorescence, is a linear process, meaning one photon absorbed will be one photon emitted. Therefore, the measured g_{PL} should be proportional to g_{abs}.

The equation to convert CD in mdeg to $\Delta\varepsilon$ is:

$$\Delta\varepsilon = \frac{CD}{(32980 \times C \times l)} \tag{4.4}$$

where C is the molar concentration of absorbing species (moles/L), CD is the CD signal in mdeg, and l is the path length of the instrument in cm. This equation is derived from the Beer-Lambert law equation relating absorbance (A) to the molar absorption coefficient,

$$A = \varepsilon C l \tag{4.5}$$

combined with the conversion factor for CD in mdeg to absorbance which is 32980.[44] Absorbance is a unitless quantity since it is the base 10 log of the ratio of incident to transmitted radiant power.[174]

I convert the CD signal in mdeg at 640 nm (−0.5 mdeg, Figure 4.2a) to the difference in molar absorption coefficient, $\Delta\varepsilon$, according to:

$$\Delta\varepsilon = \frac{(-5 \times 10^{-1}\, mdeg)}{(3.298 \times 10^{4}\, mdeg) \times (1.9 \times 10^{-11}\, M) \times (2 \times 10^{-1} cm)} = -4 \times 10^{5}\, M^{-1} cm^{-1} \tag{4.6}$$

The expected change in molar absorption coefficient is on the order of 10^5 /(M cm). To get the relative dissymmetry, g_{abs}, we need the molar absorption coefficient, ε, for the nanorod under randomly polarized light. We have an absorbance spectrum (Figure 4.2b) along with the CD spectrum. I calculate the molar absorption from the Beer-Lambert Law. The absorbance at 640 nm is 0.15 so:

$$\varepsilon = \frac{0.15}{(1.9 \times 10^{-11}\, M) \times (2 \times 10^{-1}\, cm)} = 3.9 \times 10^{10} M^{-1} cm^{-1} \tag{4.7}$$

We can compare this measured molar absorption coefficient to the reported value from the manufacturer for these gold nanorods. From the manufacturer, the absorption coefficient at the reported peak LSPR wavelength of 650 nm is 1.94×10^{10} /(M cm). This is about 2 times smaller than the measured concentration from spectroscopy, so a correction may be needed in the future.

Finally, I can calculate the g_{abs} for the nanorods:

$$g_{abs} = \frac{\Delta\varepsilon}{\varepsilon} = \frac{-4 \times 10^5\ M^{-1}cm^{-1}}{3.9 \times 10^{10}\ M^{-1}cm^{-1}} \approx -1 \times 10^{-5} \tag{4.8}$$

Overall, from this conversion of the measured CD signal in mdeg to a dissymmetry factor, g_{abs}, I find that the bulk measurement corresponds to very small g-factors on the order of 1×10^{-5}.

I measured the photoluminescence intensity from a nanorod under 640-nm LCP or RCP excitation to obtain g_{PL}. For each excitation polarization, I measured the photoluminescence intensity for 1000 frames (40 s), and I took the time average of the photoluminescence intensity over the movie. The error on this intensity measurement is the standard error on the mean of this time average. Typical values for these standard errors are about ± 1% of the photoluminescence intensities we typically measure. Therefore, the lower limit for a detectable g_{PL} in our system is ± 1×10^{-2}.

The signal levels we expect at the single-particle level given the current bulk data (1×10^{-5}) are lower than the noise floor on our microscope setup (± 1% standard error on the mean for a single-nanorod intensity). However, I am making several assumptions that would serve to lower the expected signal level. For example, though I assume that all nanorods are bound to fibrils, the effective concentration is smaller and the expected g_{abs} are higher if a small percentage of monomeric nanorods bind to the fibrils, which is the result from fluorescence microscopy (section 4.3.2). These assumptions make the estimated order of magnitude for g_{abs} a lower limit. From our fluorescence microscopy, I estimate that 10% of all nanorods bind and 45% of these bound

nanorods are monomeric. Therefore, the expected g_{abs} for a monomeric nanorod would increase by a factor 1/0.045 according to equation (4.9).

$$g_{abs} = \frac{-1 \times 10^{-5}}{(0.045)} = -2 \times 10^{-4} \tag{4.9}$$

This g_{abs} is still lower than the detectable limit in our system.

Most of our noise in the microscope setup is due to photon shot noise. In the future, I can improve the precision of our measurement of nanorod PL intensity by taking longer movies (more imaging frames) or using higher excitation powers. Additionally, we can characterize more particles on and off fibrils and run statistics on these populations to increase our confidence in the measured dissymmetry factors. Overall, the current data, particularly the predominance of small bound aggregates, and this dimensional analysis strongly indicate that nanorod aggregates are responsible for the observed signal rather than monomeric nanorods. However, our current PDCD lower limit prevents us from definitively saying a monomeric nanorod does not have an induced CD signal on a fibril.

4.4.3 Future Directions

The study thus far has shown promising results in polarization-resolved microscopy for measuring fibril chirality *in situ*. However, I need a larger sample set to confirm that the CD signal indeed largely results from small aggregates of a few nanorods and to obtain a more precise measurement of the magnitude of the induced dissymmetry, g_{PL}, to ensure the single-particle PDCD signal correlates to the observed bulk CD signal.

Another important open question my polarization-resolved fluorescence microscopy can answer is how the presence of ThT affects the induced CD signal. In other amyloid-nanoparticle systems, our collaborators in Joanna Olesiak-Bańska's group has observed that the concentration

of ThT has a strong effect on the induced CD signal. A series of experiments measuring the g_{PL} at different ThT concentrations could be performed. Additionally, I can control the polarization of a 488-nm excitation laser to measure fluorescence-detected CD signals from ThT within a 200 nm radius of a fibril-bound nanorod's center or greater than 600 nm from the fibril bound nanorod center.

One other promising direction would be to determine if the orientation of the nanorods relative to the fibril long axis affects their CD signal or their interaction with ThT. The sign of the CD signal calculated for dipole coupling of a single chiral dipole to single nanoparticles is highly dependent on the angle of the dipole relative to the nanoparticle.[164,175] From our AFM data, we observed that the single nanorods are mostly bound with the nanorod axis along the fibril. Therefore, I could measure the orientation of the fibrils by observing the photoluminescence modulation under a rotating linear polarizer in a manner similar to studies performed by the Brasselet group.[176,177] I would then perform PDCD and quantify the photoluminescence dissymmetry for subsamples with different relative nanorod angles.

Chapter 5
Conclusions

5.1 Summary

The work in this thesis expands the polarization microscopy toolkit available to single-molecule microscopists in several ways. I built a polarimetric microscope system capable of resolving heterogeneous fluorescence dissymmetry signals from single particles (Chapter 2). I further demonstrated that this device could be used to provide spatial information beyond the diffraction limit about the near-field environment of a single molecule coupled to a gold nanodimer (Chapter 3). I discovered that the apparent emission from a cyanine dye near a nanodimer is localized or excluded from the nanodimer gap region depending on the far-field excitation polarization. I showed that this emission pattern results from detection bias introduced by the enhanced electric field near the nanodimer. My work also suggests that the optical chirality of the near-field redirects and twists fluorescence emission, causing an apparent fluorescence dissymmetry in the emission. I further applied polarization microscopy to learn about induced circular dichroism (CD) signals for gold nanorods bound to amyloid fibrils (Chapter 4). I determined that, in line with previous work on induced plasmonic CD signals, the major mechanism behind the induced CD signal is electromagnetic coupling between aggregates of multiple nanoparticles.[171]

5.2 Future Directions

In the future, the techniques and protocols I developed will be valuable to gain further insight into plasmon-enhanced chiroptical spectroscopy. Particularly, further insight into the connection between optical chirality and fluorescence dissymmetry established in Chapter 3 could aid the design of platforms for ultrasensitive enantiomer detection or separation. Extending amyloid sensing in Chapter 4 to bacterial biofilms could have broad impacts on human health. It would also be beneficial to investigate alternative materials for chiral plasmon-coupled fluorescence as these materials could broaden the wavelength range available for enhancement and potentially boost dissymmetry signals even higher than the results described in Chapter 3.

5.2.1 Chiral fluorescent molecules and optical chirality

Previous work in our lab and others has shown that mislocalization results from the emission coupling of nanoparticles and fluorescent molecules.[135,136,142] On the other hand, optical chirality is a property of an electromagnetic field and is related to the differential absorption of circularly polarized light by a molecule.[17,18] Our work and work from other labs establishes that the near-field optical chirality can be translated to far-field fluorescence dissymmetry measurements.[103,139,140] I interpreted the effect as directional coupling between the emission dipole moment and the polarized near field near a nanostructure along with bias from towards detecting molecules with the high-fluorescence intensity due to the local electric field (Chapter 3). Repeating the Points Accumulation for Imaging Nanoscale Topography (PAINT) experiments described in Chapter 3 at different excitation wavelengths with different achiral dyes would provide further evidence for this coupling interpretation, by removing the bias of the electric field enhancement.

I would first propose to do the experiment with two additional cyanine dyes, Cy3 and Cy5, which have fluorescence that can be excited at 515 nm and 561 nm, respectively. Previous work

in our lab has untangled absorption and emission contributions to mislocalization using these dye/excitation combinations.[74,142] We have shown that changing the electric field results in lower fluorescence intensity enhancement while still showing strong mislocalization. These dyes would have less absorption overlap with plasmon resonance of the nanodimer structure I designed, thus I would expect to see a lower overall enhancement of fluorescence intensity near a nanodimer than for Cy5.5 but stronger mislocalization and mispolarization.

Another important next step would be measuring fluorescence dissymmetry and mislocalization patterns near the nanodimer structure using a dye with an intrinsic absorption dissymmetry factor. Tang and Cohen directly related absorption dissymmetry factors to the optical chirality of the excitation field when they first formalized their optical chirality measure.[17] Experimental evidence has shown that absorption dissymmetry factors can be enhanced. [15] Curiously, Hendry et al. foun the absorption dissymmetry enhancement was several orders of magnitude larger than the enhancement of the optical chirality. It would, therefore, be useful to measure how the absorption dissymmetry changes as a function of optical chirality enhancement. Our nanodimer structure (Chapter 3) provides an excellent platform to test the effect of a change on optical chirality enhancement on the same chiral molecule as we can tune the optical chirality enhancement in the gap region as a function of offset (Chapter 3).

One readily available fluorescent emitter for such an experiment would be a J-aggregate of cyanine dyes arranged on double-stranded DNA. J-aggregates are often described as a pair of dyes that couple with their transition dipoles end-to-end, although the full picture of coupling is more complicated.[178] For our purposes, the importance of the J-aggregates of cyanine dyes is that they possess a CD signal in the visible range.[179,180] It has been shown that these visible range CD signals can be increased with coupling to plasmonic metal nanoparticles.[180] Therefore, performing the

experiments in Chapter 3 with a J-dimer of Cy5.5 instead of a Cy5.5 monomer, and comparing the magnitude of the total fluorescence intensity enhancement for the J-dimer to the monomer would give us experimental evidence of whether the optical chirality is directly proportional to the enhanced absorption dissymmetry in addition to twisting emission.

5.2.2 Measuring chirality of amyloid fibrils *in vivo*

The work in Chapter 4 studied the coupled nanoparticle-amyloid response *in vitro* on insulin fibrils. In addition to their toxicity in diseases, state-of-the-art research has shown that amyloids can have healthy biological functions.[181] Of particular interest to the microbiology community are the curli amyloid fibrils that form the scaffold for *E. coli* bacteria biofilms.[181,182]

This functional amyloid curli is formed from the protein CsgA by the bacteria *Escherichia coli* (*E. coli*). CsgA is a naturally unfolded protein that is secreted outside of the periplasm where it can assemble into curli fibrils.[181] Like all amyloid fibrils, curli fibrils are stabilized by cross β-sheet interactions (Figure 1a). Curli fibers are produced during the early-growth phase of biofilm formation, allowing cells to adhere to surfaces to start the process of colony formation. It has been shown that, upon assembly, extracellular functional amyloids form extremely stable secondary structures (Figure 1b).[183,184] This stability is linked to the structural rigidity of extracellular fibrils.

The length scale of amyloid fibrils has thus far limited studies of their structure to electron microscopy (EM) and atomic force microscopy (AFM) techniques.[157,185] These techniques require elaborate sample preparation which limits their throughput and precludes what curi fibril formation in real time. The high resolution, sensitivity, and specificity of single-molecule fluorescence microscopy could provide a route to access the nanometer length scale structure during real time bacteria growth. However, to gain information on the chiral structure of any amyloid with visible wavelength light, some sort of reporter probe is needed. For example, thioflavin T (ThT) and

achiral gold nanorods have been proposed as potential probes of amyloid chirality at visible wavelengths because their differential absorption will correspond to the chirality of the amyloid.[171,186] Particularly, gold nanorods integrated into amyloids have already shown strong promise as a method for ultrasensitive detection of fibril formation.[171]

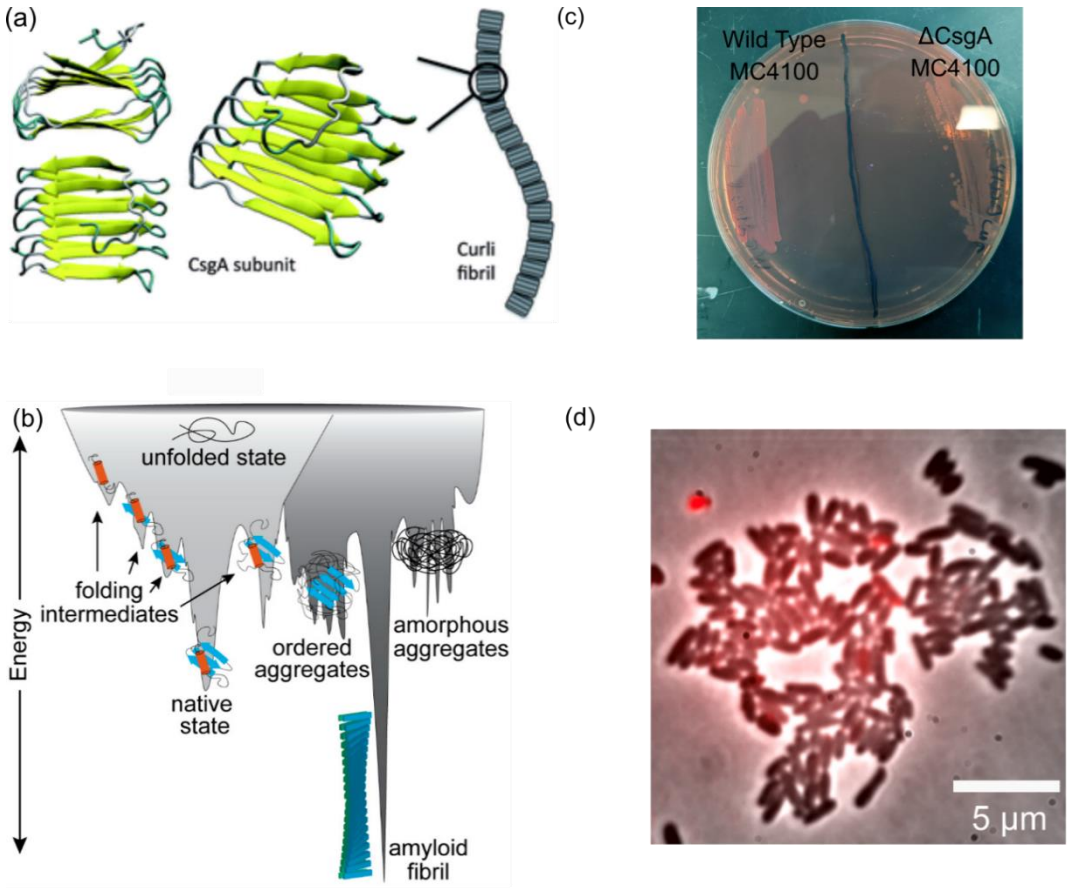

Figure 5.1: Curli amyloid biofilms.
(a) Diagram of curli fibril showing CsgA subunit folding into a β-sheet structure. Adapted from Ref. 187[187] (b) Energy diagram showing strong stability of amyloid fibrils. Adapted from Ref. 188[188] (c) MC4100 *E. coli* wild type and curli deficient strains grown on YESCA plate. Red stain can be seen on the wild type but absent from the curli deletion strain (d) Image of WT MC4100 *E. coli* on agarose pad. Fluorescence of Congo red excited at 532 nm and collected at wavelengths longer than 542 nm, overlaid on phase contrast image.

5.2.3 Methods for E. coli Biofilm Growth

In collaboration with my colleague, Adam Decker, I implemented and tested the following methods for growing *E. coli* biofilms and performing fluorescence imaging with the fluorescent dye, Congo red, as a first step toward determining if single-molecule or single-particle microscopy could be used to sense amyloid chirality *in vivo*. Congo red is a dye commonly used to confirm presence of amyloid formation.[189–192] Congo red has largely been superseded by ThT in assays testing for fibrillation due to its lack of specificity for amyloid. It has, however, been shown to be good indicator of biofilm formation when compared to control bacteria that do not produce amyloid protein particularly because it does not inhibit normal bacteria function and growth.[191] I grew the amyloid biofilms as evidenced by the red color stain of colonies with congo red (Figure 1c). I describe those methods here for future students to build upon.

MC4100 wild type (WT) and curli-deficient (ΔCsgA) *E. coli* strains were obtained from the Chapman lab at the University of Michigan. Cells were grown for 72 hours on a YESCA agar plate. YESCA agarose pads were prepared and dyed with 0.05% w/v and 0.005% w/v congo red prior to pipetting and set on 22 mm × 22 mm glass coverslips that were argon plasma etched. Individually, colonies were scraped off the plate using the back of an inoculation loop and suspended in 100 μL of YESCA minimal media. 10 μL of cells were pipetted onto congo red agarose pads and imaged under the white light in a widefield microscope equipped with a phase condenser and 100×, 1.4 NA oil-immersion objective. After acquiring a phase contrast image of the *E. coli* cells, I excited the fluorescence with a 532-nm laser and imaged the same area as the phase contrast image in epifluorescence geometry. The emission passed through a dichroic filter and a long-pass filter with edge 542-nm edge wavelength to filter out the excitation beam scattering. I observed low-intensity fluorescence from areas with *E. coli* cells (Figure 2d).

However, I did not observe fluorescent fiber structure like the in vitro ThT-stained fibrils in Chapter 4. Further work needs to be done to develop a method to image congo red stained biofilms on the fluorescence microscope.

The next step for developing this protocol would be to directly image the MC4100 *E. coli* cells on congo red YESCA agar plates.[193] One should grow cells on the congo red YESCA plates as described and then cut out a thin section of the agar plate with a single colony for imaging. If imaging the biofilms and amyloid fibrils under 532-nm excitation is possible, one could potentially add a small portion of gold nanorods on top of the agarose pad and see if they bind to the biofilm through electrostatistic interaction as in Chapter 4. Determining whether it would be possible to couple plasmonic nanorods to the amyloid fibrils in a bacteria biofilm and whether the nanorod's induced differential signal under LCP and RCP excitation (see Chapter 4) would be a good readout for the chirality of the amyloid fibrils *in vivo* could help researchers access structural information on biofilm amyloid fibrils during different growth phases or growth conditions of bacteria.

5.2.4 Silver plasmon-enhanced fluorescence in biologically relevant environments

Gold plasmonic nanoparticles are useful in many studies. However, their plasmon resonance can only be tuned to a minimum wavelength of around 520 nm because gold's interband transitions dampen the plasmon at shorter wavelengths.[194] Silver and aluminum can be tuned into the bluer visible and UV wavelengths and both are plamonic materials that support strong local surface plasmon resonance modes.[194] Although silver and aluminum nanoparticles have resonance tunable to these wavelengths, their application has been limited in biological studies because they readily oxidize in aqueous environments (Figure 5.2a). Furthermore, exciting silver and aluminum

with a laser and additional oxidizing species dissolved in the solution can increase the rate of this oxidation.[195]

Indeed, many of the optically active transitions for biomolecules are at ultraviolet and shorter visible wavelengths.[164,175] Certain fluorescent dyes that bind to nucleic acids also are excited in the ~500 nm wavelength region (Figure 5.2b, green lines). One example of such a dye is thiazole orange (TO).

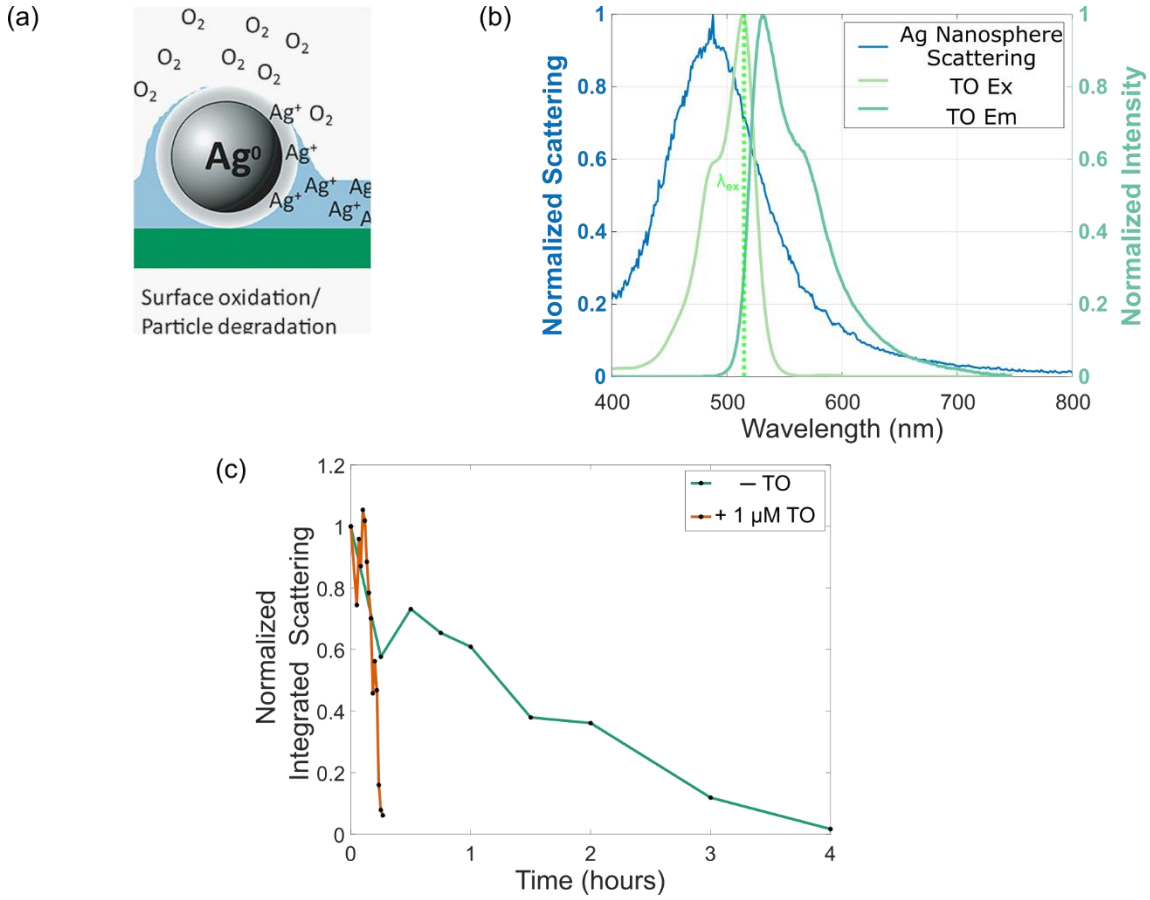

Figure 5.2: Silver nanosphere oxidation and spectral properties.
(a) Diagram of silver nanosphere oxidation in an aqueous environment. Dissolved oxygen in the water will oxidize Ag^0 to Ag^+. Adapted from [196]. (b) Dark-field scattering spectrum of a single Ag nanosphere with 75 nm diameter (blue), TO excitation and emission spectra (light green and dark green, respectively). The dotted line indicates the excitation wavelength (λ_{ex} = 515 nm). (c) Integrated scattering of a silver nanosphere over time in the presence (green line) and absence (orange line) of TO.

In collaboration with my colleague Shelby Nicolau, I studied the degradation of silver nanospheres over time in a solution of TO. I drop-cast Ag nanospheres with diameters near 75 nm (NanoComposix Product No. AGPO75-1M) onto an coverslip that had been plasma cleaned with oxygen (Yield Engineering Systems, YES-CV200RFS) and took scattering spectra of one nanoparticle (Figure 5.2b, blue line) at fixed time points over time. I excited the nanoparticles with a 515-nm CW laser at 62.1 mW/mm^2 in between taking the scattering spectra. I calculated the integral of the scattering spectra intensity from 400 nm – 800 nm using the trapezoidal rule and divided these integrals by the integrated intensity at t = 0 to obtain the normalized scattering intensity at every time point.

A 1 μM concentration of TO decreased the time for the nanoparticles to completely oxidize by an order of magnitude relative to pure double-distilled H_2O (Figure 5.2c). However, even without dye, silver nanoparticles in an aqueous solution degrade completely after ~ 4 hours under 62.1 mW/mm^2 515-nm excitation. In future projects coupling silver nanoparticles to chiral molecules, one would need to develop an approach to prevent the fast degradation of silver nanoparticles in the presence of fluorescent molecules and aqueous solvents.

Two potential options to prevent degradation would be protecting the particles with polymer layers or coating the particles with a thin layer of gold or silica. Experiments similar to the degradation experiment in Figure 2c would establish whether polymer layers of poly(diallyldimethylammonium chloride) and poly(sodium 4-styrene) as used in Chapter 3 can protect silver nanospheres from degradation.[85] NanoComposix also sells silica-shelled silver nanospheres directly (Product No. AGAH50-1M). The company can customize nanospheres with different capping agents and core-shell layers with shell thicknesses down to 15 nm. Coating a

silver particle with a thin gold layer could be a route for achieving bluer plasmon resonances while maintaining compatibility with bacteria as the oxidizing silver is known to be antimicrobial.[196]

5.3 Conclusions and Outlook

Chiral plasmonics and enhanced fluorescence dissymmetry have been established as important research directions in physical chemistry and spectroscopy, but most of the studies have been performed on bulk samples and thus are unable to observe heterogeneities that arise on the nanometer scale, for instance due to heterogeneities in the local environment near a metal nanoparticle or surface.[181] This thesis expands studies of chiral plasmon-enhanced fluorescence to the single-molecule and single-particle level, and it increases our understanding of the biosensing abilities of nanoparticles applied to amyloid fibrils. Extending the abilities of polarization microscopy to sense the chirality of single biomolecules will be a fast-growing research area with the potential to affect areas as diverse as human health and materials science.

Bibliography

(1) Mason, S. Biomolecular Homochirality. *Chem. Soc. Rev.* **1988**, *17* (0), 347–359. https://doi.org/10.1039/CS9881700347.

(2) Bonner, W. A. Chirality and Life. *Origins Life Evol Biosphere* **1995**, *25* (1), 175–190. https://doi.org/10.1007/BF01581581.

(3) Blackmond, D. G. The Origin of Biological Homochirality. *Cold Spring Harb Perspect Biol* **2010**, *2* (5), a002147. https://doi.org/10.1101/cshperspect.a002147.

(4) Capozziello, S.; Lattanzi, A. Spiral Galaxies as Chiral Objects? *Astrophys Space Sci* **2006**, *301* (1), 189–193. https://doi.org/10.1007/s10509-006-1984-6.

(5) *Chiral asymmetry in spiral galaxies? - Kondepudi - 2001 - Chirality - Wiley Online Library*. https://onlinelibrary.wiley.com/doi/10.1002/chir.1044 (accessed 2023-02-22).

(6) Brooks, W. H.; Guida, W. C.; Daniel, K. G. The Significance of Chirality in Drug Design and Development. *Current Topics in Medicinal Chemistry 11* (7), 760–770.

(7) Laurent, G.; Lacoste, D.; Gaspard, P. Emergence of Homochirality in Large Molecular Systems. *Proceedings of the National Academy of Sciences* **2021**, *118* (3), e2012741118. https://doi.org/10.1073/pnas.2012741118.

(8) Blackmond, D. G. The Origin of Biological Homochirality. *Cold Spring Harb Perspect Biol* **2010**, *2* (5), a002147. https://doi.org/10.1101/cshperspect.a002147.

(9) Quack, M.; Seyfang, G.; Wichmann, G. Perspectives on Parity Violation in Chiral Molecules: Theory, Spectroscopic Experiment and Biomolecular Homochirality. *Chem. Sci.* **2022**, *13* (36), 10598–10643. https://doi.org/10.1039/D2SC01323A.

(10) Vantomme, G.; Crassous, J. Pasteur and Chirality: A Story of How Serendipity Favors the Prepared Minds. *Chirality* **2021**, *33* (10), 597–601. https://doi.org/10.1002/chir.23349.

(11) Hein, J. E.; Huynh Cao, B.; Viedma, C.; Kellogg, R. M.; Blackmond, D. G. Pasteur's Tweezers Revisited: On the Mechanism of Attrition-Enhanced Deracemization and Resolution of Chiral Conglomerate Solids. *J. Am. Chem. Soc.* **2012**, *134* (30), 12629–12636. https://doi.org/10.1021/ja303566g.

(12) Rougeot, C.; Hein, J. E. Application of Continuous Preferential Crystallization to Efficiently Access Enantiopure Chemicals. *Org. Process Res. Dev.* **2015**, *19* (12), 1809–1819. https://doi.org/10.1021/acs.oprd.5b00141.

(13) Hecht, Eugene. *Optics*, 3rd ed.; Addison-Wesley: Reading, Mass., 1998.

(14) Rodger, Alison.; Nordén, B., 1945-. *Circular Dichroism and Linear Dichroism*; Oxford chemistry masters ; 1; Oxford University Press: Oxford ; New York, 1997.

(15) Hendry, E.; Carpy, T.; Johnston, J.; Popland, M.; Mikhaylovskiy, R. V.; Lapthorn, A. J.; Kelly, S. M.; Barron, L. D.; Gadegaard, N.; Kadodwala, M. Ultrasensitive Detection and Characterization of Biomolecules Using Superchiral Fields. *Nature Nanotech* **2010**, *5* (11), 783–787. https://doi.org/10.1038/nnano.2010.209.

(16) Tullius, R.; Karimullah, A. S.; Rodier, M.; Fitzpatrick, B.; Gadegaard, N.; Barron, L. D.; Rotello, V. M.; Cooke, G.; Lapthorn, A.; Kadodwala, M. "Superchiral" Spectroscopy: Detection of Protein Higher Order Hierarchical Structure with Chiral Plasmonic Nanostructures. *J. Am. Chem. Soc.* **2015**, *137* (26), 8380–8383. https://doi.org/10.1021/jacs.5b04806.

(17) Tang, Y.; Cohen, A. E. Optical Chirality and Its Interaction with Matter. *Phys. Rev. Lett.* **2010**, *104* (16), 163901. https://doi.org/10.1103/PhysRevLett.104.163901.

(18) Tang, Y.; Cohen, A. E. Enhanced Enantioselectivity in Excitation of Chiral Molecules by Superchiral Light. *Science* **2011**, *332* (6027), 333–336. https://doi.org/10.1126/science.1202817.

(19) Solomon, M. L.; Abendroth, J. M.; Poulikakos, L. V.; Hu, J.; Dionne, J. A. Fluorescence-Detected Circular Dichroism of a Chiral Molecular Monolayer with Dielectric Metasurfaces. *J. Am. Chem. Soc.* **2020**, *142* (43), 18304–18309. https://doi.org/10.1021/jacs.0c07140.

(20) Indukuri, S. R. K. C.; Frydendahl, C.; Sharma, N.; Mazurski, N.; Paltiel, Y.; Levy, U. Enhanced Chiral Sensing at the Few-Molecule Level Using Negative Index Metamaterial Plasmonic Nanocuvettes. *ACS Nano* **2022**, *16* (10), 17289–17297. https://doi.org/10.1021/acsnano.2c08090.

(21) Stachelek, P.; MacKenzie, L.; Parker, D.; Pal, R. Circularly Polarised Luminescence Laser Scanning Confocal Microscopy to Study Live Cell Chiral Molecular Interactions. *Nat Commun* **2022**, *13* (1), 553. https://doi.org/10.1038/s41467-022-28220-z.

(22) Green, D. W.; Lee, J.-M.; Kim, E.-J.; Lee, D.-J.; Jung, H.-S. Chiral Biomaterials: From Molecular Design to Regenerative Medicine. *Advanced Materials Interfaces* **2016**, *3* (6), 1500411. https://doi.org/10.1002/admi.201500411.

(23) Porter, J. R. Antony van Leeuwenhoek: Tercentenary of His Discovery of Bacteria. *Bacteriological Reviews* **1976**, *40* (2), 260–269. https://doi.org/10.1128/br.40.2.260-269.1976.

(24) Lakowicz, J. R. author. aut http://id.loc.gov/vocabulary/relators/aut. *Principles of Fluorescence Spectroscopy*, 3rd ed. 2006.; Springer US : Imprint: Springer, 2006.

(25) Ruhlandt, D.; Andresen, M.; Jensen, N.; Gregor, I.; Jakobs, S.; Enderlein, J.; Chizhik, A. I. Absolute Quantum Yield Measurements of Fluorescent Proteins Using a Plasmonic Nanocavity. *Commun Biol* **2020**, *3* (1), 1–7. https://doi.org/10.1038/s42003-020-01316-2.

(26) Frei, M. S.; Tarnawski, M.; Roberti, M. J.; Koch, B.; Hiblot, J.; Johnsson, K. Engineered HaloTag Variants for Fluorescence Lifetime Multiplexing. *Nat Methods* **2022**, *19* (1), 65–70. https://doi.org/10.1038/s41592-021-01341-x.

(27) Los, G. V.; Encell, L. P.; McDougall, M. G.; Hartzell, D. D.; Karassina, N.; Zimprich, C.; Wood, M. G.; Learish, R.; Ohana, R. F.; Urh, M.; Simpson, D.; Mendez, J.; Zimmerman, K.; Otto, P.; Vidugiris, G.; Zhu, J.; Darzins, A.; Klaubert, D. H.; Bulleit, R. F.; Wood, K. V. HaloTag: A Novel Protein Labeling Technology for Cell Imaging and Protein Analysis. *ACS Chem. Biol.* **2008**, *3* (6), 373–382. https://doi.org/10.1021/cb800025k.

(28) Lukyanov, K. A.; Chudakov, D. M.; Lukyanov, S.; Verkhusha, V. V. Photoactivatable Fluorescent Proteins. *Nat Rev Mol Cell Biol* **2005**, *6* (11), 885–890. https://doi.org/10.1038/nrm1741.

(29) Dempsey, G. T.; Bates, M.; Kowtoniuk, W. E.; Liu, D. R.; Tsien, R. Y.; Zhuang, X. Photoswitching Mechanism of Cyanine Dyes. *J. Am. Chem. Soc.* **2009**, *131* (51), 18192–18193. https://doi.org/10.1021/ja904588g.

(30) Levitus, M.; Ranjit, S. Cyanine Dyes in Biophysical Research: The Photophysics of Polymethine Fluorescent Dyes in Biomolecular Environments. *Quarterly Reviews of Biophysics* **2011**, *44* (1), 123–151. https://doi.org/10.1017/S0033583510000247.

(31) Ha, T. Single-Molecule Fluorescence Resonance Energy Transfer. *Methods* **2001**, *25* (1), 78–86. https://doi.org/10.1006/meth.2001.1217.

(32) Bates, M.; Huang, B.; Dempsey, G. T.; Zhuang, X. Multicolor Super-Resolution Imaging with Photo-Switchable Fluorescent Probes. *Science* **2007**, *317* (5845), 1749–1753. https://doi.org/10.1126/science.1146598.

(33) Heilemann, M.; Margeat, E.; Kasper, R.; Sauer, M.; Tinnefeld, P. Carbocyanine Dyes as Efficient Reversible Single-Molecule Optical Switch. *J. Am. Chem. Soc.* **2005**, *127* (11), 3801–3806. https://doi.org/10.1021/ja044686x.

(34) Shindy, H. A. Fundamentals in the Chemistry of Cyanine Dyes: A Review. *Dyes and Pigments* **2017**, *145*, 505–513. https://doi.org/10.1016/j.dyepig.2017.06.029.

(35) Sorour, M. I.; Kistler, K. A.; Marcus, A. H.; Matsika, S. Accurate Modeling of Excitonic Coupling in Cyanine Dye Cy3. *J. Phys. Chem. A* **2021**, *125* (36), 7852–7866. https://doi.org/10.1021/acs.jpca.1c05556.

(36) Biancalana, M.; Koide, S. Molecular Mechanism of Thioflavin-T Binding to Amyloid Fibrils. *Biochim Biophys Acta* **2010**, *1804* (7), 1405–1412. https://doi.org/10.1016/j.bbapap.2010.04.001.

(37) Mustroph, H. Cyanine Dyes. *Physical Sciences Reviews* **2020**, *5* (5). https://doi.org/10.1515/psr-2019-0145.

(38) Lepkowicz, R. S.; Przhonska, O. V.; Hales, J. M.; Fu, J.; Hagan, D. J.; Van Stryland, E. W.; Bondar, M. V.; Slominsky, Y. L.; Kachkovski, A. D. Nature of the Electronic Transitions in Thiacarbocyanines with a Long Polymethine Chain. *Chemical Physics* **2004**, *305* (1), 259–270. https://doi.org/10.1016/j.chemphys.2004.06.063.

(39) Owens, E. A.; Hyun, H.; Dost, T. L.; Lee, J. H.; Park, G.; Pham, D. H.; Park, M. H.; Choi, H. S.; Henary, M. Near-Infrared Illumination of Native Tissues for Image-Guided Surgery. *J. Med. Chem.* **2016**, *59* (11), 5311–5323. https://doi.org/10.1021/acs.jmedchem.6b00038.

(40) Dost, T. L.; Gressel, M. T.; Henary, M. Synthesis and Optical Properties of Pentamethine Cyanine Dyes With Carboxylic Acid Moieties. *Anal Chem Insights* **2017**, *12*, 1177390117711938. https://doi.org/10.1177/1177390117711938.

(41) Andrews, S. S.; Tretton, J. Physical Principles of Circular Dichroism. *J. Chem. Educ.* **2020**, *97* (12), 4370–4376. https://doi.org/10.1021/acs.jchemed.0c01061.

(42) Kelley, A. Myers. *Condensed-Phase Molecular Spectroscopy and Photophysics*; Wiley: Hoboken, N.J., 2013.

(43) Bransden, B. H., 1926-; Joachain, C. J. (Charles J. *Physics of Atoms and Molecules*; Longman: London ; New York, 1983.

(44) Rodger, Alison.; Nordén, B., 1945-. *Circular Dichroism and Linear Dichroism*; Oxford chemistry masters ; 1; Oxford University Press: Oxford ; New York, 1997.

(45) Velluz, L., 1900-; Le Grand, M., joint author.; Grosjean, M., joint author. *Optical Circular Dichroism: Principles, Measurements, and Applications*; Verlag Chemie; Academic Press: Weinheim, New York, 1965.

(46) Inoue, Y., 1949-; Ramamurthy, V. *Chiral Photochemistry*; Molecular and supramolecular photochemistry ; 11; Marcel Dekker: New York, 2004.

(47) Solomon, M. L.; Saleh, A. A. E.; Poulikakos, L. V.; Abendroth, J. M.; Tadesse, L. F.; Dionne, J. A. Nanophotonic Platforms for Chiral Sensing and Separation. *Acc. Chem. Res.* **2020**, *53* (3), 588–598. https://doi.org/10.1021/acs.accounts.9b00460.

(48) Born, M. *Principles of Optics: 60th Anniversary Edition*; Cambridge University Press. https://doi.org/10.1017/9781108769914.

(49) Rayleigh. XXXI. Investigations in Optics, with Special Reference to the Spectroscope. *The London, Edinburgh, and Dublin Philosophical Magazine and Journal of Science* **1879**, *8* (49), 261–274. https://doi.org/10.1080/14786447908639684.

(50) Wiklund, M.; Brismar, H.; Önfelt, B. Acoustofluidics 18: Microscopy for Acoustofluidic Micro-Devices. *Lab Chip* **2012**, *12* (18), 3221–3234. https://doi.org/10.1039/C2LC40757D.

(51) Tuson, H. H.; Biteen, J. S. Unveiling the Inner Workings of Live Bacteria Using Super-Resolution Microscopy. *Anal. Chem.* **2015**, *87* (1), 42–63. https://doi.org/10.1021/ac5041346.

(52) Bingen, P.; Reuss, M.; Engelhardt, J.; Hell, S. W. Parallelized STED Fluorescence Nanoscopy. *Opt. Express, OE* **2011**, *19* (24), 23716–23726. https://doi.org/10.1364/OE.19.023716.

(53) Thompson, R. E.; Larson, D. R.; Webb, W. W. Precise Nanometer Localization Analysis for Individual Fluorescent Probes. *Biophysical Journal* **2002**, *82* (5), 2775–2783. https://doi.org/10.1016/S0006-3495(02)75618-X.

(54) Needham, L.-M.; Weber, J.; Varela, J. A.; Fyfe, J. W. B.; Do, D. T.; Xu, C. K.; Tutton, L.; Cliffe, R.; Keenlyside, B.; Klenerman, D.; Dobson, C. M.; Hunter, C. A.; Müller, K. H.; O'Holleran, K.; Bohndiek, S. E.; Snaddon, T. N.; Lee, S. F. ThX – a next-Generation Probe for the Early Detection of Amyloid Aggregates. *Chem. Sci.* **2020**, *11* (18), 4578–4583. https://doi.org/10.1039/C9SC04730A.

(55) Spehar, K.; Ding, T.; Sun, Y.; Kedia, N.; Lu, J.; Nahass, G. R.; Lew, M. D.; Bieschke, J. Super-Resolution Imaging of Amyloid Structures over Extended Times by Using Transient Binding of Single Thioflavin T Molecules. *ChemBioChem* **2018**, *19* (18), 1944–1948. https://doi.org/10.1002/cbic.201800352.

(56) Zhuang, X. Nano-Imaging with STORM. *Nature Photon* **2009**, *3* (7), 365–367. https://doi.org/10.1038/nphoton.2009.101.

(57) Betzig, E.; Patterson, G. H.; Sougrat, R.; Lindwasser, O. W.; Olenych, S.; Bonifacino, J. S.; Davidson, M. W.; Lippincott-Schwartz, J.; Hess, H. F. Imaging Intracellular Fluorescent Proteins at Nanometer Resolution. *Science* **2006**, *313* (5793), 1642–1645. https://doi.org/10.1126/science.1127344.

(58) Hess, S. T.; Girirajan, T. P. K.; Mason, M. D. Ultra-High Resolution Imaging by Fluorescence Photoactivation Localization Microscopy. *Biophysical Journal* **2006**, *91* (11), 4258–4272. https://doi.org/10.1529/biophysj.106.091116.

(59) Sharonov, A.; Hochstrasser, R. M. Wide-Field Subdiffraction Imaging by Accumulated Binding of Diffusing Probes. *Proceedings of the National Academy of Sciences* **2006**, *103* (50), 18911–18916. https://doi.org/10.1073/pnas.0609643104.

(60) Sharonov, A.; Hochstrasser, R. M. Wide-Field Subdiffraction Imaging by Accumulated Binding of Diffusing Probes. *PNAS* **2006**, *103* (50), 18911–18916. https://doi.org/10.1073/pnas.0609643104.

(61) Geilmann, W. Crystals and the Polarising Microscope, A Handbook for Chemists and Others, von N. H. Hartshorne Und A. Stuart. Verlag Edward Arnold, Ltd., London 1960. 3. Aufl., XV, 557 S., 338 Abb., Geb. £ 4.—.—. *Angewandte Chemie* **1963**, *75* (19), 947–947. https://doi.org/10.1002/ange.19630751942.

(62) Rosenberger, H. E. Differential Interference Contrast Microscopy. In *Interpretive Techniques for Microstructural Analysis*; McCall, J. L., French, P. M., Eds.; Springer US: Boston, MA, 1977; pp 79–104. https://doi.org/10.1007/978-1-4684-2370-9_5.

(63) Mickols, W.; Maestre, M. F.; Tinoco, I.; Embury, S. H. Visualization of Oriented Hemoglobin S in Individual Erythrocytes by Differential Extinction of Polarized Light. *Proceedings of the National Academy of Sciences* **1985**, *82* (19), 6527–6531. https://doi.org/10.1073/pnas.82.19.6527.

(64) Weigert, F. Über Polarisiertes Fluoreszenzlicht. *Verh. Dtsch. Phys. Ges.* **1920**, *23*, 100–102.

(65) Wawilow, S. J.; Lewschin, W. L. Beiträge Zur Frage Über Polarisiertes Fluoreszenzlicht von Farbstofflösungen. II: Die Bestätigung Des Weigertschen Fluoreszenzeffekts Und Neue Beobachtungen. *Zeitschrift für Physik* **1923**, *16* (1), 135–154.

(66) *Malus's Law*. https://spie.org/publications/fg05_p03_maluss_law?SSO=1 (accessed 2023-03-01).

(67) Bruggeman, E.; Zhang, O.; Needham, L.-M.; Körbel, M.; Daly, S.; Cheetham, M.; Peters, R.; Wu, T.; Klymchenko, A. S.; Davis, S. J.; Paluch, E. K.; Klenerman, D.; Lew, M. D.; O'Holleran, K.; Lee, S. F. POLCAM: Instant Molecular Orientation Microscopy for the Life Sciences. bioRxiv February 8, 2023, p 2023.02.07.527479. https://doi.org/10.1101/2023.02.07.527479.

(68) Ding, T.; Ding, T.; Wu, T.; Wu, T.; Mazidi, H.; Mazidi, H.; Zhang, O.; Zhang, O.; Lew, M. D.; Lew, M. D.; Lew, M. D. Single-Molecule Orientation Localization Microscopy for Resolving Structural Heterogeneities between Amyloid Fibrils. *Optica, OPTICA* **2020**, *7* (6), 602–607. https://doi.org/10.1364/OPTICA.388157.

(69) Backer, A. S.; Lee, M. Y.; Moerner, W. E. Enhanced DNA Imaging Using Super-Resolution Microscopy and Simultaneous Single-Molecule Orientation Measurements. *Optica, OPTICA* **2016**, *3* (6), 659–666. https://doi.org/10.1364/OPTICA.3.000659.

(70) Hafi, N.; Grunwald, M.; van den Heuvel, L. S.; Aspelmeier, T.; Chen, J.-H.; Zagrebelsky, M.; Schütte, O. M.; Steinem, C.; Korte, M.; Munk, A.; Walla, P. J. Fluorescence Nanoscopy by Polarization Modulation and Polarization Angle Narrowing. *Nat Methods* **2014**, *11* (5), 579–584. https://doi.org/10.1038/nmeth.2919.

(71) Curcio, V.; Alemán-Castañeda, L. A.; Brown, T. G.; Brasselet, S.; Alonso, M. A. Birefringent Fourier Filtering for Single Molecule Coordinate and Height Super-Resolution Imaging with Dithering and Orientation. *Nat Commun* **2020**, *11* (1), 5307. https://doi.org/10.1038/s41467-020-19064-6.

(72) Rimoli, C. V.; Valades-Cruz, C. A.; Curcio, V.; Mavrakis, M.; Brasselet, S. 4polar-STORM Polarized Super-Resolution Imaging of Actin Filament Organization in Cells. *Nat Commun* **2022**, *13* (1), 301. https://doi.org/10.1038/s41467-022-27966-w.

(73) Saemisch, L.; Liebel, M.; Hulst, N. F. van. Isolating Strong Nanoantenna–Molecule Interactions by Ensemble-Level Single-Molecule Detection. *Nanoscale* **2020**, *12* (6), 3723–3730. https://doi.org/10.1039/C9NR08833D.

(74) Zuo, T.; Goldwyn, H. J.; Isaacoff, B. P.; Masiello, D. J.; Biteen, J. S. Rotation of Single-Molecule Emission Polarization by Plasmonic Nanorods. *J. Phys. Chem. Lett.* **2019**, *10* (17), 5047–5054. https://doi.org/10.1021/acs.jpclett.9b02270.

(75) Willets, K. A.; Van Duyne, R. P. Localized Surface Plasmon Resonance Spectroscopy and Sensing. *Annual Review of Physical Chemistry* **2007**, *58* (1), 267–297. https://doi.org/10.1146/annurev.physchem.58.032806.104607.

(76) Willets, K. A.; Wilson, A. J.; Sundaresan, V.; Joshi, P. B. Super-Resolution Imaging and Plasmonics. *Chem. Rev.* **2017**, *117* (11), 7538–7582. https://doi.org/10.1021/acs.chemrev.6b00547.

(77) Chattopadhyay, S.; Biteen, J. S. Super-Resolution Characterization of Heterogeneous Light–Matter Interactions between Single Dye Molecules and Plasmonic Nanoparticles. *Anal. Chem.* **2021**, *93* (1), 430–444. https://doi.org/10.1021/acs.analchem.0c04280.

(78) Tan, S. J.; Zhang, L.; Zhu, D.; Goh, X. M.; Wang, Y. M.; Kumar, K.; Qiu, C.-W.; Yang, J. K. W. Plasmonic Color Palettes for Photorealistic Printing with Aluminum Nanostructures. *Nano Lett.* **2014**, *14* (7), 4023–4029. https://doi.org/10.1021/nl501460x.

(79) Kazuma, E.; Jung, J.; Ueba, H.; Trenary, M.; Kim, Y. Real-Space and Real-Time Observation of a Plasmon-Induced Chemical Reaction of a Single Molecule. *Science* **2018**, *360* (6388), 521–526. https://doi.org/10.1126/science.aao0872.

(80) Wertz, E.; Isaacoff, B. P.; Flynn, J. D.; Biteen, J. S. Single-Molecule Super-Resolution Microscopy Reveals How Light Couples to a Plasmonic Nanoantenna on the Nanometer Scale. *Nano Lett.* **2015**, *15* (4), 2662–2670. https://doi.org/10.1021/acs.nanolett.5b00319.

(81) Kumar, N.; Mignuzzi, S.; Su, W.; Roy, D. Tip-Enhanced Raman Spectroscopy: Principles and Applications. *EPJ Techn Instrum* **2015**, *2* (1), 1–23. https://doi.org/10.1140/epjti/s40485-015-0019-5.

(82) Langer, J.; Jimenez de Aberasturi, D.; Aizpurua, J.; Alvarez-Puebla, R. A.; Auguié, B.; Baumberg, J. J.; Bazan, G. C.; Bell, S. E. J.; Boisen, A.; Brolo, A. G.; Choo, J.; Cialla-May, D.; Deckert, V.; Fabris, L.; Faulds, K.; García de Abajo, F. J.; Goodacre, R.; Graham, D.; Haes, A. J.; Haynes, C. L.; Huck, C.; Itoh, T.; Käll, M.; Kneipp, J.; Kotov, N. A.; Kuang, H.; Le Ru, E. C.; Lee, H. K.; Li, J.-F.; Ling, X. Y.; Maier, S. A.; Mayerhöfer, T.; Moskovits, M.; Murakoshi, K.; Nam, J.-M.; Nie, S.; Ozaki, Y.; Pastoriza-Santos, I.; Perez-Juste, J.; Popp, J.; Pucci, A.; Reich, S.; Ren, B.; Schatz, G. C.; Shegai, T.; Schlücker, S.; Tay, L.-L.; Thomas, K. G.; Tian, Z.-Q.; Van Duyne, R. P.; Vo-Dinh, T.; Wang, Y.; Willets, K. A.; Xu, C.; Xu, H.; Xu, Y.; Yamamoto, Y. S.; Zhao, B.; Liz-Marzán, L. M. Present and Future of Surface-Enhanced Raman Scattering. *ACS Nano* **2020**, *14* (1), 28–117. https://doi.org/10.1021/acsnano.9b04224.

(83) Xu, Y.; Lee, R. K.; Yariv, A. Quantum Analysis and the Classical Analysis of Spontaneous Emission in a Microcavity. *Phys. Rev. A* **2000**, *61* (3), 033807. https://doi.org/10.1103/PhysRevA.61.033807.

(84) Ayala-Orozco, C.; Liu, J. G.; Knight, M. W.; Wang, Y.; Day, J. K.; Nordlander, P.; Halas, N. J. Fluorescence Enhancement of Molecules Inside a Gold Nanomatryoshka. *Nano Lett.* **2014**, *14* (5), 2926–2933. https://doi.org/10.1021/nl501027j.

(85) Fu, B.; Flynn, J. D.; Isaacoff, B. P.; Rowland, D. J.; Biteen, J. S. Super-Resolving the Distance-Dependent Plasmon-Enhanced Fluorescence of Single Dye and Fluorescent Protein Molecules. *J. Phys. Chem. C* **2015**, *119* (33), 19350–19358. https://doi.org/10.1021/acs.jpcc.5b05154.

(86) Blanquer, G.; van Dam, B.; Gulinatti, A.; Acconcia, G.; De Wilde, Y.; Izeddin, I.; Krachmalnicoff, V. Relocating Single Molecules in Super-Resolved Fluorescence Lifetime Images near a Plasmonic Nanostructure. *ACS Photonics* **2020**, *7* (2), 393–400. https://doi.org/10.1021/acsphotonics.9b01317.

(87) Anger, P.; Bharadwaj, P.; Novotny, L. Enhancement and Quenching of Single-Molecule Fluorescence. *Phys. Rev. Lett.* **2006**, *96* (11), 113002. https://doi.org/10.1103/PhysRevLett.96.113002.

(88) Bharadwaj, P.; Deutsch, B.; Novotny, L. Optical Antennas. *Adv. Opt. Photon., AOP* **2009**, *1* (3), 438–483. https://doi.org/10.1364/AOP.1.000438.

(89) Lieberman, I.; Shemer, G.; Fried, T.; Kosower, E. M.; Markovich, G. Plasmon-Resonance-Enhanced Absorption and Circular Dichroism. *Angewandte Chemie International Edition* **2008**, *47* (26), 4855–4857. https://doi.org/10.1002/anie.200800231.

(90) Zhao, R.; Zhang, L.; Zhou, J.; Koschny, Th.; Soukoulis, C. M. Conjugated Gammadion Chiral Metamaterial with Uniaxial Optical Activity and Negative Refractive Index. *Phys. Rev. B* **2011**, *83* (3), 035105. https://doi.org/10.1103/PhysRevB.83.035105.

(91) Li, W.; Coppens, Z. J.; Besteiro, L. V.; Wang, W.; Govorov, A. O.; Valentine, J. Circularly Polarized Light Detection with Hot Electrons in Chiral Plasmonic Metamaterials. *Nat Commun* **2015**, *6* (1), 8379. https://doi.org/10.1038/ncomms9379.

(92) Hentschel, M.; Schäferling, M.; Duan, X.; Giessen, H.; Liu, N. Chiral Plasmonics. *Science Advances* **2017**, *3* (5), e1602735. https://doi.org/10.1126/sciadv.1602735.

(93) Valev, V. K.; Baumberg, J. J.; Sibilia, C.; Verbiest, T. Chirality and Chiroptical Effects in Plasmonic Nanostructures: Fundamentals, Recent Progress, and Outlook. *Advanced Materials* **2013**, *25* (18), 2517–2534. https://doi.org/10.1002/adma.201205178.

(94) Hendry, E.; Mikhaylovskiy, R. V.; Barron, L. D.; Kadodwala, M.; Davis, T. J. Chiral Electromagnetic Fields Generated by Arrays of Nanoslits. *Nano Lett.* **2012**, *12* (7), 3640–3644. https://doi.org/10.1021/nl3012787.

(95) Karst, J.; Cho, N. H.; Kim, H.; Lee, H.-E.; Nam, K. T.; Giessen, H.; Hentschel, M. Chiral Scatterometry on Chemically Synthesized Single Plasmonic Nanoparticles. *ACS Nano* **2019**, *13* (8), 8659–8668. https://doi.org/10.1021/acsnano.9b04046.

(96) García-Etxarri, A.; Dionne, J. A. Surface-Enhanced Circular Dichroism Spectroscopy Mediated by Nonchiral Nanoantennas. *Phys. Rev. B* **2013**, *87* (23), 235409. https://doi.org/10.1103/PhysRevB.87.235409.

(97) Gilroy, C.; Hashiyada, S.; Endo, K.; Karimullah, A. S.; Barron, L. D.; Okamoto, H.; Togawa, Y.; Kadodwala, M. Roles of Superchirality and Interference in Chiral Plasmonic Biodetection. *J. Phys. Chem. C* **2019**, *123* (24), 15195–15203. https://doi.org/10.1021/acs.jpcc.9b02791.

(98) Goerlitzer, E. S. A.; Puri, A. S.; Moses, J. J.; Poulikakos, L. V.; Vogel, N. The Beginner's Guide to Chiral Plasmonics: Mostly Harmless Theory and the Design of Large-Area Substrates. *Advanced Optical Materials* **2021**, *9* (16), 2100378. https://doi.org/10.1002/adom.202100378.

(99) Poulikakos, L. V.; Gutsche, P.; McPeak, K. M.; Burger, S.; Niegemann, J.; Hafner, C.; Norris, D. J. Optical Chirality Flux as a Useful Far-Field Probe of Chiral Near Fields. *ACS Photonics* **2016**, *3* (9), 1619–1625. https://doi.org/10.1021/acsphotonics.6b00201.

(100) Poulikakos, L. V.; Thureja, P.; Stollmann, A.; De Leo, E.; Norris, D. J. Chiral Light Design and Detection Inspired by Optical Antenna Theory. *Nano Lett.* **2018**, *18* (8), 4633–4640. https://doi.org/10.1021/acs.nanolett.8b00083.

(101) Kumar, J.; Eraña, H.; López-Martínez, E.; Claes, N.; Martín, V. F.; Solís, D. M.; Bals, S.; Cortajarena, A. L.; Castilla, J.; Liz-Marzán, L. M. Detection of Amyloid Fibrils in Parkinson's Disease Using Plasmonic Chirality. *Proceedings of the National Academy of Sciences* **2018**, *115* (13), 3225–3230. https://doi.org/10.1073/pnas.1721690115.

(102) Kim, J. Y.; McGlothin, C.; Cha, M.; Pfaffenberger, Z.; Emre, E. T.; Choi, W.; Kim, S.; Biteen, J.; Kotov, N. Direct Printing of Helical Metal Arrays by Circularly Polarized Light. ChemRxiv March 21, 2023. https://doi.org/10.26434/chemrxiv-2023-b342r.

(103) Pfaffenberger, Z.; Chattopadhyay, S.; Biteen, J. Far-Field Polarization Optics Control the Nanometer-Scale Pattern of High Fluorescence Dissymmetry Emission from Achiral Molecules near Plasmonic Nanodimers. *J. Phys. Chem. C* **2023**. https://doi.org/10.1021/acs.jpcc.3c00467.

(104) Dave3457. *GIF Animation of Left-Handed/Counter-Clockwise Circularly Polarized Light*. https://commons.wikimedia.org/wiki/File:Circular.Polarization.Circularly.Polarized.Light_Left.Hand.Animation.305x190.255Colors.gif (accessed 2023-04-16).

(105) Collett, E. *Field Guide to Polarization*; SPIE: 1000 20th Street, Bellingham, WA 98227-0010 USA, 2005. https://doi.org/10.1117/3.626141.

(106) Hilfiker, J. N.; Hong, N.; Schoeche, S. Mueller Matrix Spectroscopic Ellipsometry. *Advanced Optical Technologies* **2022**, *11* (3–4), 59–91. https://doi.org/10.1515/aot-2022-0008.

(107) Schaefer, B.; Collett, E.; Smyth, R. Measuring the Stokes Polarization Parameters. *Am. J. Phys.* **2007**, *75* (2), 7.

(108) Nesterov, A. V.; Niziev, V. G. Laser Beams with Axially Symmetric Polarization. *J. Phys. D: Appl. Phys.* **2000**, *33* (15), 1817. https://doi.org/10.1088/0022-3727/33/15/310.

(109) Epstein, H. M.; Dulaney, J. L. Unpolarized Laser Oscillators. 5075893, December 24, 1991. https://www.freepatentsonline.com/5075893.html (accessed 2023-04-17).

(110) *Half-Wave Liquid Crystal Variable Retarders / Wave Plates*. https://www.thorlabs.com/newgrouppage9.cfm?objectgroup_id=6179 (accessed 2023-03-16).

(111) *Creative Commons — Attribution-NonCommercial 3.0 Unported — CC BY-NC 3.0*. https://creativecommons.org/licenses/by-nc/3.0/ (accessed 2023-05-06).

(112) Reichman, J. Handbook of Optical Filters for Fluorescence Microscopy. *Chroma Technology Corporation* **2000**.

(113) Tang, Y.; Cook, T. A.; Cohen, A. E. Limits on Fluorescence Detected Circular Dichroism of Single Helicene Molecules. *J. Phys. Chem. A* **2009**, *113* (22), 6213–6216. https://doi.org/10.1021/jp903598t.

(114) *An Introduction to Optical Activity*. http://www.chem.cmu.edu/groups/bominaar/index.html (accessed 2023-03-15).

(115) López-Téllez, J. M.; Bruce, N. C.; Rodríguez-Herrera, O. G. Characterization of Optical Polarization Properties for Liquid Crystal-Based Retarders. *Appl. Opt., AO* **2016**, *55* (22), 6025–6033. https://doi.org/10.1364/AO.55.006025.

(116) Raziman, T. V.; Godiksen, R. H.; Müller, M. A.; Curto, A. G. Conditions for Enhancing Chiral Nanophotonics near Achiral Nanoparticles. *ACS Photonics* **2019**, *6* (10), 2583–2589. https://doi.org/10.1021/acsphotonics.9b01200.

(117) Campos-Jara, A.; García Parejo, P.; Álvarez-Herrero, A. Optimization of the Response Time Measuring Method for Liquid Crystal Variable Retarders. *Journal of Vacuum Science & Technology B* **2019**, *37* (6), 062930. https://doi.org/10.1116/1.5122786.

(118) Utsumi, Y.; Kamei, T.; Naito, R.; Saito, K. Measurement Methods of Nematic Liquid Crystal Response Time. *Molecular Crystals and Liquid Crystals* **2005**, *434* (1), 9/[337]-24/[352]. https://doi.org/10.1080/15421400590954452.

(119) Camacho, R.; Täuber, D.; Scheblykin, I. G. Fluorescence Anisotropy Reloaded—Emerging Polarization Microscopy Methods for Assessing Chromophores' Organization and Excitation Energy Transfer in Single Molecules, Particles, Films, and Beyond. *Advanced Materials* **2019**, *31* (22), 1805671. https://doi.org/10.1002/adma.201805671.

(120) Montes-González, I.; Bruce, N. C.; Rodríguez-Herrera, O. G.; Núñez, O. R. Method to Calibrate a Full-Stokes Polarimeter Based on Variable Retarders. *Appl. Opt., AO* **2019**, *58* (22), 5952–5957. https://doi.org/10.1364/AO.58.005952.

(121) Cyphersmith, A.; Surampudi, S.; Casey, M. J.; Jankowski, K.; Venkataraman, D.; Barnes, M. D. Chiroptical Dissymmetries in Fluorescence Excitation from Single Molecules of (M-2) Helicene Dimers. *J. Phys. Chem. A* **2012**, *116* (22), 5349–5352. https://doi.org/10.1021/jp300352n.

(122) MacKenzie, L. E.; Pålsson, L.-O.; Parker, D.; Beeby, A.; Pal, R. Rapid Time-Resolved Circular Polarization Luminescence (CPL) Emission Spectroscopy. *Nat Commun* **2020**, *11* (1), 1676. https://doi.org/10.1038/s41467-020-15469-5.

(123) Macias-Romero, C.; Török, P. Eigenvalue Calibration Methods for Polarimetry. *Journal of the European Optical Society - Rapid publications* **2012**, *7* (0). https://doi.org/10.2971/jeos.2012.12004.

(124) Schindelin, J.; Arganda-Carreras, I.; Frise, E.; Kaynig, V.; Longair, M.; Pietzsch, T.; Preibisch, S.; Rueden, C.; Saalfeld, S.; Schmid, B.; Tinevez, J.-Y.; White, D. J.; Hartenstein, V.; Eliceiri, K.; Tomancak, P.; Cardona, A. Fiji: An Open-Source Platform for Biological-Image Analysis. *Nat Methods* **2012**, *9* (7), 676–682. https://doi.org/10.1038/nmeth.2019.

(125) Amabilino, D. B.; Amabilino, D. B. *Chirality at the Nanoscale Nanoparticles, Surfaces, Materials and More*; Wiley-VCH: Weinheim, 2009.

(126) Tokunaga, E.; Yamamoto, T.; Ito, E.; Shibata, N. Understanding the Thalidomide Chirality in Biological Processes by the Self-Disproportionation of Enantiomers. *Sci Rep* **2018**, *8* (1), 17131. https://doi.org/10.1038/s41598-018-35457-6.

(127) Fazel-Najafabadi, A.; Schuster, S.; Auguié, B. Orientation Averaging of Optical Chirality near Nanoparticles and Aggregates. *Phys. Rev. B* **2021**, *103* (11), 115405. https://doi.org/10.1103/PhysRevB.103.115405.

(128) Wakabayashi, M.; Yokojima, S.; Fukaminato, T.; Shiino, K.; Irie, M.; Nakamura, S. Anisotropic Dissymmetry Factor, g: Theoretical Investigation on Single Molecule Chiroptical Spectroscopy. *J. Phys. Chem. A* **2014**, *118* (27), 5046–5057. https://doi.org/10.1021/jp409559t.

(129) Tanaka, H.; Inoue, Y.; Mori, T. Circularly Polarized Luminescence and Circular Dichroisms in Small Organic Molecules: Correlation between Excitation and Emission Dissymmetry Factors. *ChemPhotoChem* **2018**, *2* (5), 386–402. https://doi.org/10.1002/cptc.201800015.

(130) García-Guirado, J.; Svedendahl, M.; Puigdollers, J.; Quidant, R. Enantiomer-Selective Molecular Sensing Using Racemic Nanoplasmonic Arrays. *Nano Lett.* **2018**, *18* (10), 6279–6285. https://doi.org/10.1021/acs.nanolett.8b02433.

(131) Yan, C.; Wang, X.; Raziman, T. V.; Martin, O. J. F. Twisting Fluorescence through Extrinsic Chiral Antennas. *Nano Lett.* **2017**, *17* (4), 2265–2272. https://doi.org/10.1021/acs.nanolett.6b04906.

(132) Pachidis, P.; Cote, B. M.; Ferry, V. E. Tuning the Polarization and Directionality of Photoluminescence of Achiral Quantum Dot Films with Chiral Nanorod Dimer Arrays: Implications for Luminescent Applications. *ACS Appl. Nano Mater.* **2019**, *2* (9), 5681–5687. https://doi.org/10.1021/acsanm.9b01198.

(133) Adhikari, S.; Orrit, M. Optically Probing the Chirality of Single Plasmonic Nanostructures and of Single Molecules: Potential and Obstacles. *ACS Photonics* **2022**, *9* (11), 3486–3497. https://doi.org/10.1021/acsphotonics.2c01205.

(134) Isaacoff, B. P.; Li, Y.; Lee, S. A.; Biteen, J. S. SMALL-LABS: Measuring Single-Molecule Intensity and Position in Obscuring Backgrounds. *Biophysical Journal* **2019**, *116* (6), 975–982. https://doi.org/10.1016/j.bpj.2019.02.006.

(135) Raab, M.; Vietz, C.; Stefani, F. D.; Acuna, G. P.; Tinnefeld, P. Shifting Molecular Localization by Plasmonic Coupling in a Single-Molecule Mirage. *Nat Commun* **2017**, *8* (1), 13966. https://doi.org/10.1038/ncomms13966.

(136) Mack, D. L.; Cortés, E.; Giannini, V.; Török, P.; Roschuk, T.; Maier, S. A. Decoupling Absorption and Emission Processes in Super-Resolution Localization of Emitters in a Plasmonic Hotspot. *Nat Commun* **2017**, *8* (1), 14513. https://doi.org/10.1038/ncomms14513.

(137) Goldwyn, H. J.; Smith, K. C.; Busche, J. A.; Masiello, D. J. Mislocalization in Plasmon-Enhanced Single-Molecule Fluorescence Microscopy as a Dynamical Young's Interferometer. *ACS Photonics* **2018**, *5* (8), 3141–3151. https://doi.org/10.1021/acsphotonics.8b00372.

(138) Cotrufo, M.; Osorio, C. I.; Koenderink, A. F. Spin-Dependent Emission from Arrays of Planar Chiral Nanoantennas Due to Lattice and Localized Plasmon Resonances. *ACS Nano* **2016**, *10* (3), 3389–3397. https://doi.org/10.1021/acsnano.5b07231.

(139) Le, K. Q.; Hashiyada, S.; Kondo, M.; Okamoto, H. Circularly Polarized Photoluminescence from Achiral Dye Molecules Induced by Plasmonic Two-Dimensional Chiral Nanostructures. *J. Phys. Chem. C* **2018**, *122* (43), 24924–24932. https://doi.org/10.1021/acs.jpcc.8b07297.

(140) Meinzer, N.; Hendry, E.; Barnes, W. L. Probing the Chiral Nature of Electromagnetic Fields Surrounding Plasmonic Nanostructures. *Phys. Rev. B* **2013**, *88* (4), 041407. https://doi.org/10.1103/PhysRevB.88.041407.

(141) Hassey, R.; Swain, E. J.; Hammer, N. I.; Venkataraman, D.; Barnes, M. D. Probing the Chiroptical Response of a Single Molecule. *Science* **2006**, *314* (5804), 1437–1439. https://doi.org/10.1126/science.1134231.

(142) Wertz, E. A.; Isaacoff, B. P.; Biteen, J. S. Wavelength-Dependent Super-Resolution Images of Dye Molecules Coupled to Plasmonic Nanotriangles. *ACS Photonics* **2016**, *3* (10), 1733–1740. https://doi.org/10.1021/acsphotonics.6b00344.

(143) Johnson, P. B.; Christy, R. W. Optical Constants of the Noble Metals. *Phys. Rev. B* **1972**, *6* (12), 4370–4379. https://doi.org/10.1103/PhysRevB.6.4370.

(144) Palik, E. D.; Ghosh, G. C. *Handbook of Optical Constants of Solids Five-Volume Set: Handbook of Thermo-Optic Coefficients of Optical Materials with Applications*; Elsevier Science: Burlington, 1997.

(145) Tian, X.; Fang, Y.; Sun, M. Formation of Enhanced Uniform Chiral Fields in Symmetric Dimer Nanostructures. *Sci Rep* **2015**, *5* (1), 17534. https://doi.org/10.1038/srep17534.

(146) Hendry, E.; Mikhaylovskiy, R. V.; Barron, L. D.; Kadodwala, M.; Davis, T. J. Chiral Electromagnetic Fields Generated by Arrays of Nanoslits. *Nano Lett.* **2012**, *12* (7), 3640–3644. https://doi.org/10.1021/nl3012787.

(147) Fu, B.; Isaacoff, B. P.; Biteen, J. S. Super-Resolving the Actual Position of Single Fluorescent Molecules Coupled to a Plasmonic Nanoantenna. *ACS Nano* **2017**, *11* (9), 8978–8987. https://doi.org/10.1021/acsnano.7b03420.

(148) Su, L.; Yuan, H.; Lu, G.; Rocha, S.; Orrit, M.; Hofkens, J.; Uji-i, H. Super-Resolution Localization and Defocused Fluorescence Microscopy on Resonantly Coupled Single-Molecule, Single-Nanorod Hybrids. *ACS Nano* **2016**, *10* (2), 2455–2466. https://doi.org/10.1021/acsnano.5b07294.

(149) Kumar, J.; Nakashima, T.; Kawai, T. Circularly Polarized Luminescence in Chiral Molecules and Supramolecular Assemblies. *J. Phys. Chem. Lett.* **2015**, *6* (17), 3445–3452. https://doi.org/10.1021/acs.jpclett.5b01452.

(150) Zhao, Y.; Saleh, A. A. E.; Dionne, J. A. Enantioselective Optical Trapping of Chiral Nanoparticles with Plasmonic Tweezers. *ACS Photonics* **2016**, *3* (3), 304–309. https://doi.org/10.1021/acsphotonics.5b00574.

(151) Alizadeh, M. H.; Reinhard, B. M. Plasmonically Enhanced Chiral Optical Fields and Forces in Achiral Split Ring Resonators. *ACS Photonics* **2015**, *2* (3), 361–368. https://doi.org/10.1021/ph500399k.

(152) Iadanza, M. G.; Jackson, M. P.; Hewitt, E. W.; Ranson, N. A.; Radford, S. E. A New Era for Understanding Amyloid Structures and Disease. *Nat Rev Mol Cell Biol* **2018**, *19* (12), 755–773. https://doi.org/10.1038/s41580-018-0060-8.

(153) Sipe, J. D.; Cohen, A. S. Review: History of the Amyloid Fibril. *Journal of Structural Biology* **2000**, *130* (2), 88–98. https://doi.org/10.1006/jsbi.2000.4221.

(154) Balistreri, A.; Goetzler, E.; Chapman, M. Functional Amyloids Are the Rule Rather Than the Exception in Cellular Biology. *Microorganisms* **2020**, *8* (12), 1951. https://doi.org/10.3390/microorganisms8121951.

(155) Channon, K. J.; Devlin, G. L.; MacPhee, C. E. Efficient Energy Transfer within Self-Assembling Peptide Fibers: A Route to Light-Harvesting Nanomaterials. *J. Am. Chem. Soc.* **2009**, *131* (35), 12520–12521. https://doi.org/10.1021/ja902825j.

(156) Maji, S. K.; Schubert, D.; Rivier, C.; Lee, S.; Rivier, J. E.; Riek, R. Amyloid as a Depot for the Formulation of Long-Acting Drugs. *PLOS Biology* **2008**, *6* (2), e17. https://doi.org/10.1371/journal.pbio.0060017.

(157) Volpatti, L. R.; Vendruscolo, M.; Dobson, C. M.; Knowles, T. P. J. A Clear View of Polymorphism, Twist, and Chirality in Amyloid Fibril Formation. *ACS Nano* **2013**, *7* (12), 10443–10448. https://doi.org/10.1021/nn406121w.

(158) Dzwolak, W.; Surmacz-Chwedoruk, W.; Babenko, V. Conformational Memory Effect Reverses Chirality of Vortex-Induced Insulin Amyloid Superstructures. *Langmuir* **2013**, *29* (1), 365–370. https://doi.org/10.1021/la304374q.

(159) *Methods for Structural Analysis of Amyloid Fibrils in Misfolding Diseases | SpringerLink*. https://link.springer.com/protocol/10.1007/978-1-4939-8820-4_7 (accessed 2023-05-04).

(160) Lu, J.; Xue, Y.; Bernardino, K.; Zhang, N.-N.; Gomes, W. R.; Ramesar, N. S.; Liu, S.; Hu, Z.; Sun, T.; de Moura, A. F.; Kotov, N. A.; Liu, K. Enhanced Optical Asymmetry in Supramolecular Chiroplasmonic Assemblies with Long-Range Order. *Science* **2021**, *371* (6536), 1368–1374. https://doi.org/10.1126/science.abd8576.

(161) Vila-Liarte, D.; A. Kotov, N.; M. Liz-Marzán, L. Template-Assisted Self-Assembly of Achiral Plasmonic Nanoparticles into Chiral Structures. *Chemical Science* **2022**, *13* (3), 595–610. https://doi.org/10.1039/D1SC03327A.

(162) Govorov, A. O.; Fan, Z.; Hernandez, P.; Slocik, J. M.; Naik, R. R. Theory of Circular Dichroism of Nanomaterials Comprising Chiral Molecules and Nanocrystals: Plasmon Enhancement, Dipole Interactions, and Dielectric Effects. *Nano Lett.* **2010**, *10* (4), 1374–1382. https://doi.org/10.1021/nl100010v.

(163) Rybicka, A.; Longhi, G.; Castiglioni, E.; Abbate, S.; Dzwolak, W.; Babenko, V.; Pecul, M. Thioflavin T: Electronic Circular Dichroism and Circularly Polarized Luminescence Induced by Amyloid Fibrils. *ChemPhysChem* **2016**, *17* (18), 2931–2937. https://doi.org/10.1002/cphc.201600235.

(164) Govorov, A. O. Plasmon-Induced Circular Dichroism of a Chiral Molecule in the Vicinity of Metal Nanocrystals. Application to Various Geometries. *J. Phys. Chem. C* **2011**, *115* (16), 7914–7923. https://doi.org/10.1021/jp1121432.

(165) Obstarczyk, P.; Lipok, M.; Grelich-Mucha, M.; Samoć, M.; Olesiak-Bańska, J. Two-Photon Excited Polarization-Dependent Autofluorescence of Amyloids as a Label-Free Method of Fibril Organization Imaging. *J. Phys. Chem. Lett.* **2021**, *12* (5), 1432–1437. https://doi.org/10.1021/acs.jpclett.0c03511.

(166) Pfaffenberger, Z.; Chattopadhyay, S.; Biteen, J. Near-Field Optical Chirality Is Correlated with the Pattern of High Fluorescence Dissymmetry Emission from Achiral Molecules near Gold Nanodimers, 2023.

(167) Aurand, B.; Rödel, C.; Zhao, H.; Kuschel, S.; Wünsche, M.; Jäckel, O.; Heyer, M.; Wunderlich, F.; Kaluza, M. C.; Paulus, G. G.; Kuehl, T. Note: A Large Aperture Four-Mirror

Reflective Wave-Plate for High-Intensity Short-Pulse Laser Experiments. *Review of Scientific Instruments* **2012**, *83* (3), 036104. https://doi.org/10.1063/1.3694659.

(168) Guerrero-Martínez, A.; Auguié, B.; Alonso-Gómez, J. L.; Džolić, Z.; Gómez-Graña, S.; Žinić, M.; Cid, M. M.; Liz-Marzán, L. M. Intense Optical Activity from Three-Dimensional Chiral Ordering of Plasmonic Nanoantennas. *Angewandte Chemie International Edition* **2011**, *50* (24), 5499–5503. https://doi.org/10.1002/anie.201007536.

(169) Jain, P. K.; Eustis, S.; El-Sayed, M. A. Plasmon Coupling in Nanorod Assemblies: Optical Absorption, Discrete Dipole Approximation Simulation, and Exciton-Coupling Model. *J. Phys. Chem. B* **2006**, *110* (37), 18243–18253. https://doi.org/10.1021/jp063879z.

(170) Kollmer, M.; Close, W.; Funk, L.; Rasmussen, J.; Bsoul, A.; Schierhorn, A.; Schmidt, M.; Sigurdson, C. J.; Jucker, M.; Fändrich, M. Cryo-EM Structure and Polymorphism of Aβ Amyloid Fibrils Purified from Alzheimer's Brain Tissue. *Nat Commun* **2019**, *10* (1), 4760. https://doi.org/10.1038/s41467-019-12683-8.

(171) Kumar, J.; Eraña, H.; López-Martínez, E.; Claes, N.; Martín, V. F.; Solís, D. M.; Bals, S.; Cortajarena, A. L.; Castilla, J.; Liz-Marzán, L. M. Detection of Amyloid Fibrils in Parkinson's Disease Using Plasmonic Chirality. *Proceedings of the National Academy of Sciences* **2018**, *115* (13), 3225–3230. https://doi.org/10.1073/pnas.1721690115.

(172) Guerrero-Martínez, A.; Auguié, B.; Alonso-Gómez, J. L.; Džolić, Z.; Gómez-Graña, S.; Žinić, M.; Cid, M. M.; Liz-Marzán, L. M. Intense Optical Activity from Three-Dimensional Chiral Ordering of Plasmonic Nanoantennas. *Angewandte Chemie International Edition* **2011**, *50* (24), 5499–5503. https://doi.org/10.1002/anie.201007536.

(173) Tanaka, H.; Kato, Y.; Fujiki, M.; Inoue, Y.; Mori, T. Combined Experimental and Theoretical Study on Circular Dichroism and Circularly Polarized Luminescence of Configurationally Robust D3-Symmetric Triple Pentahelicene. *J. Phys. Chem. A* **2018**, *122* (37), 7378–7384. https://doi.org/10.1021/acs.jpca.8b05247.

(174) Chemistry (IUPAC), T. I. U. of P. and A. *IUPAC - absorbance (A00028)*. https://doi.org/10.1351/goldbook.A00028.

(175) Govorov, A. O.; Fan, Z.; Hernandez, P.; Slocik, J. M.; Naik, R. R. Theory of Circular Dichroism of Nanomaterials Comprising Chiral Molecules and Nanocrystals: Plasmon Enhancement, Dipole Interactions, and Dielectric Effects. *Nano Lett.* **2010**, *10* (4), 1374–1382. https://doi.org/10.1021/nl100010v.

(176) Shaban, H. A.; Valades-Cruz, C. A.; Savatier, J.; Brasselet, S. Polarized Super-Resolution Structural Imaging inside Amyloid Fibrils Using Thioflavine T. *Sci Rep* **2017**, *7* (1), 12482. https://doi.org/10.1038/s41598-017-12864-9.

(177) Duboisset, J.; Ferrand, P.; He, W.; Wang, X.; Rigneault, H.; Brasselet, S. Thioflavine-T and Congo Red Reveal the Polymorphism of Insulin Amyloid Fibrils When Probed by

Polarization-Resolved Fluorescence Microscopy. *J. Phys. Chem. B* **2013**, *117* (3), 784–788. https://doi.org/10.1021/jp309528f.

(178) Hestand, N. J.; Spano, F. C. Expanded Theory of H- and J-Molecular Aggregates: The Effects of Vibronic Coupling and Intermolecular Charge Transfer. *Chem. Rev.* **2018**, *118* (15), 7069–7163. https://doi.org/10.1021/acs.chemrev.7b00581.

(179) Kringle, L.; Sawaya, N. P. D.; Widom, J.; Adams, C.; Raymer, M. G.; Aspuru-Guzik, A.; Marcus, A. H. Temperature-Dependent Conformations of Exciton-Coupled Cy3 Dimers in Double-Stranded DNA. *The Journal of Chemical Physics* **2018**, *148* (8), 085101. https://doi.org/10.1063/1.5020084.

(180) Lan, X.; Zhou, X.; McCarthy, L. A.; Govorov, A. O.; Liu, Y.; Link, S. DNA-Enabled Chiral Gold Nanoparticle–Chromophore Hybrid Structure with Resonant Plasmon–Exciton Coupling Gives Unusual and Strong Circular Dichroism. *J. Am. Chem. Soc.* **2019**, *141* (49), 19336–19341. https://doi.org/10.1021/jacs.9b08797.

(181) Balistreri, A.; Goetzler, E.; Chapman, M. Functional Amyloids Are the Rule Rather Than the Exception in Cellular Biology. *Microorganisms* **2020**, *8* (12), 1951. https://doi.org/10.3390/microorganisms8121951.

(182) Otzen, D.; Riek, R. Functional Amyloids. *Cold Spring Harb Perspect Biol* **2019**, *11* (12), a033860. https://doi.org/10.1101/cshperspect.a033860.

(183) Chapman, M. R.; Robinson, L. S.; Pinkner, J. S.; Roth, R.; Heuser, J.; Hammar, M.; Normark, S.; Hultgren, S. J. Role of Escherichia Coli Curli Operons in Directing Amyloid Fiber Formation. *Science* **2002**, *295* (5556), 851–855. https://doi.org/10.1126/science.1067484.

(184) Dueholm, M. S.; Nielsen, S. B.; Hein, K. L.; Nissen, P.; Chapman, M.; Christiansen, G.; Nielsen, P. H.; Otzen, D. E. Fibrillation of the Major Curli Subunit CsgA under a Wide Range of Conditions Implies a Robust Design of Aggregation. *Biochemistry* **2011**, *50* (39), 8281–8290. https://doi.org/10.1021/bi200967c.

(185) Jiménez, J. L.; Nettleton, E. J.; Bouchard, M.; Robinson, C. V.; Dobson, C. M.; Saibil, H. R. The Protofilament Structure of Insulin Amyloid Fibrils. *Proceedings of the National Academy of Sciences* **2002**, *99* (14), 9196–9201. https://doi.org/10.1073/pnas.142459399.

(186) Rybicka, A.; Longhi, G.; Castiglioni, E.; Abbate, S.; Dzwolak, W.; Babenko, V.; Pecul, M. Thioflavin T: Electronic Circular Dichroism and Circularly Polarized Luminescence Induced by Amyloid Fibrils. *ChemPhysChem* **2016**, *17* (18), 2931–2937. https://doi.org/10.1002/cphc.201600235.

(187) DeBenedictis, E. P.; Ma, D.; Keten, S. Structural Predictions for Curli Amyloid Fibril Subunits CsgA and CsgB. *RSC Adv.* **2017**, *7* (76), 48102–48112. https://doi.org/10.1039/C7RA08030A.

(188) Balistreri, A.; Goetzler, E.; Chapman, M. Functional Amyloids Are the Rule Rather Than the Exception in Cellular Biology. *Microorganisms* **2020**, *8* (12), 1951. https://doi.org/10.3390/microorganisms8121951.

(189) Howie, A. J.; Brewer, D. B.; Howell, D.; Jones, A. P. Physical Basis of Colors Seen in Congo Red-Stained Amyloid in Polarized Light. *Lab Invest* **2008**, *88* (3), 232–242. https://doi.org/10.1038/labinvest.3700714.

(190) Reichhardt, C.; Cegelski, L. The Congo Red Derivative FSB Binds to Curli Amyloid Fibers and Specifically Stains Curliated E. Coli. *PLOS ONE* **2018**, *13* (8), e0203226. https://doi.org/10.1371/journal.pone.0203226.

(191) Reichhardt, C.; Jacobson, A. N.; Maher, M. C.; Uang, J.; McCrate, O. A.; Eckart, M.; Cegelski, L. Congo Red Interactions with Curli-Producing E. Coli and Native Curli Amyloid Fibers. *PLOS ONE* **2015**, *10* (10), e0140388. https://doi.org/10.1371/journal.pone.0140388.

(192) Yakupova, E. I.; Bobyleva, L. G.; Vikhlyantsev, I. M.; Bobylev, A. G. Congo Red and Amyloids: History and Relationship. *Biosci Rep* **2019**, *39* (1), BSR20181415. https://doi.org/10.1042/BSR20181415.

(193) Zhou, Y.; Blanco, L. P.; Smith, D. R.; Chapman, M. R. Bacterial Amyloids. In *Amyloid Proteins: Methods and Protocols*; Sigurdsson, E. M., Calero, M., Gasset, M., Eds.; Methods in Molecular Biology; Humana Press: Totowa, NJ, 2012; pp 303–320. https://doi.org/10.1007/978-1-61779-551-0_21.

(194) Knight, M. W.; King, N. S.; Liu, L.; Everitt, H. O.; Nordlander, P.; Halas, N. J. Aluminum for Plasmonics. *ACS Nano* **2014**, *8* (1), 834–840. https://doi.org/10.1021/nn405495q.

(195) Grillet, N.; Manchon, D.; Cottancin, E.; Bertorelle, F.; Bonnet, C.; Broyer, M.; Lermé, J.; Pellarin, M. Photo-Oxidation of Individual Silver Nanoparticles: A Real-Time Tracking of Optical and Morphological Changes. *J. Phys. Chem. C* **2013**, *117* (5), 2274–2282. https://doi.org/10.1021/jp311502h.

(196) Glover, R. D.; Miller, J. M.; Hutchison, J. E. Generation of Metal Nanoparticles from Silver and Copper Objects: Nanoparticle Dynamics on Surfaces and Potential Sources of Nanoparticles in the Environment. *ACS Nano* **2011**, *5* (11), 8950–8957. https://doi.org/10.1021/nn2031319.